DEVELOPING EXPERIMENTAL METHODS AND ASSESSING METRICS TO EVALUATE CEREBRAL ANEURYSM HEMODYNAMICS

by

Melissa C. Brindise

A Dissertation

Submitted to the Faculty of Purdue University

In Partial Fulfillment of the Requirements for the degree of

Doctor of Philosophy
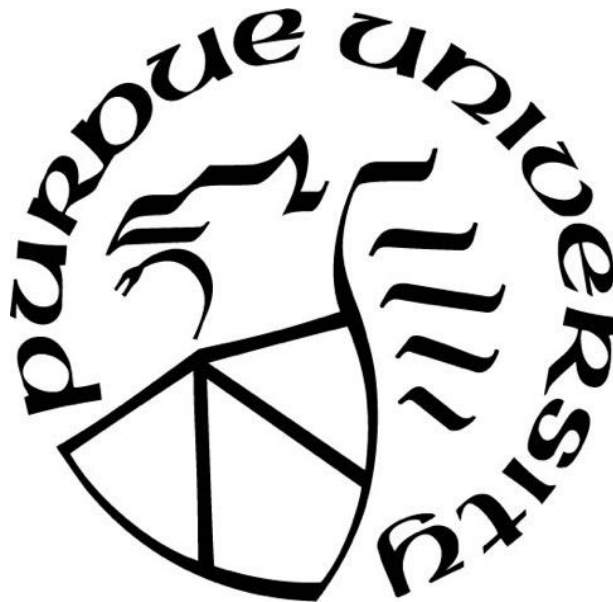
School of Mechanical Engineering

West Lafayette, Indiana

December 2019

THE PURDUE UNIVERSITY GRADUATE SCHOOL
STATEMENT OF COMMITTEE APPROVAL

Dr. Pavlos P. Vlachos, Chair

    School of Mechanical Engineering, Purdue University, West Lafayette, IN

Dr. Vitaliy L. Rayz

    Weldon School of Biomedical Engineering, Purdue University, West Lafayette, IN

Dr. Michael Markl

    McCormick School of Engineering, Northwestern University, Evanston, IL

    Feinberg School of Medicine, Northwestern University, Chicago, IL

Dr. Arezoo Ardekani

    School of Mechanical Engineering, Purdue University, West Lafayette, IN

Approved by:

    Dr. Jay Gore

        Head of the Graduate Program

Dla babci, której siła i odwaga inspirują mnie codziennie

ACKNOWLEDGMENTS

TABLE OF CONTENTS

LIST OF TABLES

LIST OF FIGURES

ABSTRACT

Accurately assessing the risk and growth of rupture among intracranial aneurysms (IA) remains a challenging task for clinicians. Hemodynamic factors are known to play a critical role in the development of IAs, but the specific mechanisms are not well understood. Many studies have sought to correlate specific flow metrics to risk of growth and rupture but have reported conflicting findings. Computational fluid dynamics (CFD) has predominantly been the methodology used to study IA hemodynamics. Yet, CFD assumptions and limitations coupled with the lack of CFD validation has precluded clinical acceptance of IA hemodynamic assessments and likely contributed to the contradictory results among previous studies. Experimental particle image velocimetry (PIV) studies have been noticeably limited in both scope and number among IA studies, in part due to the complexity associated with such experiments. Moreover, the limited understanding of the robustness of hemodynamic metrics across varying flow and measurement environments and the effect of transitional flow in IAs also remain open issues. In this work, techniques to enhance IA PIV capabilities were developed and the first volumetric pulsatile IA PIV study was performed. A novel blood analog solution—a mixture of water, glycerol and urea— was developed and an autonomous methodology for reducing experimental noise in velocity fields was introduced and demonstrated. Both of these experimental techniques can also be used in PIV studies extending beyond IA applications. Further, the onset and development of transitional flow in physiological, pulsatile waveforms was explored. The robustness of hemodynamic metrics such as wall shear stress, oscillatory shear index, and relative residence time across varying modalities, spatiotemporal resolutions, and flow assumptions was explored. Additional hemodynamic metrics which have been demonstrated to be influential in other cardiovascular flows but yet to be tested in IA studies were also identified and considered. Ultimately this work provides a framework for future IA PIV studies as well as insight on using hemodynamic evaluations to assess the risk of growth and rupture of an IA, thereby taking steps towards enhancing the clinical utility of such analysis.

CHAPTER 1. INTRODUCTION

1.1 Motivation

Intracranial aneurysms (IA) are defined as an abnormal bulging in the wall of a brain blood vessel as a result of wall weakening. The rupture of IAs accounts for 10% of all strokes and carries a 50% mortality rate and a 50% morbidity rate [1,2]. While it is estimated that 1 out of every 12 people harbor an unruptured IA, because they are asymptomatic, they typically go undetected [3]. If an IA is detected, a challenging clinical decision must be made as to whether the aneurysm can be monitored over time or must be treated. Treatment carries a combined mortality and morbidity risk of 5% [4]. Likewise, monitoring carries the risk of rupture; though, this risk is difficult to accurately assess as the specific mechanisms that cause an aneurysm to grow and rupture remain largely unknown. Both morphological and hemodynamic factors have been shown to play a critical role in the growth and rupture of an IA [5,6]. However, contradictory findings regarding specific relationships have been reported. For example, some studies have reported the aspect ratio (AR) of an aneurysm is linked to increased risk of rupture while other studies found no correlation [4,7–10]. Similarly, both high and low wall shear stress (WSS) have been associated with increased risk of rupture [3,11–14].

IA hemodynamics can be analyzed using several modalities. *In vivo* flow fields can be obtained clinically using 4D flow magnetic resonance imaging (MRI) but the spatiotemporal resolution and noise associated with this modality prevents accurate, reliable hemodynamic metric evaluation [15–17]. The complex, tortuous, and highly three-dimensional nature of the cerebral vasculature poses significant challenges for *in vitro* experimental modalities. As such, particle image velocimetry (PIV) studies in this domain are limited in both scope and number [15,17–20]. Computational fluid dynamics (CFD) has predominantly been the modality used [1,6,9,11,13,16]. However, due to the lack of experimental data, limited CFD validation has been done and studies have demonstrated differing CFD solver parameters and assumptions can yield large variations in resulting flow metrics, even using similar geometries and boundary conditions [15,21]. Furthermore, the lack of understanding of how modality-specific assumptions, limitations, and flow parameters affect resultant hemodynamic metrics is a major gap among current literature which has prevented clinical acceptance of IA hemodynamic assessments [22]. **The goal of this**

work is to bridge this gap through experimental and multi-modality studies in order to evaluate specific flow parameters which can affect IA hemodynamics, identify metrics more robust to such effects, and develop methodologies to mitigate these ancillary factors in an effort to enhance the clinical utility of IA hemodynamic analysis.

1.2   Background

1.2.1   Factors Affecting Cerebral Aneurysm Risk of Growth and Rupture

1.2.1.1   Morphological Factors

Many studies have sought to link morphological and hemodynamic metrics, to risk of growth and rupture of a cerebral aneurysm. Morphological studies most often use a large cohort (100+) of IA geometries from databases with known outcomes and aneurysm geometric information. Such studies seek to statistically correlate IA rupture to a wide variety of morphological metrics comprising the size, shape, and location of the aneurysm as well as patient health information including age, gender, and family history. However, contradictory findings have been reported. Parameters such as high aspect ratio (AR) and irregular aneurysmal shape have been linked to risk of rupture in some studies, while other studies found no link [4,7–10,23,24]. Similarly, a novel IA rupture risk score, PHASES, was reported but follow-up studies demonstrated IA geometries that ruptured despite being deemed low risk by PHASES [4,8]. Moreover, the databases do not contain flow field information, so no hemodynamic metric correlation is possible.

1.2.1.2   Hemodynamic factors

Hemodynamic studies most often use CFD to model the flow in patient-specific IA geometries. Due to computational costs, studies typically only analyze a few patient-specific geometries (<5), preventing reliable statistical correlation of hemodynamic metrics. Among hemodynamic variables, wall shear stress (WSS) has received substantial attention, due in large part to its controversial reported behavior [3]. Some studies have demonstrated that aneurysms grow at regions of low WSS magnitude, high spatial WSS gradients, and where the WSS in the aneurysmal sac is lower than that of the parent vessel(s) [6,11,12,20]. Yet, other studies have indicated risk of rupture increases with high maximal WSS [13,25]. High oscillatory shear index

(OSI) and high relative residence time (RRT) have also been found to increase risk of rupture, though substantially less studies—especially experimental ones—have analyzed these metrics in detail [3,6,12,20]. Other flow factors such as concentrated inflow jets, small flow impingement regions, lower viscous dissipation, high energy loss within the aneurysmal sac, and larger shear concentration have been identified as possible factors contributing to increased risk of IA rupture [13,19,25–27]. Some hemodynamic metrics such as pressure and pressure wave velocity (PWV) have received little to no attention within the IA domain despite the fact that both are important parameters in other cardiovascular regions. Specifically, high or mismatched PWV has been associated with cardiovascular disease, increased risk for occurrence of aneurysms, as well as restenosis in stented arteries [28–30].

1.2.1.3 Presence of Transitional Flow

Previous work has linked unstable, chaotic flow with increased risk of aneurysm rupture [13,19], precipitating questions as to the extent of transitional flow present in IA's. Transitional flow is characterized by intermittency and can significantly affect hemodynamic metrics such as WSS, OSI, and pressure [31,32]. These effects could play a critical role in the progression and rupture risk of a cerebral aneurysm. Transitional flow has been observed in various areas of the body including the heart, aorta, and stenotic vessels [33–35]. Transitional flow and high-frequency fluctuations have also been demonstrated in aneurysms [9,36], yet many IA risk of rupture studies do not consider the influence of such factors. However, transitional-flow induced flow variations can contribute to conflicting results as one study demonstrated that when high-frequency fluctuations are present a larger disparity between *in vivo* 4D Flow MRI and CFD velocity fields exists [37].

Overall, it is important to understand how transitional flow in IA geometries affects resultant flow metrics in order to enhance risk of rupture analysis. However, few studies which have sought to evaluate the fundamentals of transition to turbulence in pulsatile flow have been reported. Further, of the ones that have been done, none have used physiologically-relevant pulsatile waveforms. As such, details on the mechanisms that cause the onset and development of transitional flow in physiological pulsatile flow remain unknown [31]. Future work is needed to expound these pulsatile transition mechanisms in order for the effect of such flow on IA growth and rupture to be understood.

1.2.2 Limitations and Gaps Among Current Cerebral Aneurysm Literature

1.2.2.1 Interaction of Morphological and Hemodynamic factors

Studies typically focus on morphological or hemodynamic factors, but do not often consider both. This is in large part because of the nature of current IA data. Databases contain hundreds of geometries and outcomes but no hemodynamic information [38]. This prevents testing or modeling flow fields from the database geometries as inflow and outflow boundary conditions are unknown. Yet, an implicit dependency between morphological and hemodynamic variables is understood and likely contributing to the conflicting results reported [3,6]. For example, Meng et al. [3] determined an interaction between WSS and aneurysm size exists. Further, the AR and the inlet flowrate of an IA would both have an effect on the resultant flow field within the aneurysmal sac, and the contributing magnitude of these two factors would plausibly be different for different IAs. Thus, accurate risk of rupture assessments require a parameter space spanning both morphological and hemodynamic variables independently as well as interactively. Recently, a CFD study analyzed nearly 50 morphological and hemodynamic metrics and their association to risk of rupture using over 1600 patient-specific IA geometries and assuming inflow and outflow boundary conditions [5]. While studies such as this take a critical step of seeking to define quantified relationships between hemodynamic and morphological variables, the use of a single modality, assumption of boundary conditions, and lack of longitudinal data are significant limitations. Ultimately, specific and functional relationships between morphological and hemodynamic variables within an IA remain undefined and substantial work is needed in this area.

1.2.2.2 Modality-Specific Effects on Hemodynamic Analysis

Modalities used to study cerebral aneurysm hemodynamics typically include *in vivo* or *in vitro* 4D Flow MRI, *in silico* CFD, and *in vitro* PIV. Each modality provides a different and unique set of spatiotemporal resolution, noise, accuracy, physiological fidelity levels, as well as assumptions and limitations. *In vivo* 4D Flow MRI maintains the highest level of physiological fidelity as it does not require any segmentation or modeling. However, the low spatiotemporal resolution and high noise of this modality substantially reduces the accuracy of the measured flow fields and any subsequently computed flow metrics. Further, *in vivo* data does not provide any research control. *In vitro* 4D Flow MRI is typically used to analyze the effect of the MRI acquisition sequence and spatiotemporal resolution on resultant hemodynamics, while still

maintaining increased controllability. However, any *in vitro* or *in silico* methodology suffers from segmentation and boundary condition errors and uncertainties. Both PIV and CFD offer high spatiotemporal resolution, but each modality is constrained by assumptions such as Newtonian fluid, rigid walls, and for CFD neglecting gravitational forces and laminar flow.

The effects of these modality-specific ancillary factors on resultant flow analysis remain largely undetermined despite the fact that the few parameters that have been tested were shown to significantly alter hemodynamic metrics. Specifically, decreasing the spatiotemporal resolution has been demonstrated to lower the WSS substantially [15,16]. Further, WSS within an aneurysmal sac has been reported to be statistically significantly different when using a Newtonian vs. non-Newtonian fluid [39]. However, other parameters such as the effect of gravity, and thus aneurysmal orientation, have yet to be investigated and reported. Overall, the aggregate effect of these ancillary factors can alter the flow fields substantially and contribute to the conflicting results that have been reported. Thus, future work is needed to identify specific relationships of modality-induced assumptions and limitations on hemodynamic metrics.

1.2.2.3 Lack of Multi-Modality Studies

One way to evaluate and quantify the effects of modality-specific assumptions and limitations on hemodynamic analysis is through multi-modality studies. For example, conclusions regarding the effect of 4D Flow MRI spatial resolution were only made possible by comparing the *in vitro* 4D Flow MRI to CFD and PIV [16]. Many multi-modality studies involve *in vivo* 4D Flow MRI and CFD. In such studies, CFD is often considered the "ground truth" modality because its substantially higher spatiotemporal resolution implicates higher accuracy. Nonetheless, the 4D Flow MRI undoubtedly has higher physiological fidelity, rendering any "ground truth" modality decision controversial and subjective. Any multi-modality study which utilizes *in vivo* flow data suffers from this lack of "ground truth" issue. Any such study can analyze and compare modalities against each other, but limited conclusions can be drawn when no accepted ground-truth exists. Thus, studies which utilize PIV most often circumvent this issue by restricting themselves to *in vitro* modalities. However, this hinders the clinical translation of findings from such studies. Overall, more multi-modality studies are needed to elucidate and rectify modality-specific effects in an effort to optimally synthesize information by harnessing the strengths of each modality and

compensating for the weaknesses. A data fusion approach such as this can enhance the accuracy, fidelity, and thus clinical utility of *in vivo* hemodynamic assessments.

1.2.2.4 Difficulties of Cerebral Aneurysm Experimental Data

Experimental PIV studies in this domain have been exceptionally limited, preventing many multi-modality studies. Majority of such studies have used planar PIV, measuring only 2-dimensional, 2 velocity component (2D-2C) flow fields. However, IA geometries are highly complex, tortuous, and 3-dimensional, necessitating 3D-3C PIV data. As such, other studies have used "sliced planar" methodologies where planar data is collected at multiple parallel planes (3D-2C) and the third velocity component is reconstructed. Only one volumetric PIV (3D-3C) IA experiment has been reported using a patient-specific geometry and steady flow [15]. In this domain, PIV studies have rarely been used as a stand-alone modality, but instead typically used in a qualitative sense to validate CFD models or compare flow patterns with other modalities. Few PIV studies have reported flow metrics such as WSS or TKE and even less OSI, RRT, pressure, or PWV.

The lack of PIV studies in this domain is due, in part, to the complexity associated with such experiments. The IA geometries contain complex, highly curved walls which make them difficult to manufacture and image. It has been demonstrated that when using a complex geometry, even small disparities between the refractive index (RI) of the model and experimental working fluid can produce significant optical distortion which ultimately results in PIV velocity errors [40]. Thus, the RI of the working fluid must closely match that of the model while also maintaining the fluid properties of blood. For PIV experiments this typically requires the use of additives such as sodium iodide (NaI) which are difficult to work with and expensive. Further, NaI has a high density and produces a working fluid with a density minimally 20% higher than blood. Experimental data also contains unavoidable optical mismatch and noise, requiring robust methods to de-noise the data without compromising the fidelity of the measurements. This is particularly challenging when analyzing transitional flow metrics as contributions from small-scale turbulent flow structures and experimental noise are typically on the same order of magnitude, making them exceptionally difficult to distinguish. Overall, these challenges require substantial time to properly and accurately complete the experimentation, velocity field processing, and post-processing, inherently limiting the number of IA experimental studies reported to date.

1.2.3   Contributions of Current Work

At this point, many major gaps of IA studies, preventing development of robust, universal risk of rupture analysis and contributing to conflicting results within prior literature have been identified. These gaps include:

- uncertainty on the specific influence of transitional flow on the risk of progression and rupture of a cerebral aneurysm.
- the disconnect between morphological and hemodynamic risk factors despite a known interaction of the two.
- inadequate understanding of the effects of modality-specific assumptions, limitations, and spatiotemporal resolution on resultant flow fields and hemodynamic metrics.
- absence of volumetric PIV (3D-3C) data for both IA analysis and CFD validation.

This work aims to bridge these gaps by:

- advancing the understanding of hemodynamic factors that may contribute to IA risk of progression and rupture.
- developing experimental methodologies to alleviate some of the challenges associated with IA PIV experiments.
- conducting volumetric 3D-3C PIV experiments and comparing the data with *in vivo* 4D Flow MRI and *in silico* CFD data in a multi-modality study.

1.3   Structure of Dissertation

This dissertation consists of five manuscripts which collectively deliver on the aims outlined in Section 1.2.3. Chapters 2 and 3 focus on advancing PIV methodologies of IA hemodynamic studies. In Chapter 2, an autonomous proper orthogonal decomposition (POD) based experimental noise reduction technique is formulated and demonstrated, while a novel blood analog solution is introduced in Chapter 3. Chapters 4 and 5 consider and test hemodynamic factors which may contribute to IA risk of rupture but are not well understood. Chapter 4 explores the mechanisms causing the onset and development of transitional flow in pulsatile pipe flow. Chapter 5 demonstrates the influence of hemodynamic parameters including zones of flow recirculation, WSS, OSI, RRT, and PWV in a different cardiovascular region. Finally, Chapter 6 brings together the developed PIV methodologies and hemodynamic metric testing in a multi-modality IA study.

CHAPTER 2. PROPER ORTHOGONAL DECOMPOSITION TRUNCATION METHOD FOR DATA DENOISING AND ORDER REDUCTION

2.1 Abstract

Proper orthogonal decomposition (POD) is used widely in experimental fluid dynamics for reducing noise in a measured flow field. The efficacy of POD is governed by the selection of modes used for the velocity field reconstruction. Currently, the determination of which or how many modes to keep is a user-defined subjective choice, where an arbitrary amount of energy to retain in the reconstruction, such as 99% cumulative energy, is chosen. Here, we present a novel, fully autonomous and objective mode-selection method, which we term the entropy line-fit (ELF) method. The ELF method computes the Shannon entropy of the spatial discrete cosine transform of the eigenmodes, and using a two-line fit of the entropy mode spectrum, distinguishes between the modes carrying meaningful signal and those containing noise. We compare the ELF and existing methods using the analytical Hama flow field, synthetic PIV velocity fields derived from DNS turbulent channel flow data, and experimental particle image velocimetry vortex ring data. Overall, the ELF method improves the effectiveness of POD at removing noise from experimentally measured flow fields and subsequently the accuracy of post-processing calculations.

2.2 Introduction

Proper orthogonal decomposition (POD) is widely used in fluid dynamics for decomposing a dataset into spatial eigenfunctions, known as eigenmodes, and temporal coefficients corresponding to each eigenmode [41,42]. The eigenmodes decompose the data into a set of energy

optimized orthogonal bases [43]. Modes are sorted based on their energy contribution, where the first mode corresponds to the most energetic component of the data set [41].

In particle image velocimetry (PIV) experiments, POD is most often used for reducing random noise in the measured flow field by producing a low-dimensional description of the data. POD for noise reduction has been applied in works such as flow past a backwards facing step [44], perturbed and unperturbed flow over a wall-mounted fence [45], flow through a combustion engine [46], vortex ring formation in radially confined domains [47], and stented arterial flows [30,48]. Removing random noise from a velocity field enables more accurate and robust post-processing calculations such as coherent structures [49], pressure fields [50], or wall gradient estimations for the calculation of wall shear stress [51].

2.2.1   Computing eigenmodes and a reduced-order model

POD decomposes a data series into a spatiotemporal mode basis according to

$$u(x, y, t) = \sum_{n=1}^{T} a_n(t)\phi_n(x, y)$$ (Equation 2.1)

where u is the velocity, T is the number of snapshots, a_n are the temporal coefficients, and ϕ_n are the orthogonal eigenmodes [52]. Equation 2.1 represents an approximation of the flow whose accuracy increases with increasing T and is expected to be exact as T approaches infinity [53]. To compute the eigenmodes of a data set, the mean subtracted velocity fields are formed into a single matrix X, which is of size T x D. The covariance matrix is computed as $R = XX^t$, which is uncorrelated in time [42]. The eigenvalues, λ, and eigenvectors, η, of R are computed and the T eigenmodes are obtained by projecting the eigenvectors onto the data set according to $Y = \eta^t X$. A reduced order model is obtained by reconstructing a representation of the full data set using $N <$ T POD eigenmodes [41].

2.2.2   Current Thresholding Methods

The determination of N is most commonly done using an energy criterion cutoff such that,

$$\frac{\sum_{n=1}^{N} \lambda_n}{\sum_{n=1}^{T} \lambda_n} > E$$ (Equation 2.2),

where λ_n is the eigenvalue of the nth eigenmode and E is the percent of energy in the full data set that the reduced dimensional data set must represent. Often a 99% energy thresholding criterion is used [41], however studies have used a variety of user-defined heuristic values for energy

thresholding varying from 75-99.5% [44–46,48]. Further, the energy criterion will always utilize the first N modes in a reconstruction because mathematically the reconstruction error is shown to be minimal if the largest energy modes are used [54]. However, spurious velocity vectors with large magnitude can corrupt an eigenmode giving it an erroneously large eigenvalue, and thus energy value [55].

Despite these limitations of the energy threshold criterion, only a few studies have investigated improved thresholding alternatives. Epps and Techet (2010) proposed a root mean square (RMS) criterion that preserves only the modes whose RMS velocity is greater than the RMS of the measurement error. Mathematically this thresholding criterion is expressed as

$$\lambda_n{}^2 > \sqrt{DT} * \varepsilon \qquad \text{(Equation 2.3)}$$

where ε is the RMS error of the velocity data. However, with PIV, obtaining the RMS error of the velocity data can often be as difficult as selecting the appropriate number of modes. Raiola et. al. (2015) proposed a turbulent spectrum based approach to identify the optimal cutoff mode to minimize random errors [57]. Mathematically, this thresholding criterion is expressed as

$$\lambda^* = \left(\frac{Tq}{\sigma^2 \zeta(5/3)}\right)^{\frac{3}{5}} \qquad \text{(Equation 2.4)}$$

where λ_* is the optimal mode cutoff, q is the average turbulent kinetic energy (TKE) of the velocity field, σ is the standard deviation of the random error, and ζ is the Euler-Riemann zeta function. Equation 2.4 is not suggested for use with PIV data because the TKE calculation will contain PIV noise errors [58]. The authors instead suggest using a criterion similar to a scree test plot

$$F(k) \approx \frac{\lambda_k}{\lambda_{k-1}} \qquad \text{(Equation 2.5)}$$

Equations 2.4 and 2.5 are approximately mathematically equivalent. The optimal cutoff mode, k*, is identified as the first mode such that $F(k^*) \geq 0.999$ [57]. By computation, F will contain noisy oscillations so discrete wavelets were used to smooth the trend prior to identifying k*. The major drawback of this method is its limited range of applicability [57]. It requires the eigenmodes to be fully and well statistically converged [58] and is only applicable to turbulent data. Additionally, the choice of $F(k^*) \geq 0.999$ remains a subjective thresholding choice. We will refer to this method as the TKE criterion because it is derived from the turbulent spectrum and only applicable to turbulent data.

In this work, we present the first fully autonomous and objective POD threholding criterion. The method proposed here does not require any user inputs and analyzes the full content of spatial eigenmodes. It allows any set of eigenmodes to be used in the reconstruction, such that high-energy measurement error can also be minimized. We first compare this new method with a 95% energy criterion as well as the RMS criterion proposed by Epps and Techet (2010). We then compare the new method with the 90, 95, and 99% energy criteria, and the TKE criterion proposed by Raiola et al. (2015). Finally, we demonstrate the method and its ability to improve post-processing calculations using PIV data of laminar and turbulent vortex rings.

2.3 Improved Thresholding Method

2.3.1 Principles of the proposed method

Inherent to all PIV experiments is random noise, which is non-isotropic and non-homogenous in nature and caused by instrument and velocity measurement errors and uncertainties. Dependent on the source of the random noise, it can contain high or low energy suggesting that little correlation exists between PIV noise and energy, and thus the scalar eigenvalue. Conversely, valuable information is captured in the spatial eigenmode, where POD efficiently compacts patterned information [59]. Relevant flow structures would contain ordered patterns while random noise does not. Thus, as compared to the energy criterion, an improved thresholding method would utilize the information in the spatial eigenmodes to differentiate between the signal and noise content of each mode. Using this idea, the method proposed here quantifies a degree of order of the eigenmodes in order to obtain a representative signal to noise metric for each mode.

Quantifying a degree of order of an image or dataset has often been done using Shannon entropy [60]. Shannon entropy has previously been shown to be an effective method for autonomous coherent structure identification by quantifying vorticity structures [61]. This idea can be extended to POD as a means to quantify the organized structures, or signal, contained in an eigenmode. Shannon entropy is computed by

$$-\sum_{n=1}^{D} x_n * (\log_2 x_n) \qquad \text{(Equation 2.6)}$$

where x is the normalized value of the 2-D eigenmode at a specific point in space. However, a major drawback of Shannon entropy's applicability is that it does not consider the spatial correlation of the values [62]. That is, two images with the same set of pixel intensities will have

26

the same Shannon entropy, regardless of the spatial distribution of the pixels. For this reason, simply computing the Shannon entropy of each eigenmode will identify modes with large scale structures but will not distinguish between small scale organized flow structures and random noise fields whose sets of values are similar. Thus, to increase the robustness and efficacy of Shannon entropy for this application, an intermediate step is needed to transform the eigenmodes into a set of coefficients where the number of coefficients is proportional to the amount of noise in the field. This step can be effectively achieved using a change of basis [61], specifically the discrete cosine transform (DCT). The DCT has often been used for image compression because it is exceptional at pattern recognition and energy compaction [59], enabling organized data structures to be represented in just a few coefficients [63,64]. Meanwhile, random noise will require many coefficients for proper energy compaction due to its lack of structural pattern and high frequency content. The DCT is to some degree, flow structure dependent, such that different flow structures may require a different number of coefficients for proper compaction. Thus, the assumption when employing the DCT for this purpose is that the number of coefficients required to accurately represent any type of flow structure, regardless of organization or boundary domain, is much less than the number of coefficients required to represent random noise. This assumption has previously been shown to be reasonable in not only image processing, but also 1-D signals, where physical modes have compacted to generally a small number of coefficients [63]. The validity of this assumption is also shown in Figure 2-1a-d, where the first U and V eigenmodes contain significantly different flow structures, but similar DCT coefficient fields. The major implication of this assumption is that the number of non-zero coefficients in the DCT field is approximately proportional to the amount of random noise in the eigenmode. This makes the DCT an excellent choice for implementing a Shannon entropy-based POD thresholding criterion. However, it is important to note that any change of basis transform could be substituted here. Thus, comparisons between using, for example, the FFT or wavelet transform in place of the DCT could be explored in future work.

The DCT is computed by

$$F_{mn} = \sum_{i=0}^{D_x} \sum_{j=0}^{D_y} x_{i,j} * cos\left[\frac{\pi}{D_x}\left(i + \frac{1}{2}\right)m\right] cos\left[\frac{\pi}{D_y}\left(j + \frac{1}{2}\right)n\right] \qquad \text{(Equation 2.7)}$$

where $x_{i,j}$ is the value of the eigenmode at the spatial point (i, j).

These two computations, the DCT and Shannon entropy, are the foundation of the proposed method schematically represented in Figure 2-1. First, the DCT of the U and V velocity
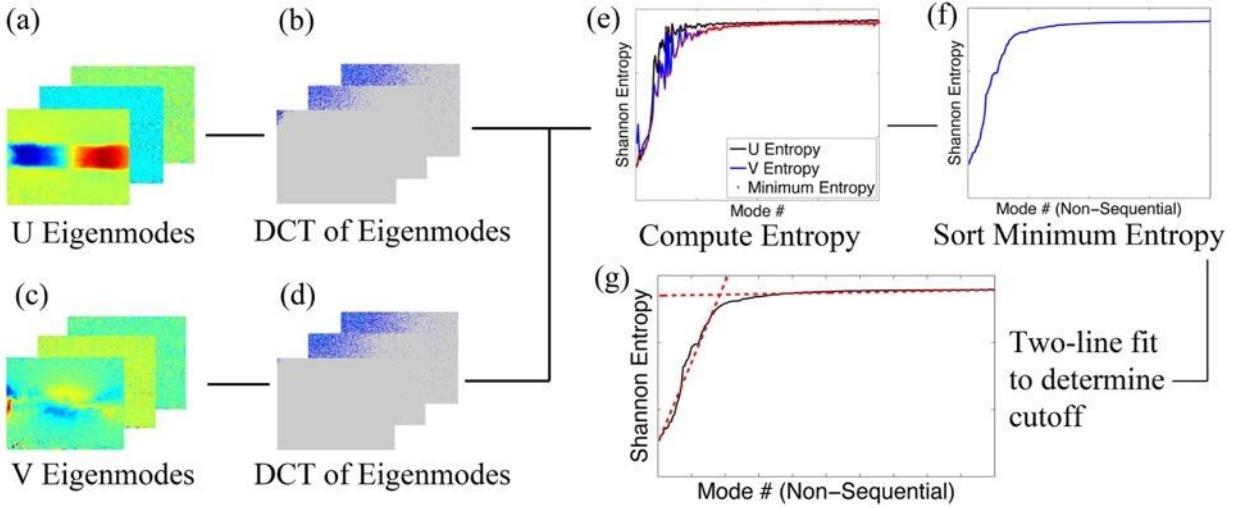
Figure 2-1: Schematic of the proposed thresholding method.

eigenmodes are computed, as in Figure 2-1b and 2-1d, according to Equation 2.7. The Shannon entropy of the DCT of each eigenmode is then computed using Equation 2.6 in order to quantify the representative signal to noise ratio of the eigenmode. Between the U and V eigenmodes, the minimum entropy value is taken as illustrated in Figure 2-1e. The entropy values are then sorted from smallest to largest as in Figure 2-1f so that any set of eigenmodes can be kept, rather than just a sequential set.

The final step is to determine the optimal cutoff mode based on the sorted mode entropy values. The majority of experimental cases will yield a trend similar to that seen in Figure 2-1f, where a plateau in the entropy is observed. This plateau occurs because the maximum entropy in the eigenmode, where each value occurs only one time, has been reached. At that point, adding additional modes provides minimal information because no patterns and thus relevant flow structures can exist in such an eigenmode. The POD is considered to have converged if this entropy
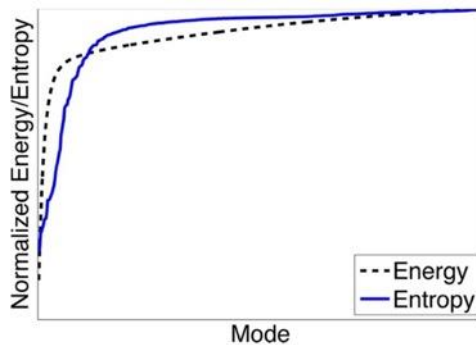
Figure 2-2: Comparison of energy vs. entropy plateau.

plateau is observable. If it is not, then more snapshots are needed to achieve an accurate reduced-order model. The entropy plateau is generally more prominent and easy to identify than the energy plateau as shown in Figure 2-2.

The plateau point can be identified using a two-line fit. The two-line fit procedure was used because the shape of the mode entropy curve is known and will always abide well to a two-line fit because it plateaus. The two-line fit proved to be more accurate and robust than the commonly used change-point analysis. It also requires no user-selected heuristics, yielding the simplest implementation procedure.

The two-line fit procedure is schematically represented in Figure 2-3. To compute the two-line fit, we select a data point of the 1-D signal, for example the one marked by 'X' in Figure 2-3a. Two polynomial line fits are computed: one using the data points 1 to X, the other using the data point X to the end of the signal. Using the set of points on the two fitted lines, represented by the dotted lines in Figure 2-3a, we have a set of predicted values for each point in the signal. The error, Σ, is then computed as the sum of the difference between the predicted values and actual values of the data. The R^2 values of the two fitted lines are also computed and averaged. This procedure is iterated for all points in the signal, as demonstrated in Figure 2-3b. The ideal fit will minimize the error and maximize the average R^2 value of the two lines. Thus, the optimal cutoff is selected as the point where R^2/Σ, shown in Figure 2-3c, is maximized. Because the entropy curve will never be perfectly symmetric, a unique solution to the two-line fit will always exist. The two-line fit method has shown to be a robust method, requiring no user tuning, for experimental data.

Overall, the proposed cutoff method computes the signal to noise ratio of the individual 2-D spatial eigenmodes using the discrete cosine transform and Shannon entropy, and selects the
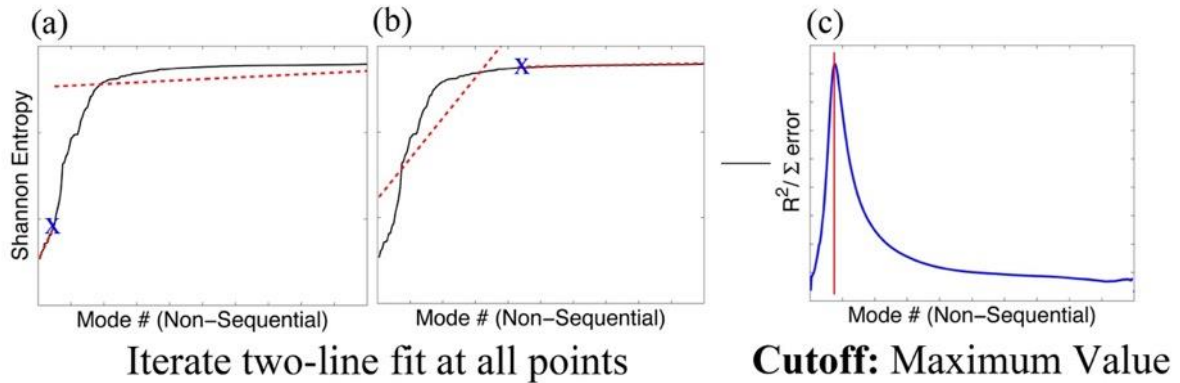
Figure 2-3: Schematic of the proposed two-line fit method to autonomously determine the optimal cutoff mode.

mode cutoff as the point where the maximum entropy plateau is first reached using the two-line fit. For brevity, for the remainder of this paper, we will refer to this method as the entropy-line fit (ELF) criterion.

2.3.2 Limitations of the ELF POD Thresholding Criterion

There are some notable limitations to POD and the ELF criterion. The data de-noising being described here only refers to random errors and does not include bias errors, which is beyond the scope of this work. Further, both POD and the ELF criterion in principle do not consider the boundary conditions of the flow domain, which may induce some errors in the ROMs.

An inherent assumption when using POD is that the number of snapshots inputted can accurately represent the modes in the flow field. In reality, considering the classical view of POD (Equation 2.1), an infinite number of modes are required for an exact representation of the data. Yet, this assumption is most often acceptable because POD converges quadratically and faster than any other expansion [65], so the smaller-scale modes that are primarily affected by the deficiencies of this assumption are already un-observable due to the limited PIV spatial resolution. Still, physically this means that eigenmode representations of the small-scale modes in the flow field changes based on the specific input and number of snapshots provided. Determining the optimal input and procedure to obtain the highest fidelity POD eigenmodes is the subject of methods such as shift and double POD [66]. Such methods can also be used in conjunction with the methodology presented herein. However, investigating the performance of these methodology variations is beyond the scope of this paper. Thus, it is important to note that the modes preserved by the ELF criterion represents the set of eigenmodes predicted to produce the reduced order model with the highest fidelity and accuracy for the given input. As such, the number of modes kept by the ELF criterion does not necessarily reflect the number of modes that actually exist in the flow. Additionally, because of these complexities, estimating the random error of the raw data or reduced order model of the data is a difficult task which could be explored in future work, but is beyond the scope of the work here.

As previously indicated, if an insufficient number of snapshots is inputted, the entropy will not converge to the maximum entropy plateau because not all large-scale modes can be accurately represented, as shown in Figure 2-4b. In such a case, the two-line fit, and ultimately the ELF criterion, will fail. The two-line fit could fail in cases where analytical signals with little to no

noise are used because these can produce intermediate plateaus in entropy, as seen in Figure 2-4a. Both of these cases cause the two-line fit to fail because they induce multiple peaks of the R^2/Σ curve, as shown in Figure 2-4c. A peak-to-peak ratio (PPR) can be computed to determine if the two-line fit failed. Through several trial cases, a PPR of less than 1.8, as observed in Figure 2-4c, was found to yield erratic results and thresholding selections. In this case, one possible way the cutoff can be determined is using only the second line fit (i.e. the line fitting the points from X to the end of the signal), as shown in Figure 2-4d. The cutoff is selected as the first point where Σ of the line defining the data points from X to the end of the signal is less than some tolerance, such as 0.1. This method will be employed in the work shown here. If it is desired to use the ELF criterion extensively with analytical signals, other cutoff identification algorithms, in place of the two-line fit, should be explored, but this is beyond the scope of this work.
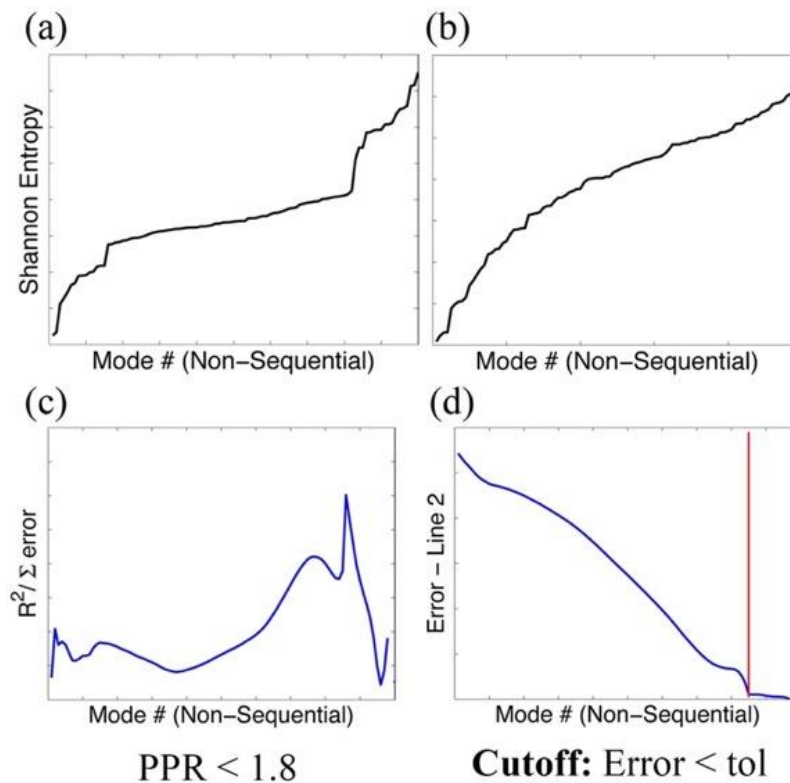
Figure 2-4: Demonstration of situations where the two-line fit may fail: (a) intermediate entropy peaks possible when using analytical signals, (b) an insufficient number of snapshots input such that the modes have not statistically converged. (c) Suggested peak-to-peak ratio check to determine if peak found is valid, (d) alternative way to identify optimal cutoff mode if original peak found is invalid.

2.4   Materials and Methods

Analysis using analytical, synthetic, and experimental flow fields was done to compare the energy, RMS, TKE, and ELF criteria. For the analytical and experimental analysis, a 95% energy threshold was applied. However, the 90% and 99% mode cutoffs are also reported for the experimental analysis.

2.4.1   Analytical Hama Flow Field

An analytical flow field for which a known number of modes and an exact solution exist was used to compare the criteria. A 2-D perturbed shear flow introduced by Hama (1962) was chosen as the analytical flow field because it contains both steady and turbulent fluctuation components. The flow field is governed by the following equations.

$$U(x, y, t) = u_0(x, y, t) + u'(x, y, t)$$

$$V(x, y, t) = v_0(x, y, t) + v'(x, y, t) \qquad \text{(Equation 2.8)}$$

$$u_0(x, y, t) = 1 + \tanh{(y)}, \qquad v_0(x, y, t) = 0 \qquad \text{(Equation 2.9)}$$

$$u'(x, y, t) = 2a \operatorname{sech}(y) \tanh(y) * \sin{(\alpha\,(x - ct))}$$

$$v'(x, y, t) = 2a \operatorname{sech}(y) * \cos{(\alpha\,(x - ct))} \qquad \text{(Equation 2.10)}$$

where c was a constant (set to 3) for the analysis. The variables a and α were adjusted from 2e-4 to 0.2 and 6.7 to 90, respectively, controlling the mode amplitudes and characteristics. The velocity grid was defined from 0 to 8 and -0.2 to 0.2 in the x and y-directions, respectively. This corresponded to 2000 vector points in the x-direction and 100 in the y-direction. One hundred velocity fields were used, for time defined from 0 to 5. An example Hama flow field is shown in Figure 2-5.
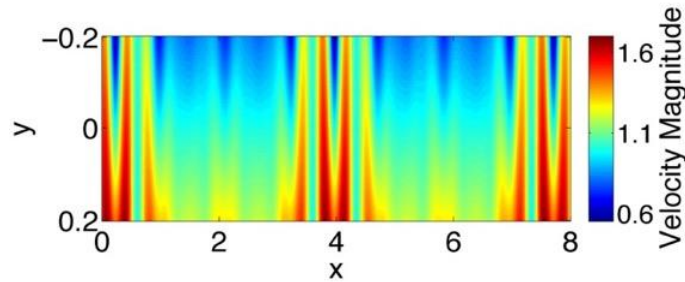
Figure 2-5: Sample Hama flow velocity field.

The analytical flow fields were corrupted with various levels of multiplicative noise. We define δ as the number of modes that exist in the flow field, φ as the ratio of the amplitude of the largest mode to the amplitude of the smallest mode, and ω as the ratio of the amplitude of the noise to the amplitude of the smallest mode. The amplitude of the noise and modes were defined by their average velocity magnitude. The performance of each thresholding criterion was evaluated by β, the number of modes kept for the reconstruction, and the L^2 relative error between the reconstructed velocity fields and the exact velocity fields. The L^2 relative error was computed as

$$L_{rel}^2 = \sqrt{\frac{\sum_{n=1}^{D}(V_{R,n}-V_{E,n})^2}{\sum_{n=1}^{D}(V_{E,n})^2}}$$ (Equation 2.11)

where V_E is the exact velocity and V_R is the reconstructed velocity. L_{rel}^2 was computed for both the U and V velocity fields and then averaged to obtain the mean error in the velocity field components. This parametric evaluation tested the number of modes successfully detected by each criterion, the dynamic range of each criterion, and each criterion's ability to remove noise while preserving valid flow structures.

2.4.2 Synthetic PIV Images of DNS Data

In principle, PIV noise is not truly multiplicative. Thus, velocity fields processed from synthetic PIV images were used to test the ELF method with higher-fidelity PIV noise. The synthetic PIV particle images created by Raiola [57] were used here. All pertinent information is given here, but the reader should refer to Raiola et al. (2015) for additional specific details on the synthetic PIV images and processing. The images were generated based on DNS channel flow velocity field data publicly available from the Johns Hopkins turbulence database [68–71]. The particles were created according to a Gaussian laser intensity profile. Uniform noise was added to the images. The images incorporated only two components of the velocity field and contained some out-of-plane effects to best mimic a planar PIV experiment. The images were time-resolved and corresponded to 8000 velocity fields, or snapshots. Multi-pass PIV processing was performed with the final pass using a 32 x 32 window size and an 8 x 8 velocity grid size. The spatial resolution of the velocity fields was 125 x 125 vectors. Pixel displacement was adjusted to be around 15 pixels per frame, as is typical in a PIV experiment. Standard deviation of the random error was estimated at 0.18 pixels [57]. The DNS velocity fields were considered the true solution which all computed L^2 relative errors were compared against. The synthetic PIV data set was used

to evaluate the effect of varying the number of snapshots inputted as well as reducing the grid resolution by subsampling the data.

2.4.3   Experimental Methods

2.4.3.1   Data Collection and Processing

Experimental semi-infinite vortex ring data was used to compare each thresholding method and demonstrate the applicability of the ELF method on experimental data. Semi-infinite vortex ring data was chosen because this flow field has been extensively studied with well-documented empirical values of its core metrics, and in-depth understanding of the governing physics. One laminar vortex ring case, with a piston stroke to piston diameter ratio, L/D_0, of 1.0 and Reynolds number of about 1400, and one turbulent vortex ring case, with an L/D_0 of 3.0 and Reynolds number of about 7000, were used. Velocity fields for the vortex rings were collected using planar time-resolved PIV. Velocity fields were collected downstream of the piston cylinder arrangement and in the plane intersecting the center of the piston. Captured images were of size 1,280 x 800 pixels with a magnification of 62 µm/pixel. Image pairs were captured at 500 Hz with inter-frame times of 1000 µs and 450 µs for the laminar and turbulent cases, respectively. Flow was seeded with 11 µm neutrally buoyant glass spheres. Additional details of this experiment are reported in Stewart and Vlachos (2012).

PIV data was re-processed for the current work, differing from that reported in Stewart and Vlachos (2012). Images were processed using an in-house PIV software Prana (https://github.com/aether-lab/prana). An iterative image deformation algorithm [72] and robust phase correlation [73–75] were used. Three passes were performed, with the final pass using a 16 x 16 pixel window and 4 x 4 grid resolution, yielding a 199 x 319 vector velocity field. All PIV passes were validated using a median-based universal outlier detection with a 7 x 7 window size [76]. Uncertainty in the velocity fields was quantified using a correlation peak to peak ratio method described in Xue et al. (2014) and Charonko and Vlachos (2013). Uncertainty was computed using both the 1σ (68.5%) and 2σ (95%) confidence intervals. Detected outliers were not included in the uncertainty calculation. For the laminar vortex ring case, uncertainty was estimated at 0.08 and 0.21 pixels for the 1σ and 2σ confidence intervals, respectively. For the turbulent vortex ring case, uncertainty was estimated at 0.07 and 0.17 pixels for the 1σ and 2σ confidence intervals, respectively. The 2σ confidence interval uncertainty values were used for the RMS thresholding

criterion in all subsequent analysis, but the number of modes kept using the 1σ cutoff is also reported.

2.4.3.2 Post-Processing Calculations

Vorticity, area, and circulation of the core regions of the vortex rings were subsequently computed. All calculations were done for the positive core and negative core individually and then the two were averaged. Vortices were identified using the λ_{ci} criterion [79], which identifies the imaginary portion of the eigenvalue computed from the velocity gradient matrix at a vector point. A 3.0% of the maximum value thresholding criterion was used to eliminate falsely identified vortices, which are the result of measurement error or experimental noise. Velocity gradients for both the vortex identification and the vorticity calculations were computed using a compact noise optimized Richardson finite difference scheme [80]. After computing the vorticity fields, core vorticity was computed as the 99_{th} percentile of the maximum vorticity value, to prevent possible large outlier values from contaminating the calculation. An equivalent diameter was computed using the area in pixels identified by the λ_{ci} output. The core area was then computed as the area of a circle with the equivalent diameter. Circulation was computed two ways, using both the line integral of the velocity, Equation 2.12, and the area integral of the vorticity, Equation 2.13.

$$\Gamma = \oint_C V \cdot n \, dl \qquad \text{(Equation 2.12)}$$

$$\Gamma = \int_A \omega \cdot n \, dS \qquad \text{(Equation 2.13)}$$

Mathematically, these two methods should produce the same value of circulation, however, based on experimental noise and noise from the differentiation, discrepancies can occur. Expected circulation values were computed using both the slug-flow approximation with the correction given in Shariff and Leonard (1992), and using the formation numbers reported in Stewart and Vlachos (2012) and the results of the slow-ramp case in Gharib et al. (1998). Both methods were found to be in good agreement and thus the slug-flow with correction calculation was used. The expected circulation values were 22.5 ± 0.76 cm2/s for the laminar case and 55.9 ± 0.43 cm2/s for the turbulent case.

2.5 Results and Discussion

2.5.1 Parametric study using analytical flow field

Using the analytical Hama flow field, three tests were performed to evaluate how each thresholding method performed for various numbers of modes, dynamic ranges, and noise levels. The number of modes and dynamic range tests were done using no noise and 5 and 20% multiplicative noise. The 5 and 20% noise levels were chosen as representative low and high levels of experimental noise. Additive Gaussian noise was also tested and produced similar results and conclusions, indicating a robustness of the thresholding criteria to various noise types. Thus, only the multiplicative noise is shown here. For all tests the RMS threshold was set to the noise level added (or 1E-4 for the 0% noise cases) multiplied by the mean velocity magnitude of the flow.

2.5.1.1 Number of Modes Test

Figure 2-6 illustrates the number of modes each criterion was able to detect for various Hama flow fields containing 2 to 120 equal amplitude modes. With only 100 snapshots being used, this test demonstrates the behavior of each method when the POD eigenmodes are not statistically converged. Figures 2-6a and 2-6b show similar trends. The RMS criterion performed best, correctly identifying the number of modes in the flow field until the number of modes extended beyond the number of snapshots, at which point it kept all modes. With no noise added, the ELF method followed the correct number of modes until 78 modes existed in the flow field ($\delta/T = 0.78$), at which point it deviated to keeping 98 modes. With 0 and 5% noise added, once the number of modes exceeded the number of snapshots, the ELF method displayed erratic cutoff mode selections oscillating between keeping about 44 modes or above 90 modes. This occurred because of the previously discussed issue of intermediate entropy plateaus in the mode entropy signal, causing similar error values for all possible cutoff mode selections. Ultimately, this corrupts the selection of the optimal cutoff mode and yields a reconstruction with unpredictable error. This behavior was only observed with analytical flow fields. However, this issue was less pronounced when a high level of noise existed in the analytical flow field because the noise reduced the intermediate entropy plateaus, as evident in Figure 2-6c. The 95% energy criterion began to under predict the number of modes with 18, 26, and 46 modes existing in the flow field ($\delta/T = 0.18$, 0.26, 0.46) at 0, 5, and 20% noise added, respectively. Although the number of modes tested revealed some limitations of the ELF method, in a practical sense, all modes in a flow field will

not have the same amplitude and there will be a dependence on the amplitude ratio the modes maintain.
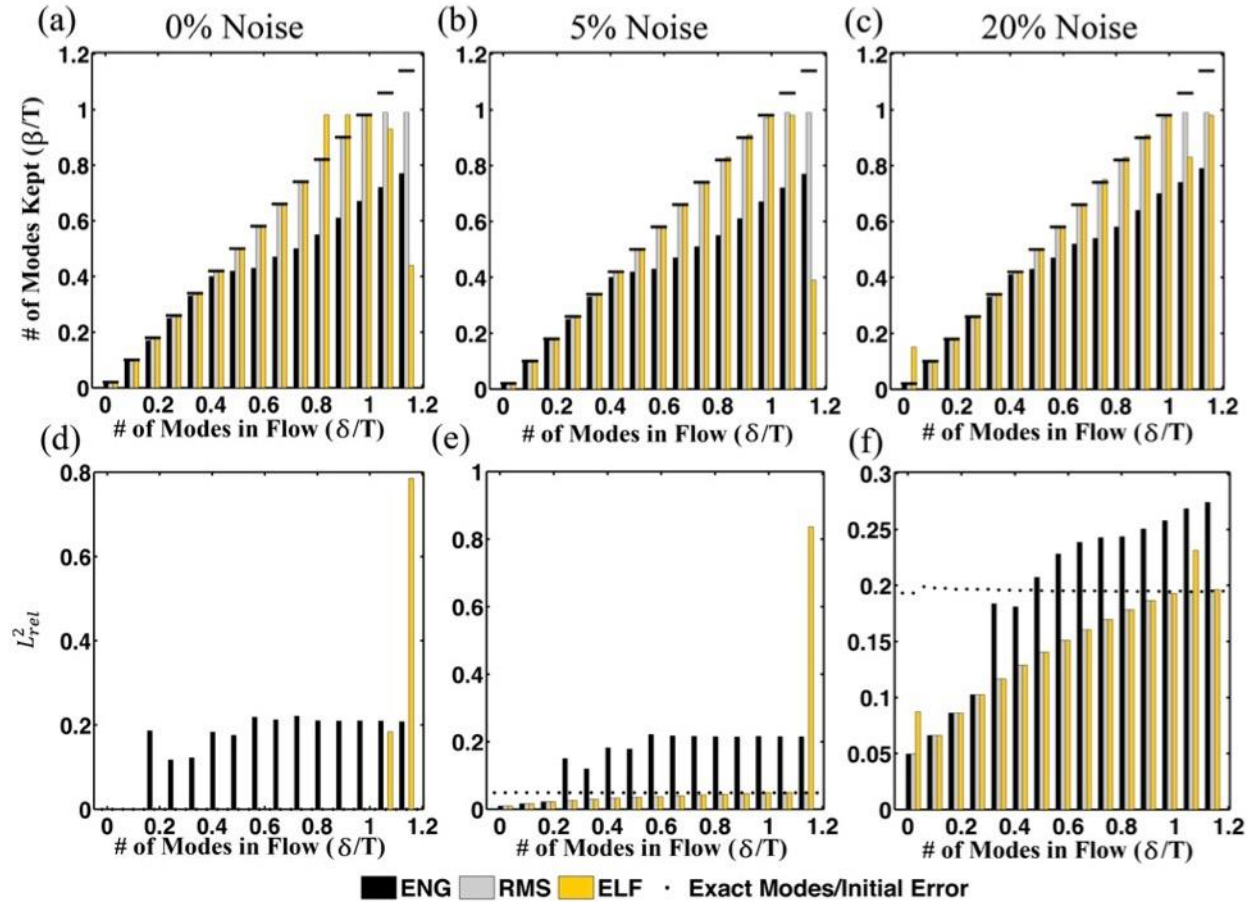
Figure 2-6: Number of modes kept, β, and the L2rel error between the reconstructed velocity fields and the exact velocity fields, as a function of the number of modes in the flow field, δ.

2.5.1.2 Dynamic Range Test

The dynamic range test is particularly important for high shear, unsteady, and spatiotemporally varying flows. To analyze the dynamic range of each method, Hama flow fields were created using various amplitude ratios, each with 12 modes. The amplitude ratio was varied from 1 to 150. The results of this analysis are given in Figure 2-7. Trends were similar for amplitude ratios above 50 and thus only amplitude ratios up to 50 are displayed in Figure 2-7.

With no noise added, the RMS criterion continued to outperform the other methods. In Figure 2-7a, the energy and ELF methods with no noise added deviated at amplitude ratios of 1.67 and 5, keeping 8 and 98 modes, respectively. In this case, the DCT of each eigenmode is similar,
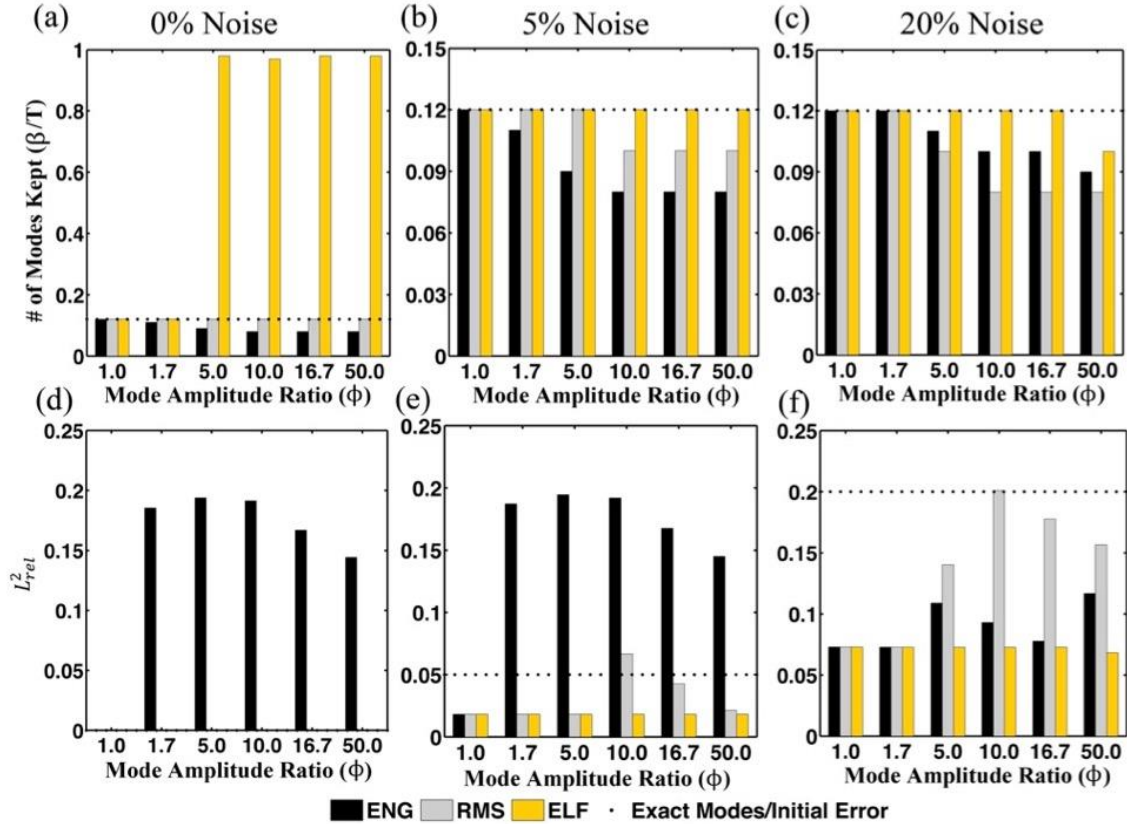
Figure 2-7: Number of modes kept, β, and the L2rel error between the reconstructed velocity fields and the exact velocity fields, as a function of the ratio of the amplitude of the largest mode to the amplitude of the smallest mode in the flow field, φ.

with most coefficients equaling zero, when no noise exists in the flow field. The signal to noise ratio is essentially infinite causing the Shannon entropy to quantify all fields as maintaining similar entropy, damping any significant change in the entropy trend. The increasing amplitude ratio also diminishes the significance of the entropy plateau point, which is why the ELF method predicts 98 modes at high amplitude ratios and no noise. Yet, because no noise exists in the flow, this over-prediction produced no reconstruction error. In Figures 2-7b and 2-7c, at 5 and 20% noise, the ELF method maintained the correct number of modes in the flow field until amplitude ratios of 125.0 and 50.0, respectively. Meanwhile, with 5% noise added, the energy and RMS methods began to under-predict the number of modes at amplitude ratios of 1.67 and 5.0, respectively. Thus, since realistically experimental flow fields would contain some noise, both of these methods would eliminate much of the small-scale turbulent spectrum. In general, the ELF method demonstrated major improvements over the RMS and energy criteria by expanding the dynamic range it was able to reconstruct.

2.5.1.3 Noise Level Test

      The noise level test explored the ability of each criterion to detect differences between the small amplitude modes that contain relevant flow structures and those that contain primarily noise. Flow fields with 12 modes and an amplitude ratio of 10 were used for this analysis.
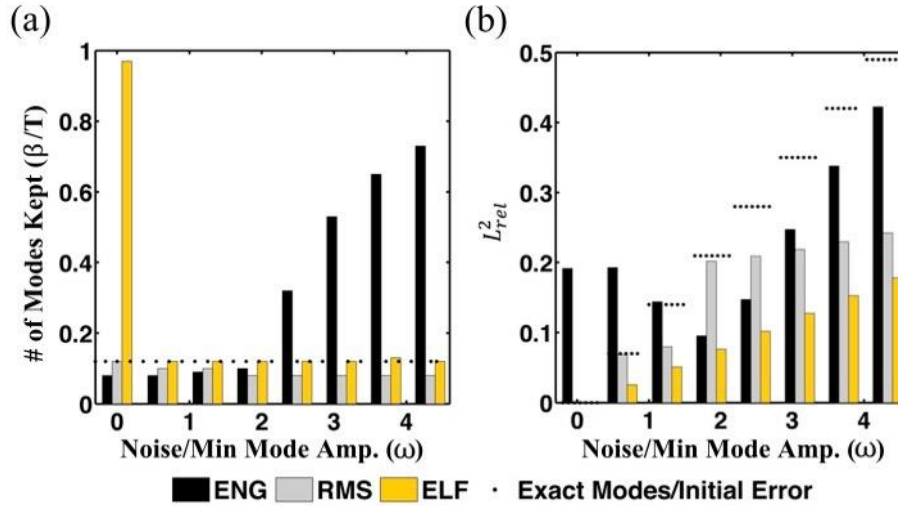
Figure 2-8: Number of modes kept, β, and the L2rel error between the reconstructed velocity fields and the exact velocity fields, as a function of the ratio of the amplitude of the noise added to the amplitude of the smallest mode in the flow field, ω.

      Figure 2-8 illustrates the results of this analysis. The ELF method was able to predict the correct number of modes, even with 50% noise. In Figure 2-8a, with the exception of no noise added, where the ELF method over-predicted as explained in Section 2.4.1.2, the ELF method was able to detect all of the correct modes even as the noise level extended beyond the lowest amplitude mode in the flow field ($\omega > 1$). The corresponding error, in Figure 2-8b, increased linearly as the noise began to corrupt the modes containing flow structures. Meanwhile, the RMS criterion began to under-predict the number of modes in the flow field at a noise to mode amplitude ratio of 0.24. Thus, the RMS criterion, although it detected large-scale flow structures, by design could not distinguish differences between noise and flow structures among modes of similar, low energy. With the energy criteria, as the noise to mode amplitude ratio and thus the noise in the flow field increased, more modes were kept. Aside from the subjectivity of the criterion, this exposes a detrimental drawback of the fundamental principle underlying the energy thresholding method. That is, random noise in the flow field causes the mode energy to be more uniformly distributed across all modes, obscuring energy differences between the noise and flow structures. Further,

because the energy criterion only considers the amplitude of eigenvalues whose magnitude is relative and subject to both flow structures and noise, the energy criterion becomes corrupted by this uniform distribution, keeping more modes, rather than less, as error in the flow field is increased. Although the RMS method also only considers the amplitude of eigenvalues, it uses an absolute thresholding value, rather than a relative one, so it is not corrupted by the high noise. Overall, in this analysis the ELF method demonstrated significant improvements as compared to the RMS and energy criteria.

2.5.2 Method comparisons using synthetic PIV images of turbulent channel

The performance of each method with synthetic PIV velocity fields was evaluated by the reconstruction error and power spectra. The DNS solution and raw PIV processed velocity fields are denoted by 'True' and 'PIV' in this work, respectively.

2.5.2.1 Evaluating the effect of number of snapshots

Altering the number of snapshots input to the POD varies the eigenmode solution obtained and the statistical convergence of the eigenmodes. To evaluate the performance of each method for varying levels of statistical convergence, POD was performed using 8000, 6000, 4000, and 2000 snapshots. Table 2-1 contains the optimal number of modes identified by each thresholding method. The minimum reconstruction error listed in Table 2-1 indicates the number of sequential modes that minimized the L^2 relative error. Because the noise added to the PIV images was uniform and known, it can be reasonable expected that a sequential set of eigenmodes produced approximately the minimal reconstruction error.

Figure 2-9 illustrates the L^2 relative error as a function of the number of sequential modes retained for the reconstruction. The number of eigenmodes kept and associated error for each thresholding method is also shown in Figure 2-9.

The 2000 snapshot case was the only one not considered converged with reference to the original model. For all converged cases, the TKE criterion chose a similar number of modes to keep, with the slight variances attributed to the discrete wavelet smoothing used. In the unconverged case, the TKE criterion over-predicted the number of modes to keep, keeping almost all snapshots and adding 13.0% error from the minimum achievable error. Meanwhile, the ELF method added 1.9% error. For the 8000 and 6000 snapshot cases, the TKE and ELF methods

performed best with less than 1% increases from the minimal achievable error. For the 4000 snapshot case, the ELF method performed optimally, yielding the minimum achievable error, while the TKE method added 1.7% error. For the 8000 snapshot case, the 90, 95, and 99% energy cutoffs respectively added 59.0, 7.9, and 18.7% error from the minimum achievable error, with similar error increases for all other cases. The RMS method failed here because of the large number of snapshots and low error, inducing a nearly three-fold increase in error for all cases.

Table 2-1: POD mode information for synthetic wall turbulence data with varying snapshots.

Number of Snapshots	8000	6000	4000	2000
Method	# Modes Kept	# Modes Kept	# Modes Kept	# Modes Kept
Energy 90%	270	259	248	225
Energy 95%	707	660	602	486
Energy 99%	3359	2859	2226	1342
RMS Criterion	1	1	2	2
TKE (Raiola et al, 2015)	1253	1284	1269	1936
ELF*	1383	1201	992	636
Min. Reconstruction Error	*1159*	*1099*	*990*	*811*

*ELF criterion keeps non-sequential modes: for 8000 case, keeps 1-1309, 1311-1340, 1342, 1343, 1345-1352, 1356-1359, 1363-1368, 1370, 1372, 1373, 1375-1379, 1384, 1385, 1387, 1390, 1393, 1395-1397, 1404, 1406-1408, 1417, 1419, 1420, 1428, 1445, 1471
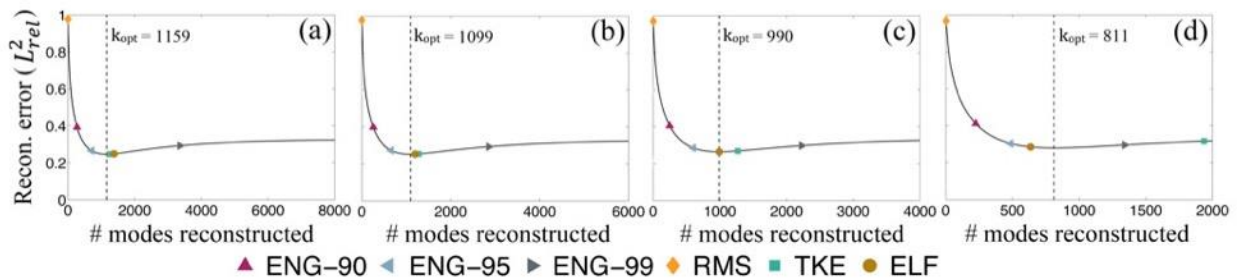
Figure 2-9: The L2rel error between the reconstructed velocity fields and the true (DNS) velocity fields, for (a) 8000 snapshots, (b) 6000 snapshots, (c) 4000 snapshots, and (d) 2000 snapshots inputted.
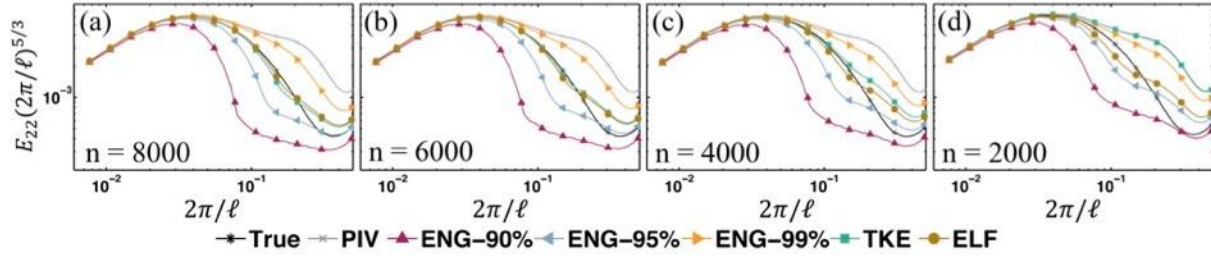
Figure 2-10: Power spectra for (a) 8000 snapshots, (b) 6000 snapshots, (c) 4000 snapshots, and (d) 2000 snapshots inputted.

Figure 2-10 shows the power spectra for all cases and all thresholding methods. The RMS method was excluded because of its excessive error. Figure 2-10 demonstrates that as the number of snapshots decreases, so too does the ability of even the optimal POD reduced order model to accurately represent the turbulent power spectra. The true solution indicated in Figure 2-10 varies with the number of snapshots inputted. In Figures 2-10a-2-10c, the TKE and ELF methods best maintained the turbulent spectra. The 90 and 99% energy criteria demonstrate the consequence of keeping too few and too many modes. Overall, Figure 2-10 shows that the ELF method best adapted to the number of snapshots inputted and varying statistical convergence, being the only method to yield the optimal reconstruction for all cases. This illustrates a major limitation of the TKE method that full statistical convergence of the eigenmodes is required for accurate results.

2.5.2.2   Evaluating the Effect of Spatial Resolution

Varying the spatial resolution by subsampling the velocity grid demonstrates how each method performed under different levels of discretization. It is important to note that subsampling produces a different effect than varying spatial resolution by increasing the PIV grid size. The effect of increasing the grid size from 8 x 8 to 16 x 16 was explored in Raiola et al. (2015) and found to produce minimal differences [57].

Table 2-2 provides the number of modes kept by each method for the 125 x 125, 100 x 100, 75 x 75, and 50 x 50 vector grid sizes. For all spatial resolution cases, 8000 snapshots were used. As the discretization resolution decreased, the smallest observable turbulent length-scale increased. Thus, the optimal number of modes expectedly decreased. Again, the TKE method retained essentially the same number of modes for all resolution cases.

Figure 2-11 illustrates the reconstruction error for each case based on the number of sequential modes retained. As the resolution decreased, the plateau following the minimum

reconstruction error became flatter, meaning keeping too many modes was preferable to keeping too few. All methods performed similarly across all different lower resolution cases. The 90, 95, and 99% energy criteria increased the error by approximately 53, 7, and 16% above the minimum possible reconstruction error, respectively. The TKE and ELF again outperformed all other methods, maintaining added errors on average of 1.0 and 1.3%, respectively.

Table 2-2: POD mode information for synthetic wall turbulence data with varying spatial resolution.

Vector Grid Size	125 x 125	100 x 100	75 x 75	50 x 50
Method	# Modes Kept	# Modes Kept	# Modes Kept	# Modes Kept
Energy 90%	270	269	269	270
Energy 95%	707	689	691	672
Energy 99%	3359	3132	2991	2474
RMS Criterion	1	2	1	1
TKE (Raiola et al, 2015)	1253	1345	1304	1249
ELF*	1383	1457	1445	1076
Min. Reconstruction Error	*1159*	*1106*	*1102*	*1029*
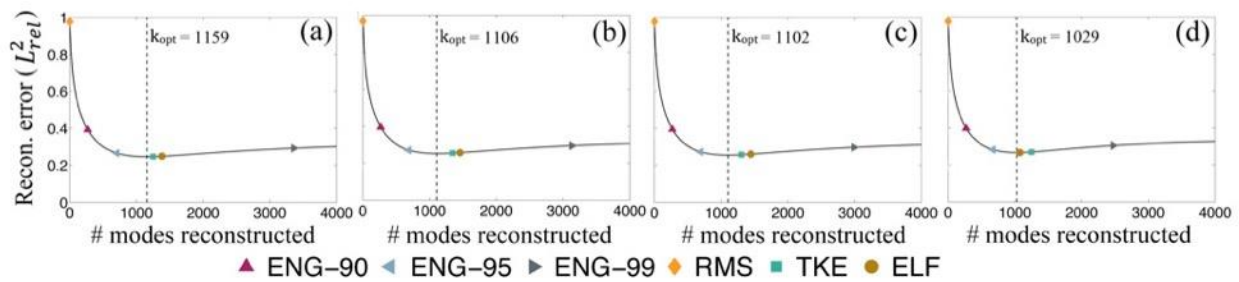
Figure 2-11: The L_{2rel} error between the reconstructed velocity fields and the true (DNS) velocity fields, for (a) 125x125, (b) 100x100, (c) 75x75, and (d) 50x50 vector grid resolution.

Figure 2-12 shows the power spectra for each resolution case. In general, the TKE and ELF methods produced similar spectra for all cases. For the 50 x 50 resolution case, despite the ELF method having the lowest reconstruction error, the TKE method maintained a slightly improved

spectrum, as observed in Figure 2-12d. Overall, all methods were not affected by the changing resolution of the discretization, indicating that the POD thresholding will perform the same regardless of vector grid spacing.
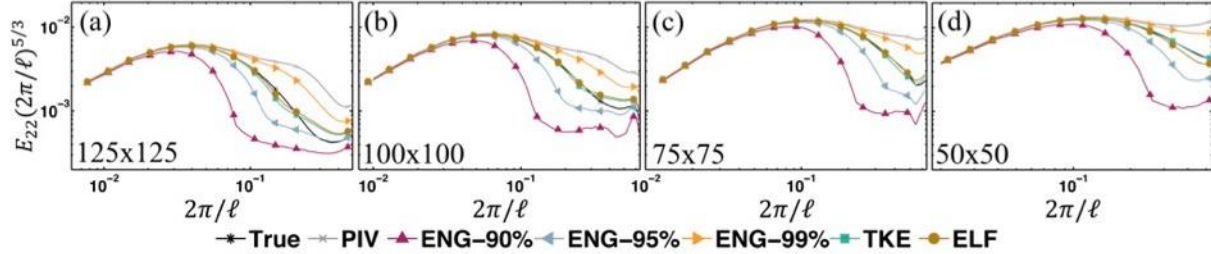
Figure 2-12: Power spectra for (a) 125x125, (b) 100x100, (c) 75x75, and (d) 50x50 vector grid resolution.

2.5.3 Method comparisons using experimental vortex ring data

While the ELF method demonstrated advantages and limitations using the analytical and synthetic flow fields, its efficacy using experimental flow fields must be evaluated. Each thresholding method was applied to vortex ring PIV measurements. Three commonly used spatial filters including a Gaussian filter, Savitzky-Golay filter [83–85], and Wiener filter [86,87] were also applied to the PIV measurements. All filters used a 5x5 kernel size. For the Wiener filter, this kernel size is an aggressive smoothing procedure. Relevant post-processing calculations were subsequently computed for all POD and spatial filtering cases and compared. Analysis was done using the raw PIV data as a reference and is denoted as 'Measured'. When applicable, the Gaussian, Savitzky-Golay, and Wiener filters are denoted as 'GF', 'SG', and 'WF', respectively. The POD mode information for the experimental vortex ring cases is summarized in Table 2-3. The RMS method was implemented using Equation 2.3 and the 1σ and 2σ values given in Section 2.3.3.1. For all methods, the laminar vortex ring case required more modes than the turbulent case. This could be the result of the higher uncertainty in the laminar case or the inability of the PIV spatiotemporal resolution to capture the small-scale turbulent structures. For both the laminar and turbulent cases, the ELF criterion does not keep sequential eigenmodes. For the turbulent case, the TKE method maintained almost all modes indicating that the data was not well enough converged for this to method to yield accurate results. Thus, the TKE method was excluded from post-processing calculations.

44

Table 2-3: POD mode information for experimental vortex ring data.

Method	# Modes Kept (500 Snapshots)	
	L/D = 1.0	L/D = 3.0
Energy 90%	140	116
Energy 95%	277	260
Energy 99%	442	440
RMS Criterion (95% RMS)	7	6
RMS Criterion (68.5% RMS)	13	9
TKE	-	436
ELF*	62	38

*ELF criterion keeps non-sequential modes: For L/D=1.0, keeps 1-60, 63, 66. For L/D=3.0, keeps 1-24, 26, 28, 29, 31-35, 38-40, 42, 46, 47
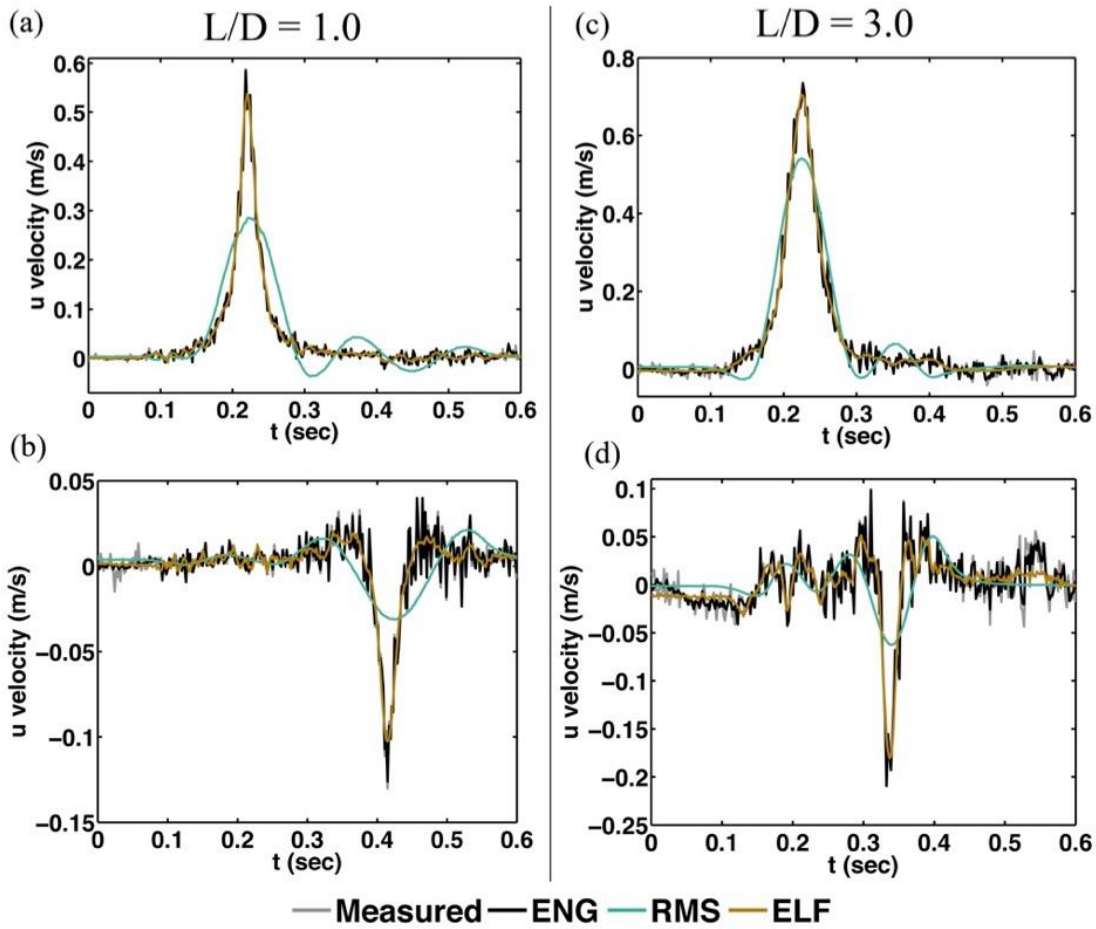
Figure 2-13: Velocity time series at two points in the flow field for the laminar case (a) and (b) and turbulent case (c) and (d), showing the smoothing effect of each POD thresholding method.

The POD mode information for the experimental vortex ring cases is summarized in Table 2-3. The RMS method was implemented using Equation 2.3 and the 1σ and 2σ values given in Section 2.3.3.1. For all methods, the laminar vortex ring case required more modes than the turbulent case. This could be the result of the higher uncertainty in the laminar case or the inability of the PIV spatiotemporal resolution to capture the small-scale turbulent structures. For both the laminar and turbulent cases, the ELF criterion does not keep sequential eigenmodes. For the turbulent case, the TKE method maintained almost all modes indicating that the data was not well enough converged for this to method to yield accurate results. Thus, the TKE method was excluded from post-processing calculations.

2.5.3.1 Data Smoothing and Filtering

Smoothing operators aim to filter out experimental measurement noise without removing or obscuring physical flow structures. Figure 2-13 shows the temporal variation of the velocity at two points in the flow field for each L/D_0 case.

For all point velocities in Figure 2-13, the energy criterion maintained about the same maximum velocity magnitude and the majority of the velocity fluctuations as compared to that of the measured velocity. In Figure 2-13a where flow was laminar, minimal fluctuations were expected, indicating that the energy criterion maintained too many modes by preserving these fluctuations likely caused by measurement noise. Conversely, the RMS method in all cases over-smoothed the data and altered both the shape and magnitude of the temporal velocity. In Figures 2-13a and 2-13b, for example, the RMS method yielded 51 and 76% reductions in the maximum velocity magnitude, respectively. Meanwhile, the ELF method provided 8 and 21% reductions in the maximum velocity vector. The ELF method qualitatively appears to be the only method to preserve the major characteristics of the velocity field, while eliminating much of the noisy fluctuations. However, the core vorticity, area, and circulation must be evaluated to quantitatively confirm this notion.

2.5.3.2 Evaluating Vorticity

The smoothing and filtering of a velocity field has implications on subsequent velocity gradient and vorticity calculations. Further, applying any finite differencing scheme to experimental data can often amplify the effect of noise in the velocity field. Figure 2-14 shows the

non-dimensionalized vorticity contours for each thresholding and spatial filtering method. Vorticity was non-dimensionalized by the piston diameter and maximum speed, $\omega D_0/U_{p,max}$. The results of the laminar and turbulent cases showed similar trends, thus only the turbulent fields are shown here.
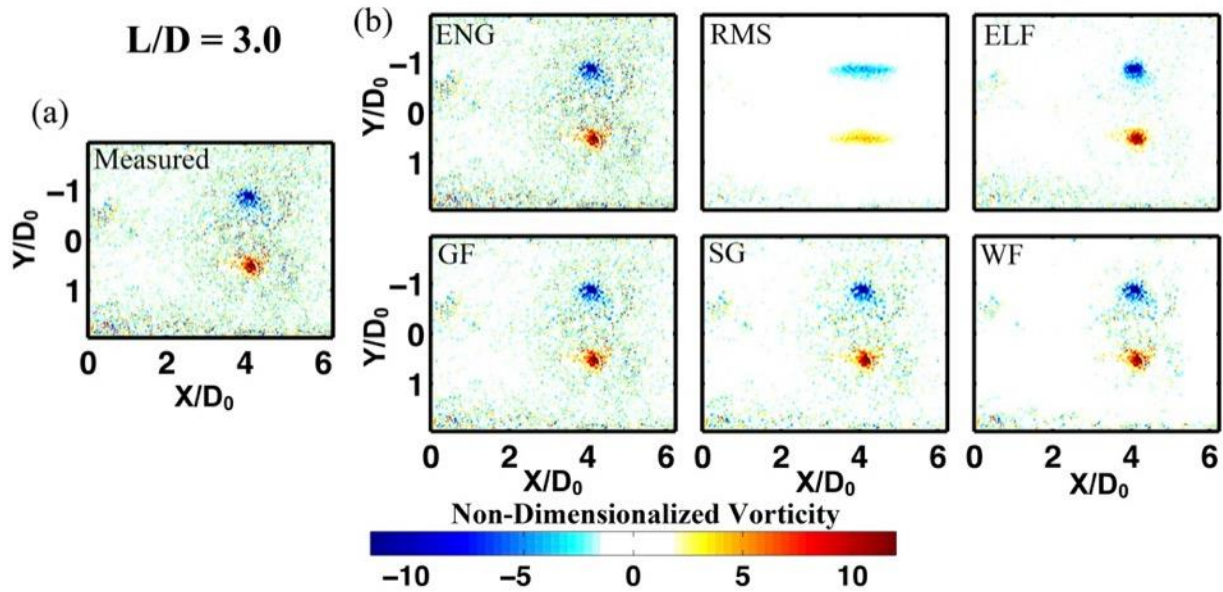
Figure 2-14: Non-dimensionalized vorticity contours computed with each POD thresholding criterion and spatial filtering method, for only the turbulent vortex ring case.

In Figure 2-14, both the measured and energy criterion vorticity fields had distinguishable core areas of vorticity, but maintained high noise in the surrounding field where the vorticity should be zero. For the turbulent case, the mean non-dimensionalized vorticity magnitudes excluding the cores for the original data and energy, RMS, and ELF criterion-filtered data were 1.49, 1.48, 0.55, and 0.84, respectively. For the Gaussian, Savitzky-Golay, and Wiener filters, the mean vorticity magnitudes excluding the cores were 1.22, 0.99, and 0.63, respectively. In accordance with previous studies, the Wiener filter outperformed the other filters [86]. The Wiener filter removed much of the vorticity noise in the surrounding region, but maintained noise between the vortex cores. The RMS method was the only method to alter the shape of the core vorticity, yielding an elliptic core area rather than circular. This distortion of the core vorticity had deleterious effects on the computed vortex core properties including area and circulation, as shown in the subsequent analysis. Meanwhile, the ELF method made the core vorticity area more distinguishable while preserving its shape for both cases.

2.5.3.3   Evaluating vortex ring core changes

For the temporal duration of the data used in this analysis, the vortex rings are fully formed and have not yet begun to break down. As such, the vortex rings were expected to maintain constant core vorticity, area, and circulation [82,88]. Therefore, any fluctuations or time-dependent trends observed in the data were expected to be contributed by experimental noise or error. Thus, each thresholding method can be evaluated for its ability to reduce fluctuations and time varying trends in these metrics.
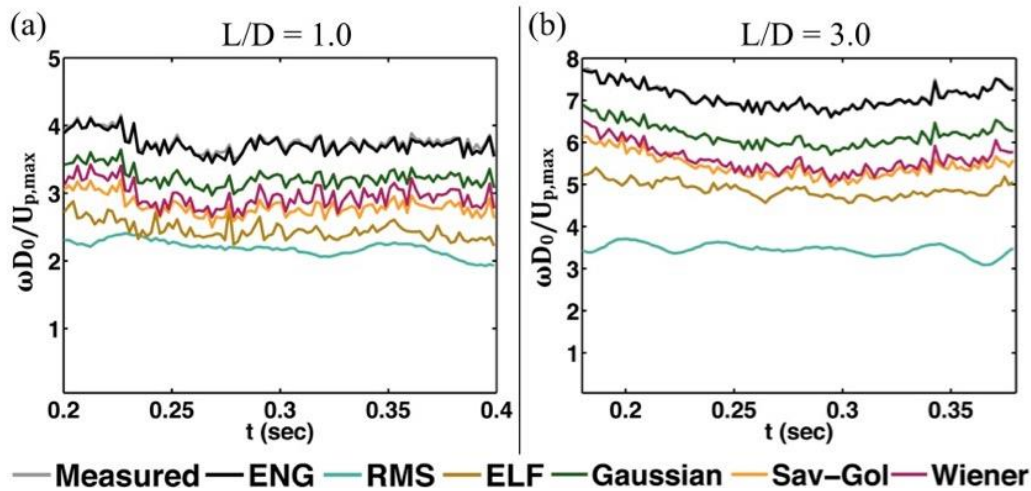
Figure 2-15: Non-dimensionalized core vorticity trend through time for each POD thresholding criterion and spatial filtering method for the (a) laminar case and (b) turbulent case.

Figure 2-15 shows the core vorticity trend through time for each POD thresholding method. The energy criterion again yielded nearly the same trend as the original data and did not reduce noise fluctuations. The RMS method yielded the largest reduction in fluctuations and the smoothest distribution. However, the ELF method maintained the same general trend as the original data did, while the RMS method yielded some ancillary time dependent trends. This is specifically noticeable in Figure 2-15b at time 0.37, where the raw data held a slightly increasing trend, but the RMS method showed a downward dip in magnitude. This demonstrates the over-smoothing performed by the RMS method generated intrinsic modes of oscillation that did not exist in the raw data. The RMS, ELF, and all spatial filtering methods substantially reduced the core vorticity magnitude. However, none of the spatial filtering methods attenuated the fluctuations in the distribution. Table 2-4 quantifies these reductions, providing the average values of all core metrics. Core area was non-dimensionalized by the piston diameter, A/D_{02}.

Table 2-4: Mean core metrics when vortex ring was fully formed for each POD thresholding method and each spatial filtering method. Listed uncertainties are the 1σ confidence interval RMS. Non-dimensionalized vorticity and area are reported.

	Core Metric	Vorticity	Area	Circulation – Γ (cm²/s)	
		$\omega D_0/U_{p,max}$	A/D_0^2	Line Integral of Velocity	Area Integral of Vorticity
	Measured	3.76 ± 0.14	0.030 ± 0.005	28.3 ± 3.1	30.6 ± 4.6
	ENG-95%	3.73 ± 0.15	0.029 ± 0.004	27.9 ± 3.0	30.5 ± 3.3
	RMS	2.19 ± 0.11	0.020 ± 0.005	6.2 ± 2.0	5.6 ± 1.3
$L/D_0 = 1.0$	ELF	2.46 ± 0.14	0.025 ± 0.004	24.3 ± 2.9	24.5 ± 2.0
	Gaussian Filter	3.23 ± 0.14	0.029 ± 0.004	27.1 ± 3.1	29.4 ± 3.3
	Savitzky-Golay Filter	2.96 ± 0.18	0.029 ± 0.004	27.5 ± 3.0	28.4 ± 4.3
	Wiener Filter	3.23 ± 0.14	0.026 ± 0.004	25.1 ± 3.1	28.1 ± 4.6
	Measured	7.10 ± 0.27	0.071 ± 0.011	65.1 ± 7.1	65.4 ± 11.3
	ENG-95%	7.09 ± 0.27	0.069 ± 0.011	64.0 ± 7.1	64.1 ± 11.5
	RMS	3.45 ± 0.13	0.051 ± 0.013	22.0 ± 5.6	17.6 ± 4.6
$L/D_0 = 3.0$	ELF	4.89 ± 0.19	0.059 ± 0.009	55.7 ± 5.9	51.0 ± 5.2
	Gaussian Filter	6.18 ± 0.27	0.068 ± 0.01	63.9 ± 7.2	63.6 ± 6.5
	Savitzky-Golay Filter	5.44 ± 0.28	0.065 ± 0.01	60.8 ± 6.6	60.0 ± 6.3
	Wiener Filter	5.61 ± 0.33	0.059 ± 0.01	56.9 ± 6.9	57.5 ± 6.6

Some smoothing-induced reductions to the core area and vorticity are expected since noise can corrupt the measurements and derivative calculations, causing an over-prediction of both core area and vorticity. The RMS and ELF methods yielded vorticity magnitude reductions of 54 and 40% for the laminar case, and 59 and 44% for the turbulent case, respectively. For both cases, the Gaussian, Savitzky-Golay, and Wiener filters reduced the vorticity by about 13, 23, and 21%, respectively. Meanwhile the energy criterion produced reductions of 16% for both the laminar and turbulent cases. In terms of the non-dimensionalized core area, the energy criterion and Gaussian filters maintained magnitudes all within a few percent of the measured data. The RMS, ELF, and Wiener filter methods yielded reductions of about 30, 17, and 17%, respectively, in both the laminar and turbulent vortex core areas. To determine the verity of the reported deductions, circulation, which depends on both core area and vorticity and has a known expected value, must be evaluated.

2.5.3.4 Evaluating Circulation

Expected circulation values based on empirical data for various L/D$_0$ values are known [81,82], allowing us to quantitatively examine the efficacy of each thresholding method.

Figure 2-16 illustrates the mean circulation values computed using both calculation methods. In all cases, the two circulation calculation methods showed good agreement with both values within the range of the uncertainties. This demonstrates that the noise in the flow field affected both calculations similarly and that POD smoothing altered the velocity, vorticity, and core metrics in a consistent manner. Using the velocity-line integral method for all further comparisons, the original, energy criterion, and Gaussian and Savitzky-Golay filters maintained similar circulation values and errors of approximately 25% from the expected circulation values, for both the laminar and turbulent cases. The RMS method demonstrated that the over-smoothing corrupted the core metrics and generated significant errors of over 55% in all circulation calculations. This was culminated by the propagation of error induced by the over-smoothing in the velocity and vorticity fields and core area detected by λ_{ci}. The Wiener filter produced circulation errors of 19 and 2%, for the laminar and turbulent cases respectively. The main drawback of the Wiener filter demonstrated here is that it retained high and noise-driven fluctuations in the metrics, which yields unpredictable error and demonstrates why POD smoothing generally performs better than spatial filtering. The ELF criterion produced circulation
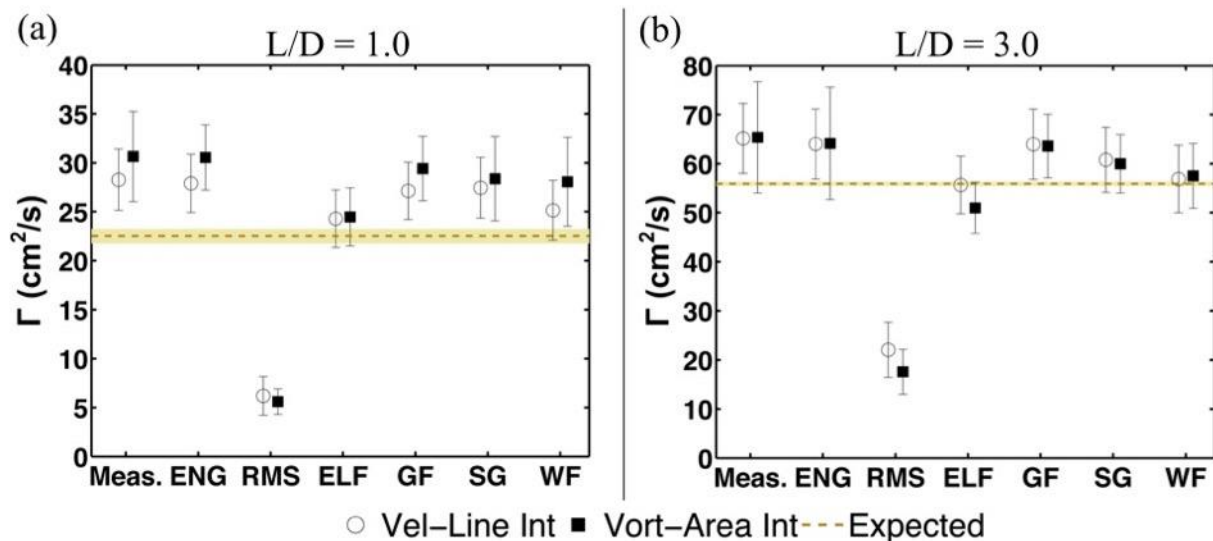
Figure 2-16: Circulation computed for each POD thresholding criterion and spatial filtering method for the (a) laminar case and (b) turbulent case. Circulation was computed two ways, using both the line integral of the velocity and the area integral of the vorticity.

50

estimates with errors of 8 and 4% for the laminar and turbulent cases, respectively. These low error values indicate that the reduction of core vorticity and area observed with the ELF method was primarily the result of the removal of noise from the flow field. This establishes the success of the ELF method at eliminating as much error as possible while maintaining the true characteristics of the flow field.

2.6   Conclusions

We present a new method (ELF) for POD mode truncation and experimental data denoising. The method enhanced the efficacy of POD at removing experimental noise by autonomously detecting error in individual eigenmodes and requiring no user inputs. It yielded a higher dynamic range of the velocity reconstruction, as compared to the energy and RMS criteria, and was able to keep modes with relevant flow structures whose energy was less than that of the noise. One major limitation of the ELF method revealed here was its erratic nature when the two-line fit procedure failed. In particular, this hinders the ability of ELF method to be used as a means to compute the exact number of modes that exist in an analytical flow field. However, the ELF method performed exceptionally as a smoothing operator. Using experimental vortex ring data, we demonstrated that the successful reduction of noise in a flow field produced using the ELF criterion increased the accuracy of subsequent calculations and analysis. In general, the ELF thresholding criterion for POD provides superior, completely autonomous smoothing capabilities, and is easy to implement and applicable to any experimental fluid dynamics study.

2.7   Acknowledgements

CHAPTER 3. DENSITY- AND VISCOSITY-MATCHED NEWTONIAN AND NON-NEWTONIAN BLOOD-ANALOG SOLUTIONS WITH PDMS REFRACTIVE INDEX

3.1   Abstract

Optical imaging is commonly used to investigate biological flows and cardiovascular disease using compliant silicone polydimethysiloxane (PDMS) Sylgard 184 geometries. However, selecting the working fluid with blood density and viscosity, and PDMS index of refraction (RI) for such experiments is challenging. Currently, water-glycerol is commonly used and sodium iodide (NaI) often added to increase the index of refraction without changing fluid viscosity. But the resulting fluid density is well above blood. Moreover, NaI is expensive, has safety and material discoloration concerns, and has been reported to affect non-Newtonian fluid behavior. Here, we present a new blood analog alternative based on urea. Urea is approximately five to fifteen times less expensive than NaI, safe and easy to handle, optically clear, and causes no discoloration. Water-glycerol-urea solutions, unlike those with NaI, simultaneously matched the density and viscosity of blood and RI of PDMS. Water-xylitol and water-xylitol-urea solutions are also possible blood analog solutions. Xanthan gum (XG)-water-glycerol non-Newtonian solutions maintained similar viscoelastic properties throughout the range of weight percent (about 15-25%) of urea and NaI used here. The results showed that the XG weight percent affected viscoelastic properties more than the weight percent of urea or NaI tested in this study. Overall, we demonstrate urea is useful for PDMS blood analog experiments and should also be considered as an inexpensive additive, and an alternative to NaI.

3.2 Introduction

In vitro flow experiments are used to evaluate a range of vascular diseases. Optical *in vitro* imaging measurement techniques, such as particle image velocimetry (PIV), are used because they provide well-controlled flow fields with high spatiotemporal resolution. For such experiments, the test geometries are often made of silicone polydimethysiloxane (PDMS) Sylgard 184 because the versatility in the curing process allows for specific shapes and compliances to be represented [89]. Although 3D printing and plastic materials are also used, they are limited to rigid test sections. Detailed evaluation and review of *in vitro* experimental techniques, including test section manufacturing, are presented by Wright et al. (2017) [89] and Yazdi et al. (2018) [90].

For optical experiments using PDMS models, selecting the proper working fluid is critical, but difficult even for Newtonian fluids [90]. Imaging requires the fluid to be optically clear and have the same index of refraction (RI) as the material of the geometry section. For complex geometries, even small differences in RI can result in significant optical distortion [40]. The working fluid must also simultaneously match the fluid properties of blood (ρ = 1060 kg/m$_3$, μ = 2.9-4.37 mPa-s) [90,91]. While dynamic scaling may be used in cases where the working fluid does not match that of blood, this is not always possible and can add complexity to the experiment and the calculation of properly scaled spatiotemporal gradients. A 60/40 (by volume) water-glycerol mixture is one of the most widely used blood analogue solutions for use with PDMS. However, a 60/40 water-glycerol mixture yields an index of refraction of approximately 1.39, well below that of PDMS at 1.414 [92]. A water-glycerol mixture with the same RI of PDMS has a viscosity about 2-3 times higher than blood. To increase the RI of a 60/40 water glycerol solution, sodium iodide (NaI) is often added because it increases index but does not change the kinematic viscosity of the fluid [92–94]. However, NaI is expensive, corrosive to equipment, and can cause discoloration of material upon direct contact [92,94,95]. NaCl has also been used to increase the index of refraction of water-glycerol, but this increases the solution viscosity above that of blood [96]. Najjari et al. (2016) tested sodium thiocyanate (NaSCN) and potassium thiocyanate (KSCN) as additives to water-glycerol, but safety of both chemicals is a concern, particularly when heated. Other proposed Newtonian blood analog solutions include a mixture of ethanol and diethylphthalate [97] and a mixture of isopropyl alcohol and glycerol [98]. However, alcohols have densities lower than water (and thus blood) and are flammable, presenting safety issues for use with high-power lasers.

Among Newtonian blood analog solutions, fluid density is rarely considered. For example, the density of water-glycerol-NaI solutions matching the RI of Sylgard 184 is typically about 1250 kg/m$_3$ [89,90,94], substantially higher than the density of blood. NaI is often added because of the convenience of not changing the viscosity, but its high density increases fluid density significantly, a concern for PIV studies where tracer particles must be neutrally buoyant. While water-glycerol-NaI solutions can simultaneously match the RI of PDMS and viscosity of blood, it is not able to simultaneously match these two parameters and the density of blood.

The effect of each additive on non-Newtonian fluids must also be considered. Most often a very small amount (<0.06% by weight) of xanthan gum (XG) is added to the base solution mixture, to yield a non-Newtonian fluid. Long et al. (2005) reported that NaI does not affect viscoelastic properties of an XG-water-glycerol solution. However, Najjari et al. (2016) reported NaI significantly reduced the shear-thinning properties of such solutions [94]. Deplano et al. (2014) also reported that the rheology of XG solutions is sensitive to the addition of salts [99].

In this work, we present a novel blood analog solution—a mixture of water-glycerol and urea—which is able to simultaneously match the index of refraction of PDMS, and the density and viscosity of blood. Like NaI, urea increases the index of refraction of water and water-glycerol linearly [100]. Urea is less expensive (about 5-15x) and safer than NaI. By comparison, urea causes small increases in the kinematic viscosity and density of water-glycerol solutions, while NaI causes minimal change in kinematic viscosity and a large increase in density. We tested different concentrations of water-glycerol-urea solutions and compared these solutions to mixtures of water-glycerol-NaI. To test the effect of urea on XG solutions, we added various concentrations of XG to water-glycerol-urea and compared the viscoelastic properties to XG-water-glycerol-NaI solutions. Xylitol was also tested as a substitute for glycerol. Although in this work, we limit evaluation to blood analog solutions for use with PDMS, urea should be considered as a cost-effective and safe additive for index matching in any PIV experiment.

3.3   Materials and Methods

3.3.1   Working Fluid Preparation

Fluids were prepared using ultrapure water (Thermo Scientific Barnstead NANOpure Water Purification System) and mixed with a magnetic stir bar at room temperature. Additives

included urea (Fisher Chemical), xylitol (99%, Alfa Aesar), sodium iodide (Technical Grade 9080, IodiTech), sodium chloride (Fisher Chemical), glycerol (99%, PTI Process Chemicals), and xanthan gum (Hodgson Mill). All chemicals were used as received from the supplier, with no additional purification.

To obtain baseline information, two-component Newtonian mixtures, where each additive was added incrementally to the ultrapure water, were first tested. Solutions were magnetically stirred for approximately 30 minutes before testing. The temperature, index of refraction, density, and dynamic viscosity were recorded during each iteration of Newtonian testing, as described in Section 3.3.2.

Three-component Newtonian mixtures were then tested using ultrapure water, glycerol, and NaI or urea. Three ratios of water-glycerol were used to represent low, medium (average), and high values of reported blood viscosity. The three water-glycerol base mixtures were allowed to stir for 24 hours and subsequently split into two 200 mL sub-volumes, resulting in six total solutions. Incremental amounts of NaI or urea were added to the water-glycerol solutions until the refractive index of PDMS Sylgard 184 was reached. Each incremental addition was allowed to stir for about 30 minutes before testing.

Newtonian testing was done using the six final PDMS-index matched water-glycerol-urea and water-glycerol-NaI solutions. Each of the six solutions were split into four 50 mL sub-volumes, resulting in 24 total samples. Xanthan gum was added at 0.02, 0.04 and 0.06 wt%. All samples were stirred constantly for 3-4 days to ensure well-mixed solutions. Temperature, index of refraction, density, and oscillatory elasticity and viscosity were obtained for all non-Newtonian fluids.

3.3.2 Fluid Property Measurement

Refractive indices were measured at 589 nm with a handheld, digital Abbe Refractometer (Model PA202) with range of 1.3330-1.5000 nD and +/-0.0001 precision. Densities were calculated as the average of three mass/volume measurements. Volumes were measured using a 1000 µL pipette for highest accuracy. Rheological properties were measured with a Discovery HR-2 Hybrid Rheometer (TA Instruments) using a cone (1°:00':11" and 40-mm diameter) geometry. These tests were performed under controlled temperature conditions (23.6$_o$C ±0.02$_o$C) correlating with the initial fluids at room temperature.

3.3.2.1 Newtonian

The steady shear (sweep mode) experiments were conducted using the cone geometry with a gap of 66 µm and shear rate ranging from 1 to 500 s_{-1}. In sweep mode, a steady and increasing shear rate is applied to the fluid to evaluate variations of viscosity with shear rate. Newtonian fluids plateaued to a constant viscosity at higher shear rates, and these values were used to obtain the dynamic viscosity, μ_∞ (Pa-s), of the fluid. For the chosen shear rate range, the kinematic viscosity remained constant throughout.

3.3.2.2 Non-Newtonian

Non-Newtonian fluids were tested using the cone geometry with a 66 µm gap and an oscillatory shear stress of 2 Hz to obtain the storage modulus, *G'* (Pa), and loss modulus, *G"* (Pa). These parameters were used to compute the elasticity and viscosity of the fluids respectively. Oscillatory elasticity, ζ (m_2/s), was calculated according to the Equation (3.1):

$$\zeta = G'/\omega\rho \qquad \text{(Equation 3.1)}$$

where ω is angular frequency (ω = 12.566 rad/s) and ρ is the density of the fluid (kg/m_3). Oscillatory viscosity, ν (m_2/s), was calculated using Equation (3.2):

$$\nu = G''/\omega\rho \qquad \text{(Equation 3.2)}$$

Triplicate oscillatory shear rate runs were performed, and the G' and G'' values averaged. The averaged values were used to compute the oscillatory viscosity and elasticity. The results are presented with uncertainty bars showing ±1 standard deviation of the three run average.

3.4 Results and Discussion

3.4.1 Two-component Newtonian Fluids

Properties of the two-component Newtonian fluids were characterized at room temperature to identify feasible alternatives to NaI for the purpose of increasing the index of refraction of blood analogs. Alternatives to water-glycerol solutions were also investigated. Urea and xylitol were identified as low cost, low density, RI increasing additives. Both urea and xylitol are safer and about 5x less-expensive per unit mass than NaI. Urea solutions are also more stable than NaI, improving the safety and usability of long-term stored solutions. Table 3-1 summarizes the properties of each additive used in this study.

Table 3-1: Properties of chemical additives used in two-component solutions.

Material	Chemical Formula	Density (kg/m³)	Solubility (g/L)	Cost per 500g (USD)†	Safety‡
Urea	CH_4N_2O	1320	545 (25°C)	$8.95 - 58.90	Health: 1 Flammability: 0 Instability: 0
Sodium Iodide	NaI	3670	1840 (25°C)	$141.80 - 264.00	Health: 2 Flammability: 0 Instability: 1
Xylitol	$C_5H_{12}O_5$	1520	1700 (20°C)	$68.30 - 84.00	Health: 1 Flammability: 0 Instability: 1
Sodium Chloride	NaCl	2160	100 (20°C)	$7.35 - 39.50	Health: 1 Flammability: 0 Instability: 1
Glycerol	$C_3H_8O_3$	1261	Miscible	$10.29 - 92.86	Health: 1 Flammability: 1 Instability: 1

† Prices ranges based on Fischer Scientific Alfa Aesar 99+%, Sigma-Aldrich ACS reagent grade, and Carolina Biological laboratory grade. Xylitol is not available from Carolina Biological and based on other two prices only.

‡ As defined by NFPA 704 on chemical SDS; 0 – least hazardous and 4 – most hazardous

The index of refraction, density and viscosity of each aqueous solutions of each additive are shown in Figure 3-1a, 3-1b, and 3-1c, respectively. Figure 3-1a shows that by weight percent (wt%), both xylitol and urea were about as effective as NaI at increasing the index of refraction of water. NaCl was most effective, but the solution quickly lost clarity and reached saturation at an
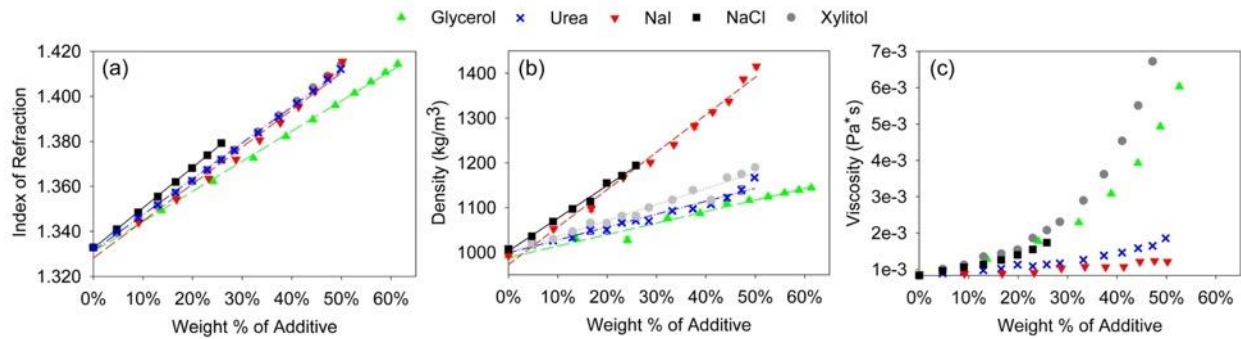
Figure 3-1: Effect of aqueous solutions of glycerol, xylitol, urea, sodium chloride, and sodium iodide on the index of refraction (a), density (b), and viscosity (c) of water.

index of refraction of 1.3793. Figure 3-1b shows that the increase in fluid density as a function of additive weight percent was about five times less for xylitol and urea than NaI. Specifically, an aqueous 50.21 wt% NaI solution had a density of 1416 kg/m3, while at similar weight percent, aqueous urea (49.83 wt%) had a density of 1167 kg/m3 and aqueous xylitol (49.94 wt%) had a density of 1190 kg/m3. Figure 3-1c indicates that xylitol caused a larger increase in viscosity of the fluid than both urea and NaI. A 49.94 wt% solution of xylitol had a viscosity of 8.493E-3 Pa-s, while similar weight percent solutions of urea (49.83 wt%) and NaI (50.21 wt%) had viscosities of 1.857E-3 Pa-s and 1.213E-3 Pa-s, respectively.

These results demonstrate that urea can be used as a low-density additive for changing the refractive index of working fluids. Among additives tested, NaI and urea had the smallest and similar effect on dynamic viscosity. These results agreed with the general consensus that NaI has negligible effect on kinematic viscosity. For blood analogs matching refractive indices in the range of 1.38 to 1.40, a mixture of water-xylitol should be considered. For example, you can achieve a water-xylitol solution where the RI = 1.3915, ρ = 1139 kg/m3, and μ = 3.619E-3 Pa-s.

3.4.2   Three-component Newtonian Fluids

Urea and NaI were used to make three-component Newtonian solutions of water-glycerol-additive to develop blood analogs. Xylitol was not included here because the resulting solution when mixed with glycerol has a viscosity 2-3 times that of blood. Figure 3-2 shows the RI (3-2a), density (3-2b) and viscosity (3-2c) of these fluids. Water-glycerol solutions were prepared to represent low (3.0E-3 Pa-s), medium (3.8E-3 Pa-s), and high (4.6E-3 Pa-s) values of reported
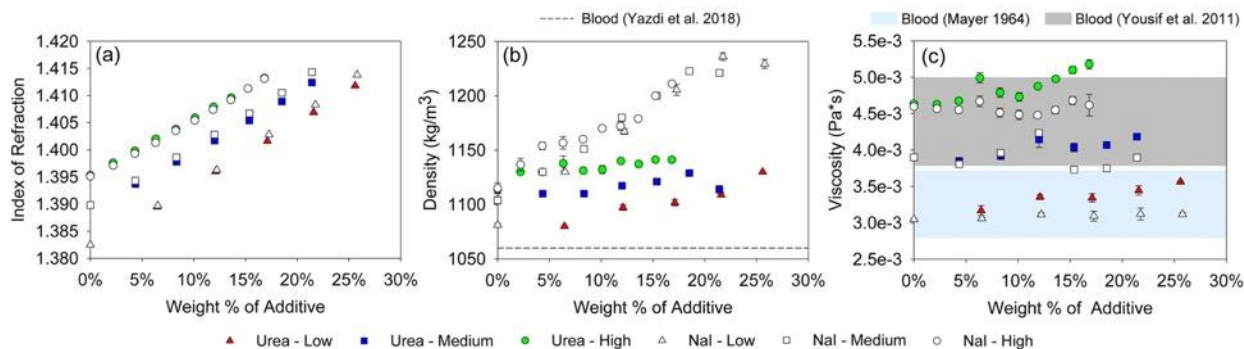
Figure 3-2: Index of refraction (a), density (b), and viscosity (c) variations of three-component Newtonian solutions when urea and NaI were added to water-glycerol. Three starting ratios of water-glycerol were tested (low, medium, high) to span the range of reported human blood viscosities.

blood viscosity [91,92]. The corresponding water-glycerol volume ratios for the low, medium, and high viscosity solutions were 67/33, 62/38 and 58/42, respectively.

As shown in Figure 3-2a, the RI of both the urea and NaI solutions increased at a similar rate as a function of weight percent. The change of index as a function of weight percent of urea was independent of the starting ratio of water-glycerol in this range. Thus, when using urea, the desired fluid properties and RI can be planned and adjusted based on weight percent of glycerol and urea. Considering the solution density, as observed in Figure 3-2b, the addition of urea caused a density increase of about 1.3 kg/m3 per wt%, while NaI caused a density increase of approximately 6.0 kg/m3 per wt%, a nearly five-fold difference. Thus, when adding NaI, the increase in density is substantial and should be considered. In terms of viscosity, urea increased the fluid viscosity of the low, medium, and high water-glycerol solutions by 17, 7, and 12%, respectively. Thus, when adding urea to water-glycerol solutions, a small increase of viscosity is expected, but the fluid viscosity can still remain within the range of blood viscosity. Table 3-2 summarizes the final properties of all three-component solutions. As previously indicated in Table 3-1, the urea solutions are approximately 5 times less expensive than the NaI solutions. Further, urea solutions are safe and easy to make and use. A water-glycerol-urea solution was left in an experimental flow loop for approximately 6 weeks and in a Pyrex container for approximately four months. No discoloration of the fluid or any flow loop components was observed.

Although xylitol increased viscosity too much to be used in a water-glycerol-xylitol solution, it can instead replace glycerol in three-component Newtonian solutions. Because of the oily nature

of glycerol, it can be difficult to handle and leaves slippery residue when spilled. Conversely, xylitol is easy to handle, a common and safe product, and can be bought in a technical grade inexpensively. Table 3-3 provides fluid composition and properties for three water-xylitol-urea solutions. Table 3-3 confirms that water-xylitol-urea solutions can be used as a blood analog with PDMS.

Optical experiments using glass or acrylic models require a higher fluid RI of between 1.47-1.49. To test for such experiments, urea was added to a 57/43 by volume solution of water-glycerol. The highest achievable index of refraction before saturation of urea was 1.4428. Thus, water-glycerol-urea alone cannot be used for high index of refraction optical experiments. However, urea can be combined with NaI to achieve high RI fluids at a cheaper cost, through the fluid and stability properties of such solutions should be explored in future work.

Table 3-2: Final properties of three-component Newtonian fluids.

Starting Viscosity	Material	Wt% Water	Wt% Glycerol	Wt% Additive	Refractive Index	Viscosity (Pa-s)	Density* (kg/m^3)
	Blood; PDMS	--	--	--	1.4118	2.81E-3– 3.72E-3[1]	1060
						3.8E-3– 5.0E-3[2]	
LOW	Urea	45.64	28.77	25.58	1.4118	3.564E-3	1130
	NaI	45.51	28.70	25.79	1.4138	3.117E-3	1229
MEDIUM	Urea	44.07	34.52	21.41	1.4124	4.184E-3	1114
	NaI	44.07	34.52	21.41	1.4143	3.898E-3	1221
HIGH	Urea	43.21	39.96	16.83	1.4132	5.178E-3	1141
	NaI	43.21	39.96	16.82	1.4131	4.616E-3	1211

[1] Mayer GA (1964) Blood Viscosity in Healthy Subjects and Patients With Coronary Heart Disease. Can Med Assoc J 91:951–4.

[2] Yousif MY, Holdsworth DW, Poepping TL (2011) A blood-mimicking fluid for particle image velocimetry with silicone vascular models. Exp Fluids 50:769–774.

*Density uncertainty was 0.61% or less for all reported values.

Table 3-3: Properties of water-xylitol-urea solutions.

Wt% Water	Wt% Xylitol	Wt% Urea	Temperature (oC)	Refractive Index	Viscosity (Pa-s) (23.6 oC)	Density (kg/m3)
50.6	20.0	29.4	23.6	1.4118	2.957E-3	1154
50.7	25.3	24.0	22.4	1.4120	3.547E-3	1154
50.9	30.3	18.8	24.2	1.4118	4.033E-3	1152

3.4.3   Non-Newtonian Fluids

For flow in small vessels (diameter $< 0.5 - 0.6$ mm), in addition to RI, density and viscosity, the Non-Newtonian behavior of blood must also be considered [101]. Previous studies have reported that non-Newtonian solutions using xanthan gum lose shear-thinning properties with the addition of salts, such as NaI [94,99]. Therefore, the effect of urea on non-Newtonian XG solutions was tested. Xanthan gum was added at 0.02, 0.04 and 0.06 wt% to the final three-component Newtonian solutions to introduce non-Newtonian properties. Fluid testing was conducted for a
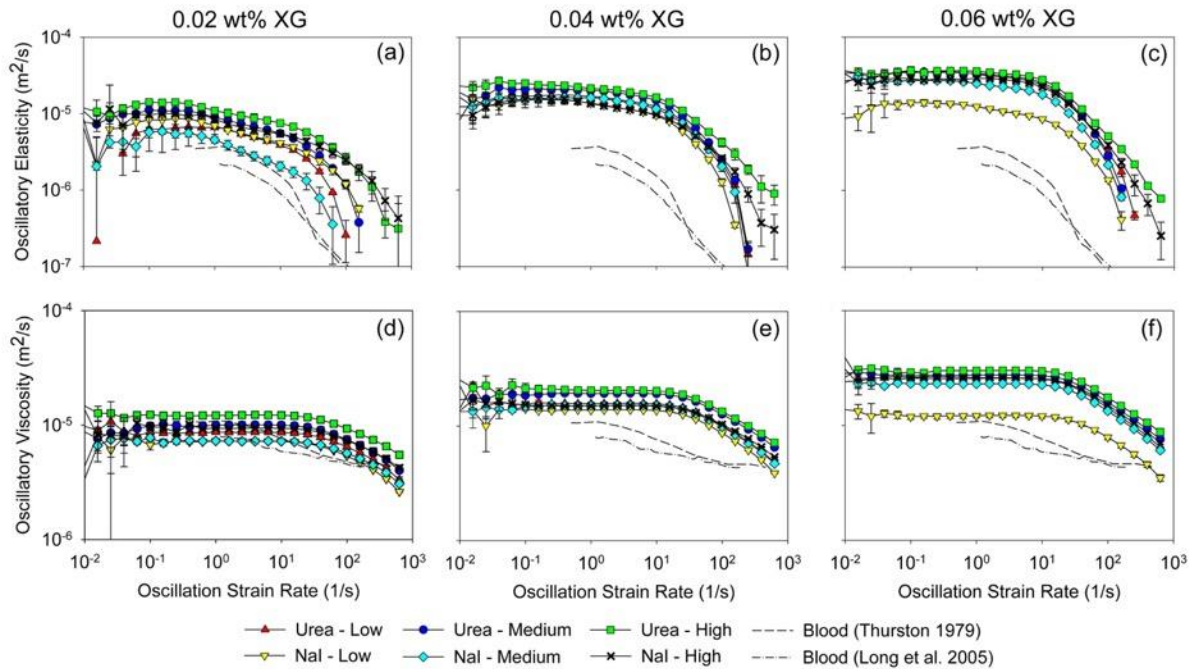
Figure 3-3: Oscillatory elasticity (a-c) and viscosity (d-f) with 0.02 (a, d), 0.04 (b, e), and 0.06 (c, f) wt% xanthan gum added to the low, medium, and high water-glycerol ratios with urea and NaI added. Blood viscosity and elasticities reported in Thurston (1979) and Long et al. (2005) were extracted using WebPlotDigitizer.

strain percent range of 5E-3 to 5000, corresponding to an oscillation strain rate of approximately 8E-4 to 650. The resulting oscillatory viscosity (m_2/s) and oscillatory elasticity (m_2/s) as a function of oscillatory strain rate (s_{-1}) are shown in Figure 3-3 in comparison to blood [93,102]. Increased uncertainty in oscillatory elasticity at high oscillatory strain rates was observed, possibly due to the large gap size used, however, this increased uncertainty does not change the general observations and conclusions presented here.

Overall, as observed in Figure 3-3, urea and NaI maintained similar viscoelastic properties in XG-water-glycerol solutions, confirming that urea can also be used for non-Newtonian solutions. At constant weight percent XG, the weight percent of urea or NaI in this range (about 15-25 wt%) had small effect on the shear thinning non-Newtonian behavior. It is important to note, because
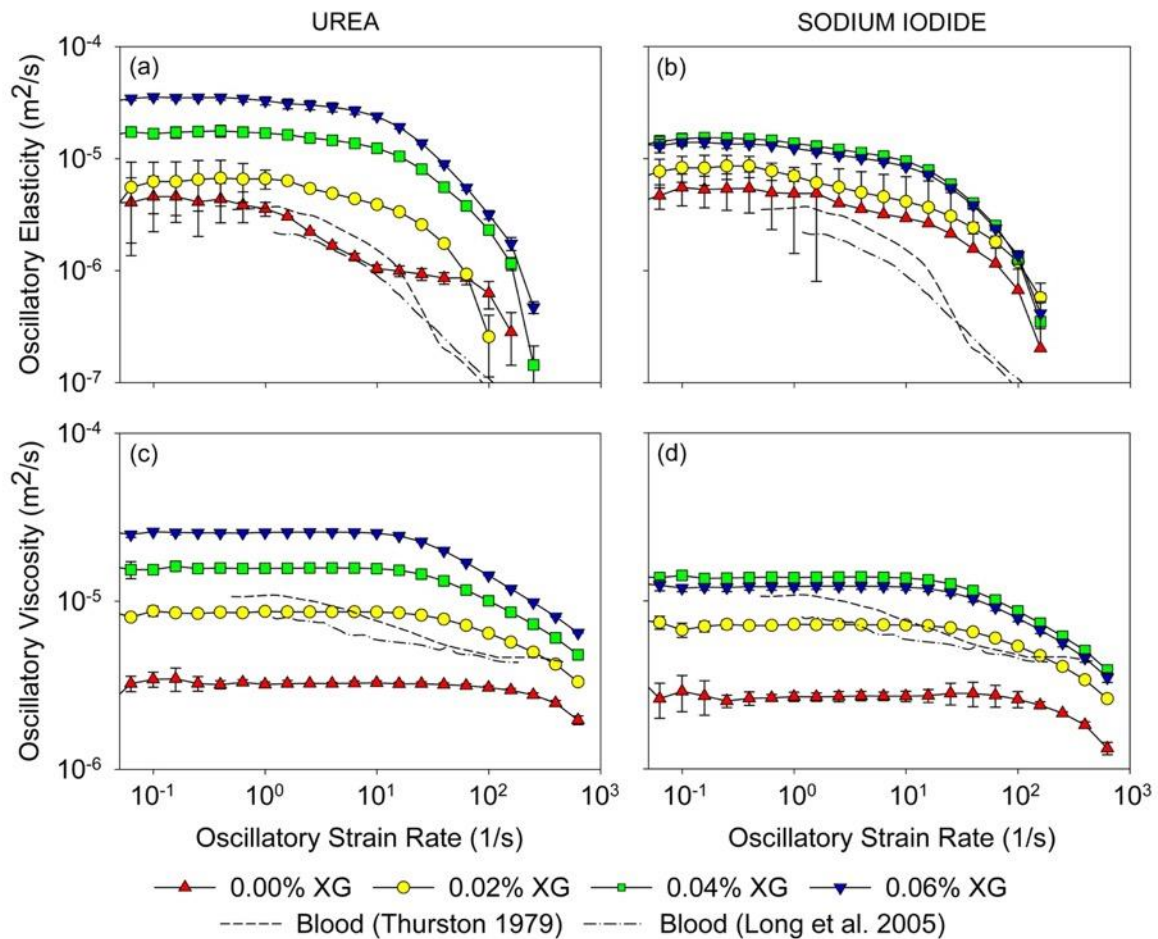
Figure 3-4: Oscillatory elasticity (a-b) and viscosity (c-d) at various weight percent xanthan gum added to the low water-glycerol ratio solution with urea (a and c) and NaI (b and d) added. In (a), high uncertainty in the 0 wt% XG yielded an abnormal elasticity trend, but was still included for completeness.

62

the index of refraction of PDMS is of primary interest in this work, the range of additive used here was limited compared to other studies that investigate fluids of high refractive index (1.47-1.49). Based on Figure 3-3, adding 0.02 wt% XG to the studied solutions resulted in the closest match to the non-Newtonian properties of blood.

Figure 3-4 shows the low starting viscosity solutions with varying weight percent XG (0-0.06 wt%) added. Because the weight percent XG added was so low, the weight percent of water, glycerol, and additive were effectively unchanged. The weight percent of XG from 0.02-0.06 wt% had a significant effect on the magnitude of the oscillatory elasticity and viscosity of the fluid. Also, at higher weight percent XG, the slope of the shear-thinning property increased slightly. It is important to note, in our method the XG was added last, allowing for the weight percent of XG added to be precisely controlled for each solution. However, it is typical for the XG to be added directly to glycerol prior to mixing all other components together, to reduce mixing time. The latter method changes the weight percent of XG in the final solution, often significantly, because of the small weight percent of XG used. For example, as reported in Najjari et al. (2016), the wt% of XG was 0.06 with no NaI added but decreased to 0.044 and 0.028 wt% XG for 26.87 and 55.46 wt% NaI added, respectively. Further, the change in NaI shear-thinning observed in that work closely resembles the change observed in Figure 3-4 when only the XG weight percent is reduced, though it cannot be specifically determined from these observations to what degree the reported change in shear-thinning viscoelastic properties in that work was caused by the addition of NaI versus the reduction in XG weight percent. Therefore, future studies are needed to explore this and investigate the viscoelastic properties of higher wt% NaI, urea, and other additives with a fixed weight percent of XG across all solutions.

3.5 Conclusions

Two-component and three-component Newtonian and non-Newtonian blood analog solutions for use with PDMS and optical imaging were studied here. In this work, we characterized urea and xylitol as additives to water and water-glycerol blood analog mixtures as low-density alternatives to NaI. The addition of urea to Newtonian water-glycerol solutions resulted in a blood analog that simultaneously matched blood density, viscosity, and the RI of PDMS. In contrast, NaI increased fluid density by about 6.0 kg/m_3 per weight percent added, making water-glycerol-NaI solutions with densities well above that of blood. Urea is relatively inexpensive, safe, and easy to

work with. Water-xylitol and water-xylitol-urea were also found to be adjustable for a wide range of refractive indices while meeting blood analog criteria, particularly low blood viscosities. For non-Newtonian testing using XG-water-glycerol solutions, urea and NaI maintained similar shear-thinning properties. These results also showed that the viscoelastic properties of the non-Newtonian fluids were primarily affected by weight percent XG, while weight percent additive in the studied range (about 15-25%) had a smaller effect. These results demonstrate that urea should be considered as an affordable and simple way to adjust the RI of working fluids, while only slightly altering the fluid density and viscosity, for PIV experiments.

3.6 Acknowledgements

CHAPTER 4. PULSATILE PIPE FLOW TRANSITION: FLOW WAVEFORM EFFECTS

4.1 Abstract

Although transition is known to exist in various hemodynamic environments, the mechanisms that govern this flow regime and their subsequent effects on biological parameters are not well understood. Previous studies have investigated transition in pulsatile pipe flow using non-physiological sinusoidal waveforms at various Womersley numbers, but have produced conflicting results and multiple input waveform shapes have yet to be explored. In this work, we investigate the effect of the input pulsatile waveform shape on the mechanisms that drive the onset and development of transition using particle image velocimetry, three pulsatile waveforms, and six mean Reynolds numbers. The turbulent kinetic energy budget including dissipation rate, production, and pressure diffusion was computed. The results show that the waveform with a longer deceleration phase duration induced the earliest onset of transition while the waveform a longer acceleration period and thus smaller velocity gradients delayed the onset of transition. In accord with the findings of prior studies, for all test cases turbulence was observed to be produced at the wall and either dissipated or redistributed into the core flow by pressure waves, depending on the mean Reynolds number. Turbulent production increased with increasing temporal velocity gradients until an asymptotic limit was reached. The turbulence dissipation rate was shown to be independent of mean Reynolds number, but a relationship between the temporal gradients of the input waveform and the rate of turbulence dissipation was found. In general, these results demonstrated that the input pulsatile waveform directly affected the onset and development of transition.

4.2 Introduction

Transition to turbulence in pulsatile pipe flow is of interest in the biomedical field. Transitional flow has been observed in the heart, aorta, downstream of narrowed (stenotic) vessels [34,35,103], and in aneurysms [9,19,36]. Transitional flow alters relevant hydro- and hemo-dynamic parameters, including wall shear stress and pressure, which affect the biomechanics of vessels and can lead to the growth or development of vascular disease. Further, the pulsatile waveform varies based on the region of the vasculature of interest, yet the effect of the shape of the pulsatile waveform on transition has not been studied. In general, there has been a lack of physiologically-relevant transitional pulsatile flow studies and the mechanisms that lead to the onset and development of transition in this domain remain unclear.

In transitional flow studies, pulsatile flow is typically defined as an oscillating flow component superimposed on a constant mean flow. The turbulence production mechanisms in fully turbulent pulsatile pipe flow have been studied extensively and yielded consistent conclusions. Turbulence is produced in the near wall region and then diffuses to the core region [104–106]. Scotti and Piomelli [105] found turbulence production occurred primarily during the end of the acceleration phase and was centered around l_s^+, the non-dimensional parameter of the Stokes layer thickness, l_s. The two terms are defined as:

$$l_s = \sqrt{2\nu/\omega} \qquad\qquad \text{(Equation 4.1)}$$

$$l_s^+ = l_s \frac{u_\tau}{\nu} \qquad\qquad \text{(Equation 4.2)}$$

where ν is kinematic viscosity (m2/s), ω is the pulsatile frequency (1/s), and u_τ is the friction velocity (m/s). He and Jackson [104] observed the shear waves produced at the walls were attenuated and confined to the viscous sub-layer. This agrees with the findings of Eckmann and Grotberg [107] who found turbulence was confined to the walls while the core flow remained laminar. Alternatively, Scotti and Piomelli [105] observed at low pulsatile frequencies turbulence produced at the wall had enough time to dissipate to the core flow during the deceleration phase.

Intermittency and turbulent 'puffs' are a primary characteristic of transitional flow. These puffs form at the location of instabilities in the flow and propagate downstream [108]. Stettler and Hussain [109] observed the intermittent turbulent 'puffs' in pulsatile flow were phase-locked. The phase-locked regime was also observed by Trip et al. [32] Beyond this, contradiction exists regarding both the underlying mechanisms and critical Reynolds number in pulsatile transition

pipe flow studies [32,110]. Much of the discord seems to be caused by different transitional regimes found at different frequency parameter values (Womersley number, α). The critical Reynolds number and intermittent flow structures were found to be affected primarily by the mean velocity (Reynolds number), frequency parameter, and the ratio of the mean to the pulsatile velocity amplitude [32,108,109]. Different combinations of the three factors, particularly low Womersley numbers and high pulsatility amplitudes, were found to suppress the development of transitional flow structures [108]. Peacock et al. [110] determined a power-law relationship of the frequency parameter, α, and Strouhal number, which correlated to the critical Reynolds number. This implies that critical Reynolds number always increases with increasing α, which was also shown by Falsetti et al. [111] However, Stettler and Hussain [109] found the critical Reynolds number to decrease (as compared to steady flow) for Womersley numbers less than 3, but to increase for Womersley numbers between 4 and 10. Trip et al. [32] found for α values between 10-25, transition occurred at a similar critical Reynolds number as steady flow, and was only dependent on the mean Reynolds number. The results in Trip et al.[32] demonstrated that as the α decreased, transition occurred more gradually across a broader range of Reynolds numbers. Several studies have shown turbulence increases during the deceleration phase of the cycle and re-laminarizes during the acceleration phase [32,107,109]. This suggests a phase shift exists between the turbulence intensity and mean velocity. Trip et al. [32] showed this phase shift existing for the Womersley values between 10-25. However, at a Womersley value of 4.85, Iguchi et al. [106] found no phase shift.

The discrepancies among prior pulsatile pipe flow transition studies indicate that all factors which play a role in transition have not been identified or studied. The known intermittency-affecting factors referenced here suggest that transition is, at least in part, influenced by the input pulsatile waveform velocity gradients. This could explain why different Womersley numbers produce different transitional mechanisms and critical Reynolds numbers. However, this relationship between input pulsatile waveform velocity gradients and factors such as turbulence production and dissipation which effect transition has not been studied in detail, despite the insight it may reveal into the prior inconsistencies. Further, studies have almost universally employed a sinusoidal oscillating flow component with a non-zero mean that results in a waveform that never tends to zero. Not only is this not physiological, it will only amplify or attenuate the waveform velocity gradients, but not change their shape.

In the present work, we compare three distinct input waveform shapes tested across a range of mean Reynolds numbers covering the laminar-turbulent transition zone and identify the differences in the onset and development of transition by the different waveforms. Subsequently, we analyze the turbulent kinetic energy (TKE) budget, primarily production, dissipation, and pressure diffusion, in order to explain the underlying mechanisms causing these differences associated with different pulsatile waveform shapes. We specifically focus on detailing the relationships between the TKE budget components and the velocity and acceleration of the input pulsatile wavelet. We isolated the influence of the waveform gradients by maintaining a constant Womersley number of 2.4, a physiologically typical value. Additionally, we limited the input waveforms to all be of clinical significance, thus all waveform shapes and mean Reynolds numbers tended to zero. A planar particle image velocimetry (PIV) experiment was conducted to obtain velocity fields for all test cases. It is important to note, due to some shortcomings of the experimental methods, this work does not allow for global analysis of the critical Reynolds number of transition, only comparisons between test cases of the driving mechanisms.

4.3   Experimental Techniques

4.3.1   Flow Loop

A schematic of the flow loop used for this study is given in Figure 4-1a. Three input velocity waveforms at six mean Reynolds numbers were tested for a total of 18 cases. The three input waveforms shown in Figure 4-1b, 4-1c, and 4-1d are referred to as Long Deceleration (LD), Symmetric (SYM), and Long Acceleration (LA), respectively. The six mean Reynolds number used were 500, 1000, 2000, 2500, 3000, and 4000. A computer-controlled gear pump generated all pulsatile waveforms. Due to pump limitations, the cycle duration of each waveform was two seconds, rather than the physiologically typical one second cycle. A straight and rigid tube (FEP) with 1/8" inner diameter and 1/16" wall thickness was used for the test section. A 150-diameter length of the straight tubing preceded the test section to ensure fully developed flow. Water (ρ = 1000 kg/m3, ν = 8.9e-6 m2/s) was used as the working fluid, which has the same index of refraction as FEP. The test section was submerged in the working fluid to reduce optical distortion in the PIV images.
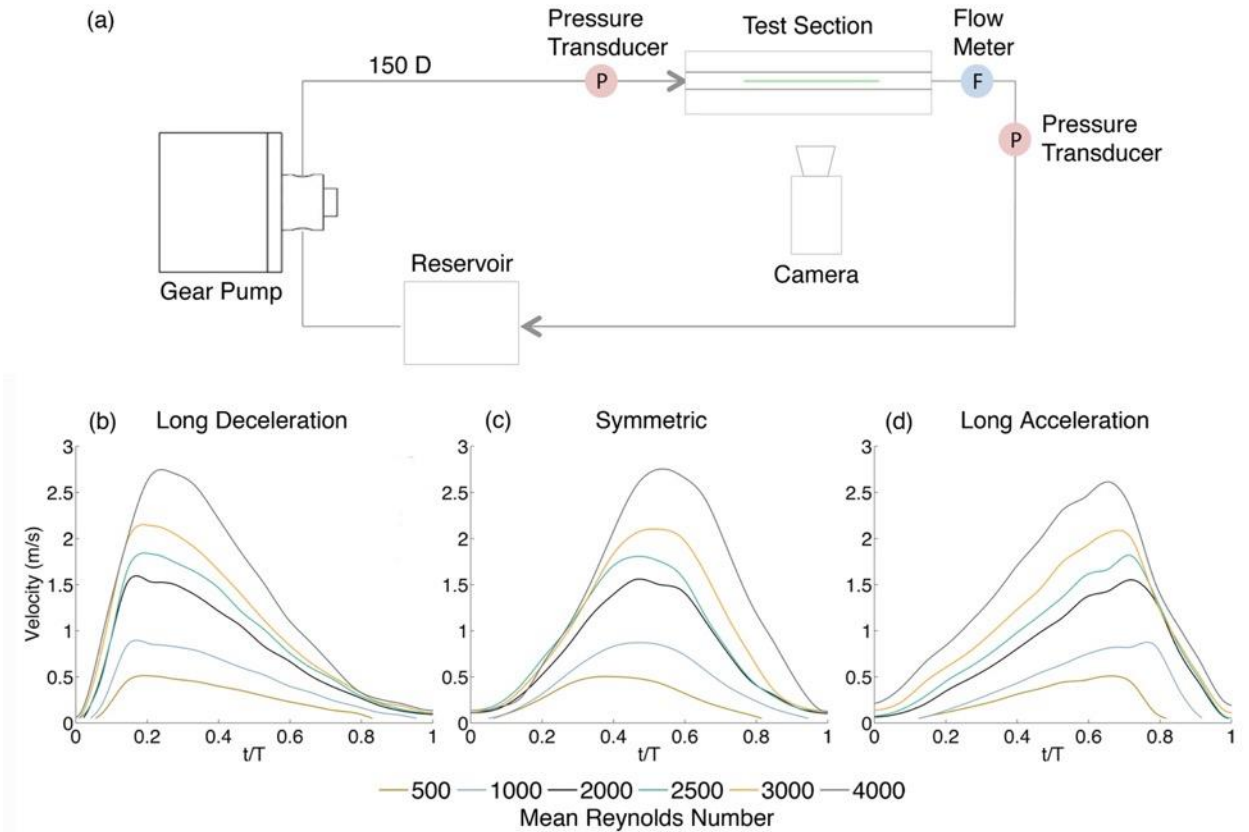
Figure 4-1: (a) Flow loop and planar particle image velocimetry experimental schematic. The test section was submerged in a box filled with the working fluid and the laser sheet vertically pierced the center of the pipe. F and P denote the locations of the flowmeter probe and pressure transducers, respectively. Arrows indicate flow direction. The input waveforms with time non-dimensionalized by the duration of one pulsatile cycle, T, for all eighteen cases: (b) long deceleration, (c) symmetric, (d) long acceleration.

4.3.2 Measurement Technique

PIV images were captured using a high-speed camera (Phantom Miro) and Nd-YLF laser (Continuum Terra-PIV, $\lambda = 527$ nm). The laser sheet was less than 1 mm thick and aligned with the center of the tube. Flow was seeded with 3 μm fluorescent particles. The experimental design needed to balance the need for a high repetition rate such that temporal gradients could be validly computed, the limited camera buffer size (number of images able to be captured per recording) at full resolution, and the desire for the most number of cycles to be captured. As such, double pulsed images were captured at a frame pair frequency of 250 Hz, such that temporal gradients could be computed. The inter-frame time, given in Table 4-1, varied by Reynolds number to maintain a maximum displacement in the entire cycle of approximately 15-pixel. The captured images were

full camera resolution (2560 x 1600 pixels) to obtain the highest possible spatial resolution. The camera magnification was 2.29 μm/pix. Two pulsatile cycles were captured for each case, which at this frame rate and resolution corresponds to the full buffer size of the high-speed camera used.

Table 4-1: Inter-frame time used for each mean Reynolds number case.

Mean Reynolds Number	Inter-frame time, dt (μs)
500	69.845
1000	30.800
2000	19.798
2500	15.831
3000	13.341
4000	8.795

PIV images were processed using an in-house code, Prana (https://github.com/aether-lab/prana). Three passes of an iterative image deformation algorithm were computed [72]. Robust phase correlation was used [73,74]. The last PIV pass used a 64 x 64 pixel window size with a 50% Gaussian window [75] to reduce spectral leakage in the velocity correlation calculation, resulting in a 32 x 32 pixel effective window size. An 8 x 8 pixel grid size was used for the final pass, making the resulting velocity field 199 x 226 vectors. A median-based universal outlier detection (UOD) with a window size of 3 x 3 for the first pass and 5 x 5 for the second pass was used [76]. No validation was used for the final PIV pass. The uncertainty of the resulting PIV velocity fields was estimated using a peak-to-peak ratio method [77,78]. The 1σ and 2σ confidence interval uncertainty estimates were similar across all cases, at approximately 0.08 and 0.2, respectively, as is typical for a well-controlled PIV experiment.

PIV velocity fields were filtered using proper orthogonal decomposition (POD). The entropy line-fit (ELF) thresholding criterion was used to autonomously determine the optimal threshold for each dataset [112]. The ELF method has been shown to better preserve small-scale modes and improve the turbulence spectrum as compared to the traditional energy threshold method [112]. Table 4-2 gives the number of modes kept out of the 998 snapshots for each test case, which corresponded to approximately 99.7% of the energy for all cases. UOD was subsequently used on the POD filtered velocity fields to eliminate any residual outliers. Finally,

the two pulsatile cycles were phase averaged. The resultant velocity fields are referred to as the 'filtered PIV velocity' for the remainder of the paper.

Table 4-2: Number of POD modes retained using 998 snapshots for each case.

Mean Reynolds Number	Input Waveform		
	SYM	LA	LD
500	36	33	35
1000	78	79	84
2000	207	188	189
2500	205	213	217
3000	240	225	234
4000	228	229	243

4.3.3 Post Processing

The fluctuating velocity components were computed according to the Reynolds decomposition expressed as

$$u_i' = U_i - \langle U_i \rangle \qquad \text{(Equation 4.1)}$$

where u_i' is the fluctuating velocity, U_i is the filtered PIV velocity, and $\langle U_i \rangle$ is the mean velocity. Because a pulsatile waveform is used here, $\langle U_i \rangle$ is not constant in time and cannot be computed using an ensemble average. Further, the trade-off between a high frame pair frequency to allow temporal gradients to be computed and the limited camera buffer size meant only two cycles could be recorded. As such, a traditional triple decomposition method, which uses phase-locked ensemble averages, as employed in Trip et al. [32] also could not be used here. Instead, a filtering approach was needed to remove fluctuations and identify the underlying pulsatile trend as an ensemble average does. Thus, at each point in space, the discrete wavelet transform (DWT) was used to identify the temporally varying mean u-velocity component, as illustrated in Figure 4-2a. Discrete wavelets act as a filter bank, decomposing an input signal using successive high-pass and low-pass filters at each level, resulting in approximate (low-pass) and detail (high-pass) coefficients [113–115]. The approximate coefficients at each filter level can be reconstructed to produce a de-noised version of the input signal, which in this case extracts the $\langle U_i \rangle$ component. For all cases here, $\langle U_i \rangle$ was computed as the reconstruction of the fifth-level approximate

71

coefficients which was found to best remove all fluctuations while preserving the underlying pulsatile trend. Because unidirectional pipe flow was studied here, the mean velocity in the v-component was assumed to be 0 for all time steps. Figure 4-2b shows a sample u'_i signal. To compare the ensemble average and DWT approaches, an analytical sine signal with 50 cycles and 5% added Gaussian noise—a typical amount of fluctuations expected for a turbulent flow—was created. For the ensemble approach, the 50 cycles were averaged. For the DWT approach, two sequential cycles were selected and subsequently phase averaged (as was done for the experimental data), then the DWT was used to extract the underlying waveform. Figure 4-2c compares the results of the ensemble and DWT approaches with the analytical solution computed by performing an ensemble average on the analytical signal before Gaussian noise was added. In Figure 4-2c, the DWT signal shown is the average of all sequential two-cycle solutions. Figure 4-2c demonstrates that the DWT was able to accurately extract the underlying waveform. Further, even with 50 cycles, the ensemble average still contained some fluctuating behavior. Figure 4-2d shows the DWT approach had a 4% variation across all sequential-two cycle solutions (i.e. cycles 3 and 4 vs. cycles 36 and 37). Together Figures 4-2c and 4-2d suggest that the DWT approach may cause a 4% uncertainty in the fluctuating velocity for each point in space, but this uncertainty is negligible for
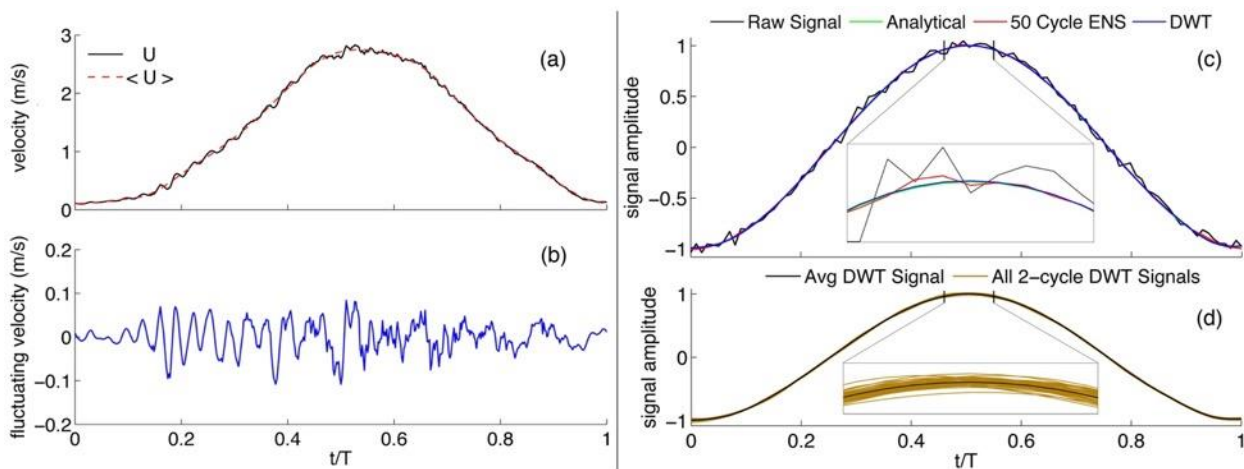
Figure 4-2: Schematic of computing the fluctuating velocity component using the discrete wavelet transform (DWT). (a) The raw u-velocity component and the mean u-velocity component, <U>, computed as the reconstruction of the fifth-level approximate wavelet coefficients. (b) The resulting fluctuating u-velocity component. (c) A comparison of the DWT and ensemble average approaches using an analytical, 50-cycle sine signal with additive Gaussian noise. The DWT-based solution shown is the average of all possible sequential two-cycle solutions (d) The variation in the DWT approach based on each sequential two-cycle solution.

results which are spatially averaged. Therefore, because this uncertainty is low similar to that of the ensemble average, the DWT approach is reasonable for this study. Further, because most results presented here are spatially averaged, the DWT approach is not expected to influence the findings of this study.

TKE and turbulence intensity (TI) were subsequently computed according to Equation (4.2) and (4.3), respectively.

$$K(t) = \frac{1}{2}(u'(t)^2 + v'(t)^2) \qquad \text{(Equation 4.2)}$$

$$I(t) = \frac{1}{u_c(t)}\sqrt{\frac{1}{2}(u'(t)^2 + v'(t)^2)} \qquad \text{(Equation 4.3)}$$

where K is the TKE (m_2/s_2), I is TI (%), u_c is the centerline velocity (m/s), and t is time. The axial line average of the fluctuating velocity was subtracted from each fluctuating velocity field, as detailed in Trip et al. [32], to minimize the effect of pump fluctuations on the TKE and TI calculations. Coherent structures were identified using the λ_{ci} criterion [79], which computes the eigenvalues of the spatial velocity gradient matrix at each vector point and selects the maximum imaginary portion of the eigenvalues. The magnitude of λ_{ci} represents the relative strength of the coherent structure. A 10% threshold was used to filter noise within each temporal λ_{ci} field.

To analyze the TKE budget, dissipation, production, and pressure diffusion were computed for all test cases. Dissipation was computed using the energy spectra curvefit method designed specifically for PIV experimental data and described in Xu and Chen [116] and mathematically expressed by

$$\epsilon = \left(\frac{55}{18C_k}k_1^{5/3} \cdot E_{11}(k_1)\right)^{3/2} \qquad \text{(Equation 4.4)}$$

where ϵ is dissipation rate (m_2/s_3), k_1 is the wavenumber in the axial direction, E_{11} is the energy spectra, and C_k is the Kolmogorov constant and set to 0.5 for this analysis. Only wavenumbers in the inertial sub-range were used to compute the dissipation range. A Hanning window was used when computing the E_{11} spectra. The PIV interrogation windows essentially act as a filtering operation, which causes the computed energy spectra to tail off the -5/3 Kolmogorov spectrum [116,117]. The modified curvefit method [116] corrects the windowing effect by adjusting E_{11} according to

$$\widetilde{E_{11}} = |G(k_1)|^2 E_{11}(k_1) \qquad \text{(Equation 4.5)}$$

where $\widetilde{E_{11}}$ is the modified energy spectra and $G(k_1)$ is the Fourier transform of the PIV windowing filter kernel. In this case, a 50% Gaussian windowing filter was used [75]. With the modified method, $\widetilde{E_{11}}$ is used in Equation (4.4), and has been demonstrated to be more accurate with fully turbulent flow fields [116]. For laminar and transitional flow, however, the PIV window filtering effect is not as prominent because fluctuating velocity components are not as prevalent. Thus, employing the correction given in Equation (4.5) will introduce more error into the energy spectra. In this experiment, because a large range of mean Reynolds numbers were used, a combination of the curvefit and modified curvefit methods were employed. For each E_{11} and corresponding $\widetilde{E_{11}}$ spectra in space and time, the spectra whose slope was closer to the -5/3 Kolmogorov spectra was used to compute the dissipation rate for that axial location and time.

Production and pressure diffusion were computed according to Equation (4.6) and Equation (4.7), respectively,

$$P = -u_i' u_j' \frac{\partial \langle U \rangle_i}{\partial x_j} \tag{Equation 4.6}$$

$$\Pi = -\frac{1}{\rho} \frac{\partial (p' u_i')}{\partial x_i} \tag{Equation 4.7}$$

where P is production, Π is pressure diffusion, ρ is density (kg/m3), and p′ is the fluctuating pressure (Pa). All gradients were computed using a compact Richardson differentiation scheme which has been shown to be noise optimized for PIV data [80]. To minimize persisting numerical differentiation noise, fluctuating velocity and pressure fields were smoothed using the Wiener filter [86] and the DWT. Pressure was computed using an in-house omni-directional Navier-Stokes pressure solver, described in Charonko et al. [50] This method has been validated using turbulent nozzle flow, demonstrated using both laminar and turbulent flows, and required no boundary conditions for this application since only the fluctuating pressure component was needed.

The Stokes length, $l_s = \sqrt{2\nu/\omega}$, where ω is the radian frequency of pulsation, was 0.75 mm for all test cases since the pulsation frequency was constant. The non-dimensional Stokes length $l_s^+ = l_s u_\tau / \nu$ was subsequently computed, where u_τ is the friction velocity. To compute $u_\tau = \sqrt{\frac{\tau_w}{\rho}}$, thin plate spline (TPS) radial basis functions (RBF), optimized to reduce numerical noise in PIV data, were used to calculate the wall shear stress, τ_w [51]. The friction velocity was computed using the mean velocity. The non-dimensional wall unit was defined by $y^+ = y u_\tau / \nu$.

4.4   Results and Discussion

4.4.1   Exploring the Flow and Development of Turbulent Structures

The flow profiles and turbulent structures were first evaluated in order to validate the experimental setup and identify the locations and development of turbulent structures.

Figure 4-3 shows the velocity profiles at each mean Reynolds number, averaged axially and temporally. For the low mean Reynolds number cases of 500 and 1000, the analytical Poiseuille flow solution is also plotted for reference. For all mean Reynolds number cases, good agreement is observed between the different cases. These results validate the fully developed flow characteristics for this experiment. As seen in Figure 4-3, only the mean Reynolds number case of 500 shows a profile similar to the laminar flow solution. By a mean Reynolds number of 1000, the profile was more uniform in the core region and maintained higher wall gradients, as is typical of a turbulent velocity profile. The velocity profiles for all cases at and above a mean Reynolds number of 2000 are similar and resemble a fully developed turbulent profile. Because all cases go
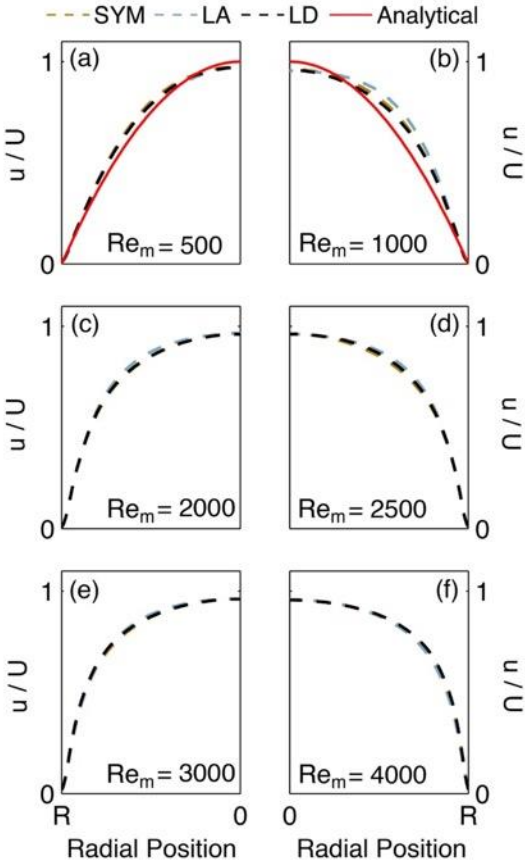
Figure 4-3: Axially and temporally averaged velocity profiles all experimental cases. For low mean Reynolds number cases, the analytical Poiseuille flow solution is plotted.
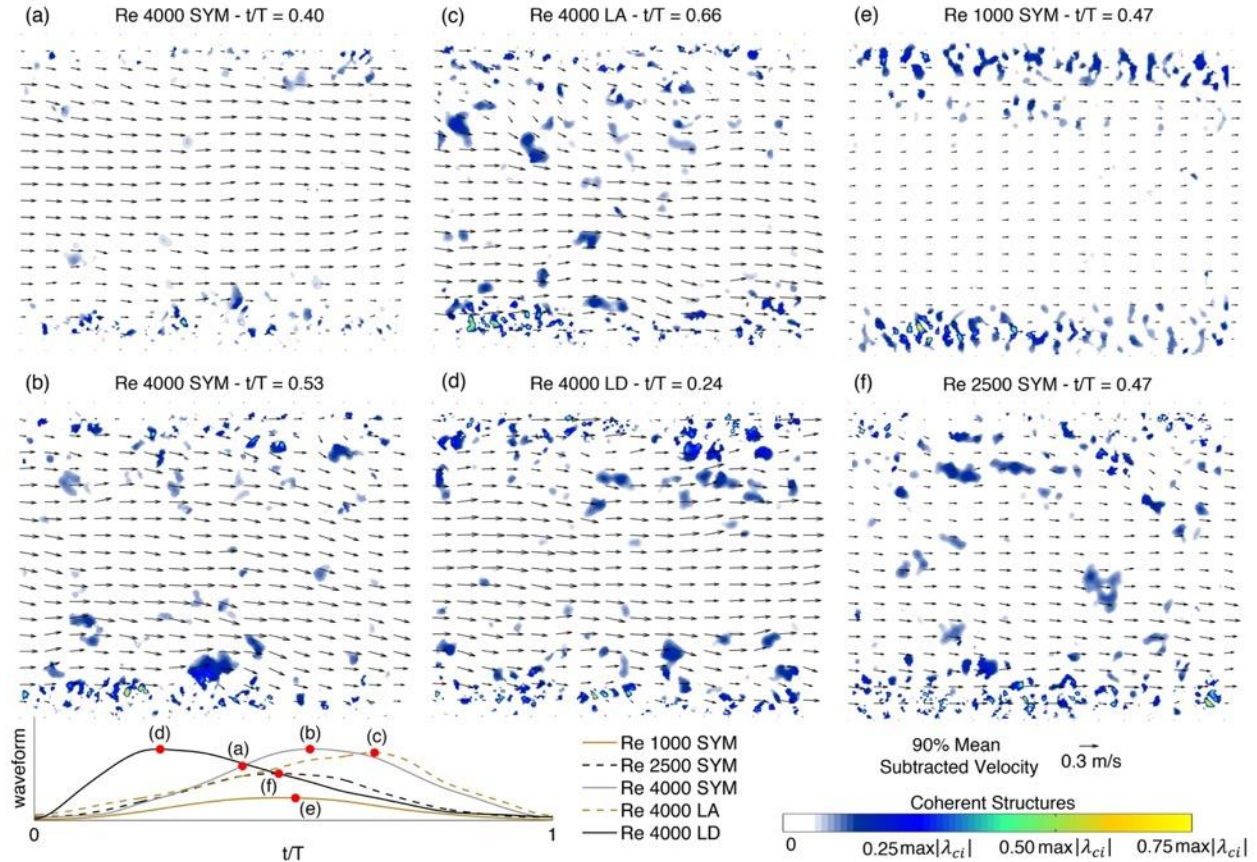
Figure 4-4: Flow contour snapshots for various mean Re cases, waveforms, and points in the pulsatile cycle including (a) and (b) the mean Re of 4000, SYM case, (c) the mean Re of 4000, LA case, (d) the mean Re of 4000, LD case, (e) the mean Re of 1000, SYM case, and (f) the mean Re of 2500, SYM case. Vector fields shown are the flow velocity with 90% of the mean flow subtracted. Coherent structures computed using the 90% mean subtracted velocity are overlaid. All coherent structures fields are normalized their respective maximum λci value. The contours represent the λci value, indicating the relative strength of the coherent structure.

down to a zero flow rate throughout the pulsatile cycle, they all range up to high Reynolds numbers at peak flow rate (i.e. the mean Re 4000 cases range up to an instantaneous Reynolds number of about 10000). Therefore, the turbulent flow profiles, even at low mean Reynolds numbers, are expected.

Figure 4-4 investigates the dynamics of the flow instabilities and turbulent structure formation for all waveforms and three mean Reynolds number cases. In Figure 4-4, the 90% mean subtracted flow vectors and coherent structures in the flow domain are illustrated. Figures 4-4a and 4-4b show the mean Reynolds number of 4000 SYM case at about 75% acceleration and peak flow rate, respectively. It is observed in Figure 4-4a that flow instabilities began to form in the

near wall region, as expected due to the higher shear gradients in this region as a result of the no-slip condition. Subsequently, turbulent coherent structures formed at the location of these flow instabilities. As the flow continued to accelerate to peak flow rate, these structures were ejected from the wall and moved into the core flow, as seen in Figure 4-4b. Alternatively, some structures are swept back to the wall, as observed in Figure 4-4b and 4-4c, where flow vectors radially inward of some structures direct back towards the wall. Figures 4-4b, 4-4c, and 4-4d compare the structures at peak flow rate for the mean Reynolds number of 4000 SYM, LA, and LD cases, respectively. All waveform cases had similar turbulent structure distributions, suggesting that the input waveform did not affect the radial location where the structures form. Figures 4-4b, 4-4d, and 4-4e compare the structures at peak flow rate for the SYM waveform at mean Reynolds numbers of 4000, 1000, and 2500, respectively. The thickness of the near-wall region where structures primarily developed increased as the mean Reynolds number decreased. This notion is
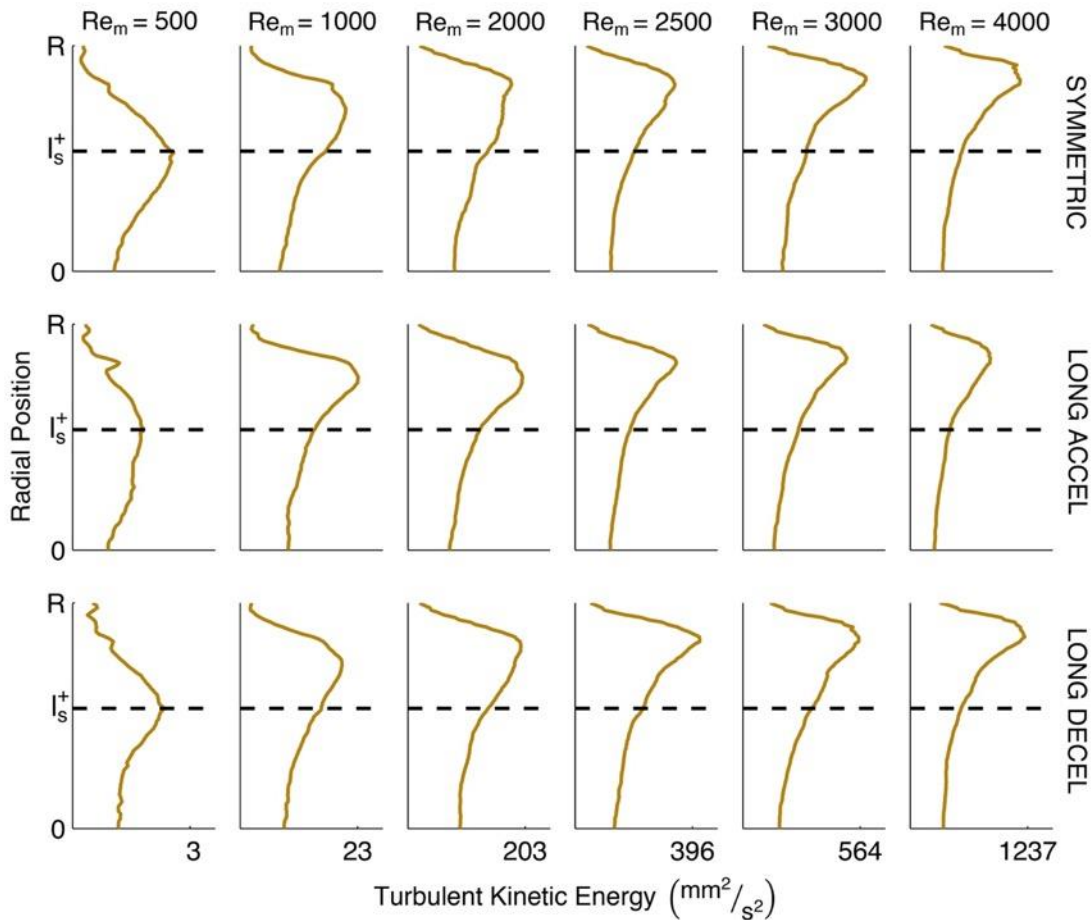
Figure 4-5: TKE as a function of radial position for all test cases. TKE is averaged axially and temporally. The non-dimensionalized Stokes length, l_s^+, is shown in all cases.

explored in more detail in Figure 4-5 and the subsequent discussion. In the mean Reynolds number case of 1000, minimal structures are observed in the core flow, suggesting that no ejection motions occur at the lower mean Reynolds number cases. Analysis of the TKE budget is needed to determine when and why the ejection motions occur in this pulsatile transition flow domain.

Figure 4-5 shows the TKE as a function of radial position for all test cases. Here, TKE was temporally and axially averaged. As the mean Reynolds number was increased, the peak TKE moved radially outward. The peak TKE location moved from an r/R of 0.65 to 0.86 to 0.94 through the mean Reynolds numbers of 500, 2500, and 4000, respectively, for all waveforms. As the mean Reynolds number is increased, the near-wall layers including the viscous sub-layer and buffer layer are expected to be thinner. Thus, an interaction between these layers and the location of turbulence structure formation is suggested. This agrees with the results of previous studies which have stated shear and pressure waves that contribute to the generation of turbulence originate in the viscous and buffer layers [104,105]. Because results were similar across all waveforms, it can be concluded that the peak TKE radial location is not affected by temporal velocity gradients.

The non-dimensionalized Stokes length, l_s^+, is indicated in Figure 4-5. Because all test cases utilized the same pulsatile frequency and thus Womersley number, the Stokes length was the same for all cases at r/R of 0.54. Previous studies have indicated that turbulence production and TKE primarily occurs at l_s^+ and an interaction between the Stokes layer and turbulence production exists [104,105]. However, for this study, such a relationship was only observed at a mean Reynolds number of 500. Because the Stokes length only depends on pulsating frequency and does not consider mean Reynolds number or the oscillation amplitude, it fails to accurately describe the TKE production at the higher mean Reynolds numbers used here. It is plausible this discrepancy is related to the amplitude of oscillation which is much greater for this study than those that use the traditional sinusoidal waveform. Trip et al. [32] demonstrated that the Reynolds number using the oscillation amplitude as the characteristic velocity failed to indicate when the onset of transition occurred, but did not explore how the oscillating Reynolds number altered the radial location of peak TKE. Such a notion would need to be explored in future studies.

4.4.2 Comparing the Input Waveforms

The formation of turbulent structures and radial location of peak TKE was observed to only be affected by the changing mean Re and not the different input waveforms. In order to compare
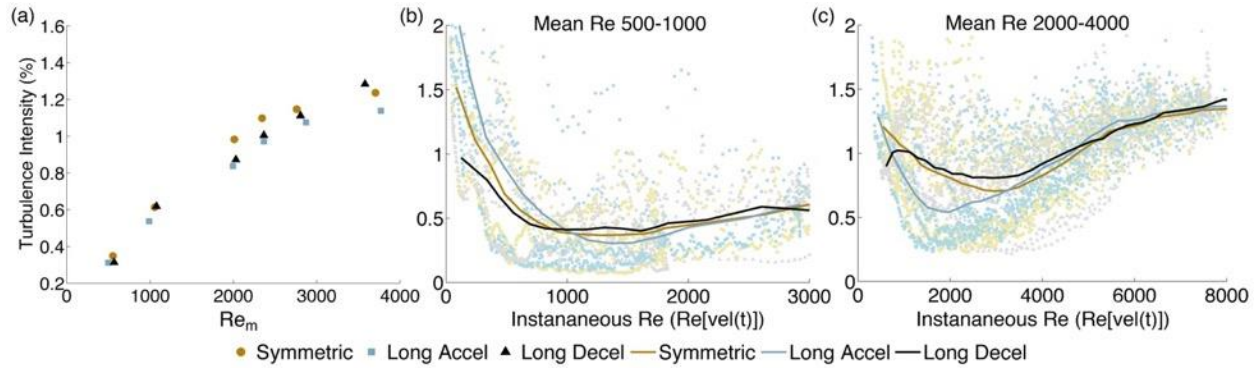
Figure 4-6: (a) Space and time averaged turbulence intensity for all test cases. Turbulence intensity as a function of instantaneous Reynolds number for (b) low mean Reynolds number regimes of 500 and 1000 and (c) high mean Reynolds number regimes of 2000, 2500, 3000, and 4000. Lines show the histogram of points using approximately fifty points per bin.

the differences in the onset transition across the different input waveforms, the turbulence intensity trends for each case were analyzed.

Figure 4-6a illustrates the average turbulence intensity for each test case. The LA case on average maintained a 12 and 7% lower turbulence intensity for all mean Reynolds numbers than SYM and LD, respectively. SYM had the highest average turbulence intensity of 0.98, 1.10, and 1.15%, at the mid-range mean Reynolds numbers of 2000, 2500, and 3000, respectively. However, the differences in the average turbulence intensity were in general small (about 0.1%). Figures 4-6b and 4-6c show the turbulence intensity as a function of instantaneous Reynolds number, or the Reynolds number defined using instantaneous velocity magnitudes in space and time. In the low mean Re regimes, shown in Figure 4-6b, all input waveforms had similar turbulence trends. However, in the higher mean Re regimes shown in Figure 4-6c, the LA case maintained about a 33% lower turbulence intensity across the range of transitional instantaneous Reynolds numbers (Re ≈ 1500-3000) than both the SYM and LD waveforms, suggesting that this waveform delayed the onset of transition. Conversely, the LD waveform had the highest turbulence intensity through this range of Reynolds numbers, suggesting it had the earliest onset of transition.

Figure 4-7 shows the temporal variation of turbulence intensity for all test cases. As evident in Figure 4-7a, because all velocity waveforms went to zero ($u_c \to 0$), the turbulence intensity calculation was mathematically unstable and infinitely large at the beginning and end of the cycle where the centerline velocity goes to zero. At a mean Reynolds number of 500, the SYM and LD waveforms had intermittent spikes in the turbulence intensity through the middle of the cycle,

79
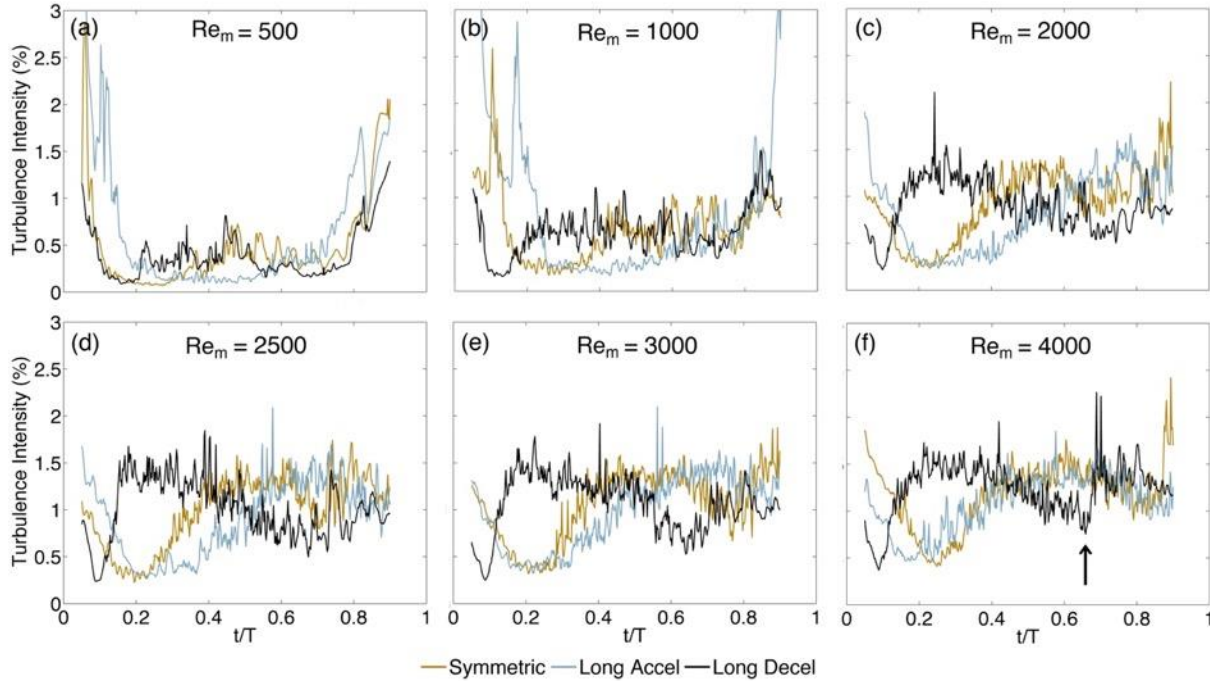
Figure 4-7: Spatially-averaged turbulence intensity through time for all input waveforms at mean Reynolds numbers of (a) 500, (b) 1000, (c) 2000, (d) 2500, (e) 3000, and (f) 4000.

suggesting the beginning of a transitional regime. The LA waveform did not show any intermittency until a mean Reynolds number of 1000, again demonstrating a delay of the onset of turbulence. However, because the turbulence intensity calculation is mathematically unstable shortly after the LA peak flow rate it is difficult to evaluate the turbulence intensity through the deceleration portion of the cycle from this analysis. At the higher mean Reynolds numbers of 3000 and 4000 a distinguishable spike was observed at t/T of about 0.65 in the LD waveform, likely indicating a return from a turbulent to a transitional regime, further demonstrating the LD waveform had the earliest onset of transition. Such results qualitatively match expectation as previous studies have indicated the deceleration phase of the pulsatile cycle contains the highest turbulence intensity [32,107,109].

The deceleration phase is characterized by an adverse pressure gradient, which has been observed to cause the near-wall flow to become unstable, increasing vortical flow and shear in this region [19,61]. This effect is realized by the LD waveform, which maintained this adverse pressure gradient for the longest time, and was observed to facilitate the most turbulence production. However, the deceleration phase of the LA waveform had a larger adverse pressure gradient

80

magnitude as compared to the SYM and LD waveforms. Therefore, these results suggest that the duration of the adverse pressure gradient is more influential in causing instabilities than the magnitude of the adverse pressure gradient. Conversely, the peak turbulence intensity for the LD waveform in Figures 4-7d-4-7f were approximately the same at 1.5%, suggesting that turbulence production is an asymptotically limited process where a point exists such that further increases to the acceleration rate and oscillation amplitude will not produce more turbulence. The SYM and LA waveforms demonstrated similar trends through the acceleration period, suggesting that the shape of the acceleration portion of a pulsatile cycle does not strongly influence turbulence production. Thus, this analysis concludes that the duration of the deceleration phase and magnitude of acceleration are most influential in the development of transition, while the magnitude of deceleration and duration of acceleration have minimal effect.

4.4.3   Investigating the TKE Budget

To identify and explain the underlying cause of the differences in the onset and development of transition by the different input waveforms, the TKE budget must be broken down and analyzed.

Figure 4-8 illustrates the dissipation rate, production, and pressure diffusion as a function of radial position. All terms have been averaged temporally and axially. Because of the limited PIV spatial resolution and noise expected in the gradient-based production and pressure diffusion terms, quantitative comparisons across the different terms cannot be made. Thus, all terms shown in Figure 4-8 were normalized to the same scale following averaging. The trends across all cases, for all terms, were similar, again indicating that no interaction existed between temporal velocity gradients and the radial location of maximum dissipation or production. At the higher mean Reynolds numbers of 2500 and 4000, the production peaks matched that of the radial TKE at r/R of 0.86 and 0.94, respectively. Dissipation remained in the very near wall region of r/R of 0.98 throughout all mean Reynolds numbers. At low mean Reynolds numbers of 500 and 1000, the pressure diffusion in the near wall region is positive, indicating that throughout the pulsatile cycle, pressure waves were primarily transporting turbulence towards the wall. However, for all other mean Reynolds numbers, the pressure diffusion is negative in the near wall region, indicating that it transported turbulence away from the wall into the core region of the flow. One possible explanation for this is that for the low Reynolds number cases, instabilities and vortical structures

are produced within the Stokes layer, swept back to the wall by the pressure waves, and subsequently dissipated. However, as the mean Reynolds number increases to 2000-3000, the turbulence production rate exceeds the dissipation rate, and the TKE budget is no longer in a stable equilibrium. This causes the pressure waves to transport the residual turbulence away from the wall, into the core flow and increasing the overall turbulence intensity in the flow domain. Such an explanation is in accord with He and Jackson [104] who suggested pressure is responsible for redistributing turbulence from the axial to transverse direction.

Figure 4-9 compares the turbulence intensity, total dissipation, and total production. Total dissipation and production are defined as the integral of spatially averaged dissipation and production rates through time. Figure 4-9b demonstrates that turbulence dissipation was relatively
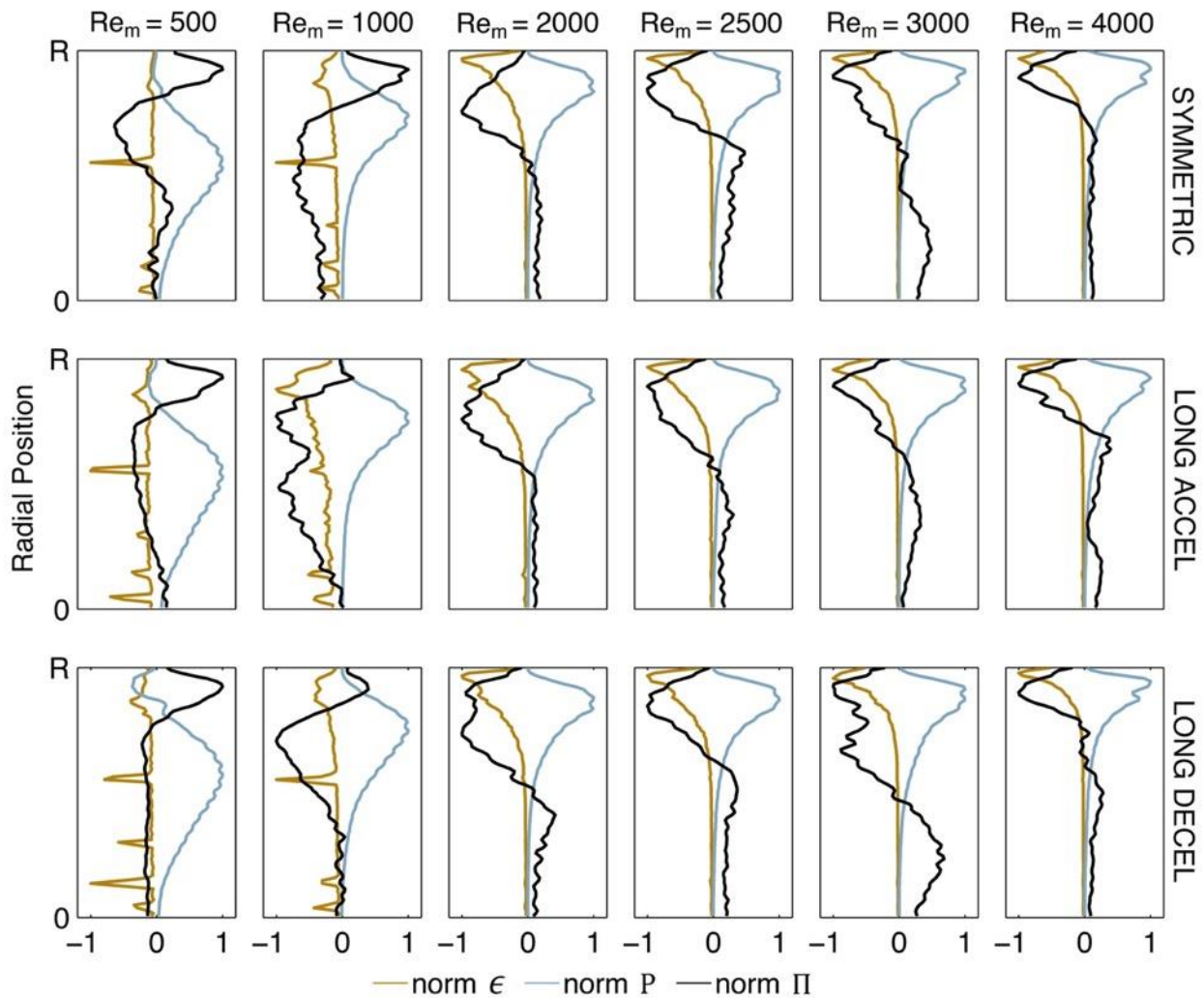
Figure 4-8: Normalized dissipation (ϵ), production (P), and pressure diffusion (Π) as a function of radial position for all test cases. All parameters are averaged axially and temporally.

82
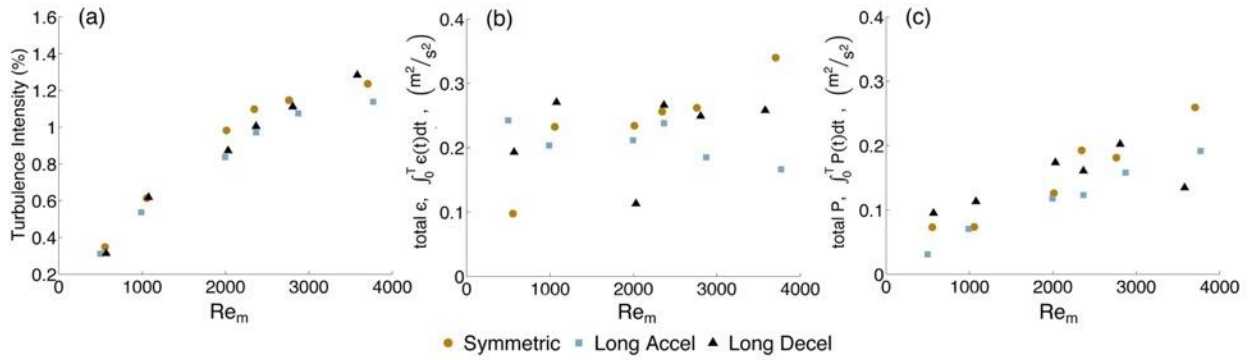
Figure 4-9: (a) Space and time averaged turbulence intensity, (b) Space and time averaged total (integrated) dissipation for all test cases, and (c) Space and time averaged total (integrated) production, for all test cases.

similar for all mean Reynolds numbers. The SYM, LA, and LD waveforms averaged total dissipation values of 0.24, 0.21, and 0.23 m2/s2, respectively, across all mean Reynolds numbers. The fact that dissipation was independent of mean Reynolds number implies it is also independent of the mean velocity magnitude. Alternatively, turbulence production shown in Figure 4-9c increased with increasing mean Reynolds number. The trend in Figure 4-9c matches that of the turbulence intensity shown in Figure 4-9a, suggesting that production most prominently describes the turbulence characteristics of the flow. The LA waveform had about 20% lower total production than the other two waveforms across all but the highest mean Reynolds number of 4000. Production for the LD waveform at a mean Reynolds number of 4000 had a 25% decrease from the 2000-3000 mean Reynolds numbers. This observation supports the notion that turbulence production is asymptotically limited. Alternatively, this can viewed as a temporal velocity gradient limit, such that production is constant beyond a certain temporal velocity gradient. By design, the SYM and LA waveforms had smaller temporal velocity gradients in the acceleration phase than the LD waveform and thus did not demonstrate this limit in turbulence production but rather increased linearly. These results coupled with the proposed explanation of the function of the pressure diffusion waves would plausibly explain the traditional hyperbolic tangent-type trend of the turbulence intensity versus mean Reynolds number plots observed in previous literature [32], and suggest that two critical Reynolds numbers exist in a given flow. The first critical Reynolds number is achieved when the production rate exceeds the dissipation rate, at which point the pressure waves begin to transport turbulence away from the wall rather than stably confine it to
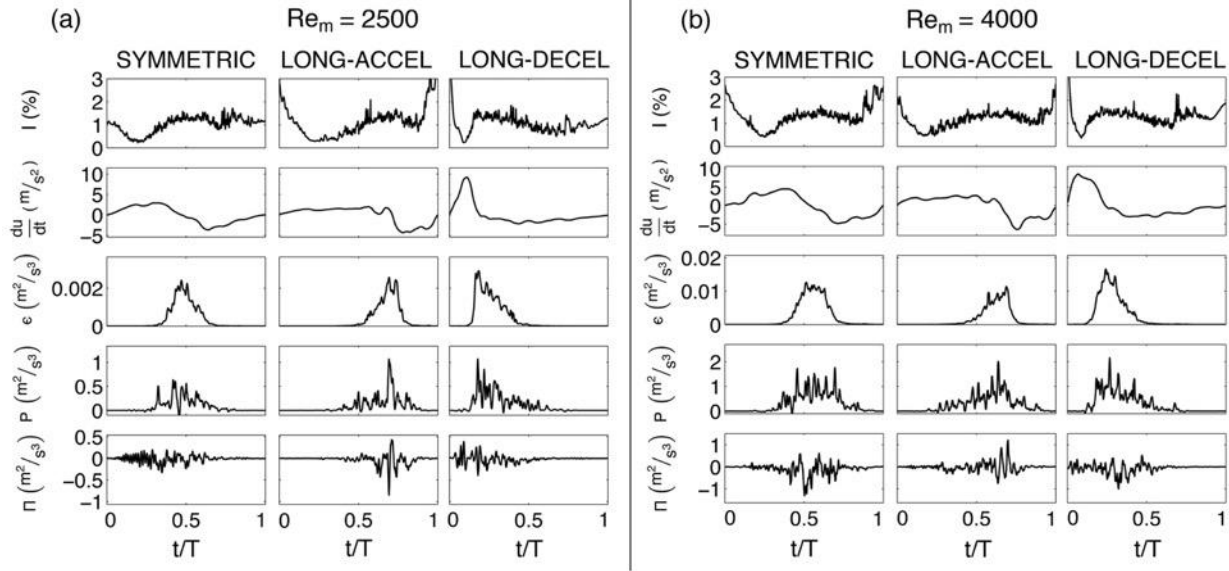
Figure 4-10: Turbulence intensity (I), temporal input velocity waveform gradient (du/dt), dissipation (ϵ), production (P), and pressure diffusion (Π) trends through time for all input waveforms at mean Reynolds numbers of (a) 2500 and (b) 4000.

the wall. The second critical Reynolds number occurs when the turbulence production reaches its asymptotic limit such that further increases in flow oscillations or disturbances do not increase the rate of turbulence production. The second critical Reynolds number described here represents the traditional critical Reynolds number. This idea of two critical Reynolds numbers for pulsatile flows would better represent the results of previous studies as well. For example, as previously mentioned in Section 4.2, Trip et al. [32] found that at lower Womersley numbers, transition occurred more gradually. A lower Womersley number flow would have a lower acceleration magnitude and longer duration of deceleration as compared to a higher Womersley number flow. The latter suggests instabilities occur at a lower Reynolds number, so that the first critical Reynolds number would also be lower, while the former would mean the asymptotic production limit would be occur at a higher Re, delaying the second critical Reynolds number. Thus, the notion of two critical Reynolds numbers could explain the underlying mechanism behind the finding in Trip et al. [32] and would explain the finding here that magnitude of acceleration and duration of deceleration are the most influential parameters on pulsatile transition.

The above analysis noted a relationship between temporal velocity gradients and the TKE budget, but did not define this relationship. Figure 10 compares the temporal trends the turbulence intensity, velocity gradient, dissipation rate, production, and pressure diffusion for mean Reynolds

numbers of 2500 and 4000. For the SYM and LA waveforms, it is evident that the pressure diffusion was only prominent following significant turbulence production in the flow field. However, for the LD waveform the pressure diffusion shows significant fluctuations before turbulence production. This suggests that the short and rapid acceleration associated with the LD waveform caused increased near-wall instabilities and an early onset of the pressure redistribution or first critical Reynolds number described above. Such a notion lends further explanation to the increased turbulence intensity observed in the LD waveform. The similarities between the production and turbulence intensity trends reveal the same conclusion made in Figure 9, namely that production was the primary mechanism driving the turbulence intensity. The production lasted for a longer period of the pulsatile cycle than the dissipation (e.g. 75 versus 40% of the cycle, respectively, for the mean Reynolds number of 4000 case, Figure 4-10b). In both mean Reynolds number cases, the dissipation had a well-defined region in the flow where it was significant and was zero otherwise. Comparing this non-zero portion with the velocity gradients, it is evident that the dissipation rate began to rise when the slope of the velocity gradient became negative. Further, the dissipation rate began to decay when the magnitude of the velocity gradient became negative (i.e. when the flow was slowing down). From this analysis, the dissipation rate seemed to depend on the sign of the velocity gradient and the sign of the slope of the velocity gradient. Figure 4-11 explicitly explores this relationship. In Figure 4-11 four "quadrants" have been defined based on the signs of the velocity gradient, or acceleration, and slope of the acceleration curve. Physically, quadrant 1 would represent the case where the velocity gradient and its slope are both positive, thus flow is accelerating at an increasing rate. Quadrant 4 would represent the case where the velocity gradient is positive, but its slope is negative, thus flow is still accelerating but at a decreasing rate. Quadrants 2 and 3 can be defined similarly.

Figure 4-11 confirms that a well-defined relationship between the acceleration, slope of the acceleration, and dissipation rate within the pulsatile flow exists. Specifically, the dissipation rate is non-zero only when the velocity gradient is greater than zero. For decelerating flow, no turbulent dissipation is occurring. This conclusion can provide some explanation for the numerous observations from this and previous studies that the deceleration phase of a pulsatile cycle contains the majority of the turbulence [32,107,109]. It is also important to note that Figures 4-9 and 4-11 show a rather unexpected finding that velocity does not affect dissipation, but acceleration and slope of acceleration strongly do. The acceleration and slope of the acceleration are directly
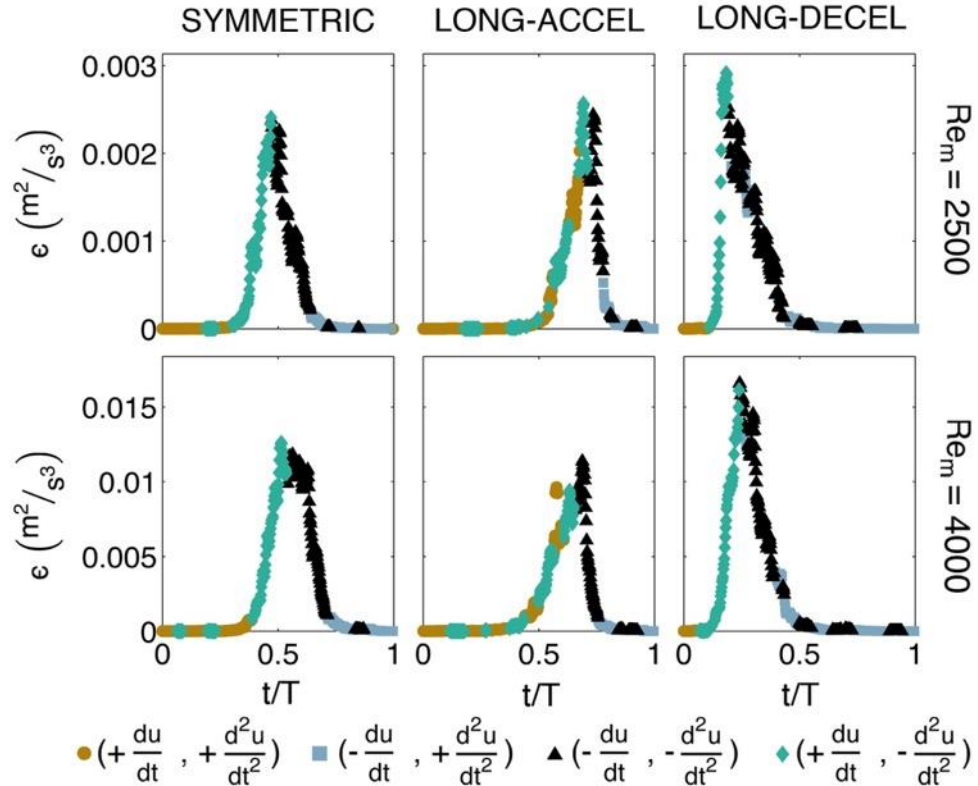
Figure 4-11: Dissipation (ϵ) as a function of time for all input waveforms at mean Reynolds numbers of 2500 and 4000. Each dissipation point is classified using a four-quadrant system based on the sign of the first and second derivatives of the input velocity waveform.

influenced by the pressure gradient, suggesting that this may be the underlying mechanism affecting the dissipation rate, a notion that would need to be explored in future studies. A critical implication of this relationship is that the temporal velocity gradient of a pulsatile waveform directly affects the dissipation rate and subsequently the onset and development of turbulence. Evaluating velocity gradients using traditional sinusoidal pulsatile waveforms may assist in further explaining the discrepancies in previous studies, specifically the differences observed at various Womersley numbers, and should be explored in future work.

4.4.4 Limitations

In this study, we utilize three unique input waveforms, all of physiological relevance. Because a large number of studies using steady flow and several studies using the traditional sinusoidal pulsatile waveform have been done, we did not test these domains here. Qualitative comparisons can be done between the results herein and previous studies using steady or sinusoidal

pulsatile flow, however future studies would need to explicitly define the differences between alternate waveforms, such as the ones used here, and steady flow and sinusoidal waveforms. Thus, all conclusions and findings are limited to the pulsatile flow domain.

In addition, gear pumps inherently induce fluctuations into the flow and since a flow straightener was not used, these fluctuations were not precisely controlled. Although physiological flow will have native fluctuations and pump fluctuations were mitigated by the previously mentioned u′ correction and phase averaging, this limitation implies these results cannot be used to identify or inform a global critical Reynolds numbers for these waveforms.

Dissipation, production, and pressure diffusion have received little attention in experimental pulsatile transition flow studies. Therefore, those results could not be validated with other transitional PIV studies and generalized conclusions of these results must be made with caution. The use of the energy spectra method versus differentiation methods for computing dissipation reduced noise in this metric, however due to the limited spatial resolution of PIV, the dissipation rate was likely under-resolved. Because of this bias in the dissipation rate, the TKE budget based on the components computed here may not balance and comparisons of values across the different TKE budget components cannot be made. Both production and pressure diffusion required the evaluation of numerical derivatives, resulting in noisy fluctuations in these results.

4.5   Conclusions

This study investigated the influence of the input pulsatile waveform, and thus temporal velocity gradients, on the onset and development of transition. The goals were to (i) identify differences in when the onset of transition occurs based on the input waveform shape and (ii) to use the TKE budget to explain the underlying mechanisms causing the differences in the onset of transition based on input waveform shape. The results demonstrated the rate of acceleration and duration of the deceleration phase were most influential in determining when the onset of transition occurred, such that waveforms with longer deceleration phases had an earlier onset of transition, while waveforms with shorter and more rapid deceleration delayed transition. The TKE budget calculations highlighted specific details on the role of production and dissipation in the pulsatile transitional regime and suggesting the existence of two critical Reynolds numbers. Because production was affected by the mean Reynolds number but the dissipation rate was independent of it, a point exists where turbulence production exceeds dissipation, causing turbulence to be

distributed into the core flow. However, turbulence production was asymptotically limited such that further increases to the flow acceleration rate did not produce more turbulence. Together these findings provide an explanation for the hyperbolic tangent shape of the traditional turbulence intensity by Reynolds number plots and the notion that lower Womersley numbers cause a more gradual onset of transition [32]. Dissipation rate was found to be independent of mean velocity, through a relationship between dissipation rate and the temporal flow acceleration was demonstrated. Further, no turbulent dissipation was found to occur in the deceleration phase of the pulsatile cycle.

Overall the results of this study demonstrated relationships between the temporal gradients of a pulsatile waveform and the mechanisms driving transition. These findings can, in part, explain some of the conflicting mechanisms and critical Reynolds numbers found in previous pulsatile transition literature as a result of differing Womersley numbers. Given these findings and the experimental limitations of this work, future studies are needed to assess the identified relationships in more detail. For example, the TKE budget should be explored using the traditional sinusoidal waveform at various Womersley numbers. In addition, tomographic measurements would provide more accurate turbulent structure identification and TKE budget calculations.

CHAPTER 5. HEMODYNAMICS OF STENT IMPLANTATION PROCEDURES IN CORONARY BIFURCATIONS: AN *IN VITRO* STUDY

5.1   Abstract

Stent implantation in coronary bifurcations presents unique challenges and currently there is no universally accepted stent deployment approach. Despite clinical and computational studies, the effect of each stent implantation method on the coronary artery hemodynamics is not well understood. In this study the hemodynamics of stented coronary bifurcations under pulsatile flow conditions were investigated experimentally. Three implantation methods, provisional side branch (PSB), culotte (CUL), and crush (CRU), were investigated using time-resolved particle image velocimetry (PIV) to measure the velocity fields. Subsequently, hemodynamic parameters including wall shear stress (WSS), oscillatory shear index (OSI), and relative residence time (RRT) were calculated. The pressure field through the vessel was non-invasively quantified and pressure wave speeds were computed. The effects of each stented case were evaluated and compared against an un-stented case. CRU provided the lowest compliance mismatch, but demonstrated detrimental stent interactions. PSB, the clinically preferred method, and CUL maintained many normal flow conditions. However, PSB provided about a 300% increase in both OSI and RRT. CUL yielded a 10% and 85% increase in OSI and RRT, respectively. The results of this study support the concept that different bifurcation stenting techniques result in hemodynamic environments that deviate from that of un-stented bifurcations, to varying degrees.

5.2   Introduction

Percutaneous coronary interventions on bifurcated coronary lesions represent a challenge for interventional cardiologists. Though a series of different stent implantation techniques have been described, uncertainty still exists regarding the best selection for each individual patient [118].

The (drug-eluting) stent implantation procedure aims to minimize the occurrence of both vessel thrombosis and in-stent restenosis which are the main phenomena causing major adverse cardiac events. The main stent failures (restenosis and thrombosis) have been associated with the flow dynamics of stented segments, thus calling for improvements in the assessment and minimization of local stent-induced hemodynamic changes [119,120]. Established correlations exist between the outcomes of a stent implantation procedure and its induced alterations of flow parameters such as wall shear stress (WSS), oscillatory shear index (OSI), and relative residence time (RRT). Decreases in WSS values as well as increases in OSI and RRT increase the risk of restenosis [120–122]. Compliance mismatch between the stent and the host vessel can also increase the risk of thrombosis [123].

Implantation techniques for coronary bifurcations can utilize one or two stents [118]. The simplest stent technique is the provisional side branch (PSB) method, which uses only one stent in the main vessel (MV). It is eventually followed by further interventions (like ballooning or stenting) in the side branch (SB). Conversely, double stenting strategies deploy stents in both the MV and the SB using various techniques. Among different double stenting techniques, the culotte (CUL) and the crush (CRU) have been widely adopted worldwide.

Clinical trials have been a primary method for evaluating stent implantation techniques. PSB is currently the preferred method largely due to its simplicity, and easier and shorter implantation procedure [124]. Short-term clinical trials have suggested that the PSB method produces less adverse events (8.0%) as compared to complex stenting techniques (15.2%) [125]. However, lower residual stenosis in the SB has been observed with the two-stent strategies [126]. Comparing the two-stent methods, CUL and CRU were found to provide no significant difference in a three year follow-up study, with major adverse cardiac events occurring in 16.7% and 20.6% of patients, respectively [127]. The brief clinical results presented here demonstrate that clinical studies to date have been unable to provide conclusive evidence as to which stent technique performs best. For clinical trials, it is often impossible to differentiate adverse outcomes arising from the stent implantation techniques over all other clinical explanations. Additionally, since PSB is the preferred method, two-stent strategies are generally used only in more critical cases, thus biasing clinical results towards PSB.

In the present study, we sought to compare the hemodynamic conditions associated with *in vitro* testing of different stent implantation techniques. This investigation expands upon the

earlier work by Raben et al. [128] who reported the first *in vitro* experimental results for the hemodynamics of stented coronary bifurcations using steady flow conditions. Here, we use particle image velocimetry (PIV) to obtain velocity and pressure fields under physiological pulsatile flow conditions for each coronary stent implantation technique.

5.3   Materials and Methods

5.3.1   Flow Loop

A mock circulatory flow loop was designed to simulate coronary flow conditions (refer to Charonko et al. [48] for more details). The working fluid, a 60/40 water to glycerin mixture, was used to match the kinematic viscosity and density of blood ($\nu = 3.77 \times 10^{-6}$ m^2/s, $\rho = 1100$ kg/m^3). Figure 5-1a illustrates the flow loop schematic. A pulsatile waveform, shown in Figure 5-1b, was generated through the flow loop using a computer-controlled gear pump. The mean flow rate was maintained around 85 mL/min for all test cases, modeling a resting flow condition with a heart rate of 60 bpm [129]. The flow rate was maintained at an 84/16 split between the MV and SB to ensure that the observed velocity and momentum changes between test cases were an artifact of
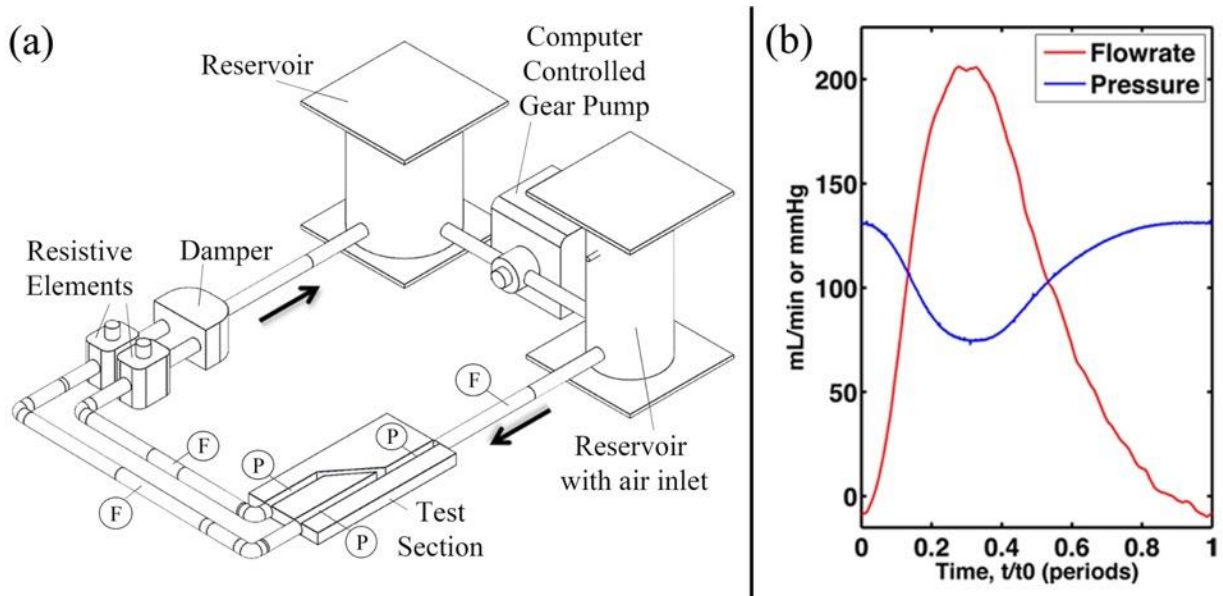
Figure 0-1: (a) Mock coronary flow loop schematic. F and P indicate relative locations of flowmeter probes and pressure transducers, respectively. Arrows indicate flow direction. (Adapted from Raben et al. [128]), (b) Flow rate and pressure waveforms at the inlet of the test section. The time is non-dimensionalized by the duration of one pulse, t0.

the stents and not the inflow conditions [128]. Repeatability of the flow loop was estimated at 2% variation between test cases and cycle-to-cycle variation was within 0.5%. The Reynolds number defined by the lumen diameter before stenting and the average bulk flow velocity was 150. At peak systole it ranged up to approximately 450. The Womersley number was 2.04. These represent physiologically consistent conditions. The pressure waveform, shown in Figure 5-1b, was out of phase with the flow rate, mimicking the hemodynamic environment in the coronary artery. Physiologically, the coronary artery is located on the curved heart and the inlet flow profile may not be fully developed. However, because the physiological inlet velocity profile depends on patient specific parameters and a planar model was used for this study, an experimental replication of this could introduce more error than a fully developed flow profile. Thus, a fully developed inlet velocity profile was used.

5.3.2   Bifurcation Models and Stents

Four compliant coronary artery models with a $60_\circ$ bifurcation were cast using polydimethylsiloxane (PDMS – Sylgard 184), as described by Raben et al. [128]. A $60_\circ$ bifurcation was chosen because it represents a higher risk angle ($\geq 50_\circ$) and thus an angle where complex stenting strategies would more likely be considered clinically [130]. The modulus of elasticity of the models was approximately 1.0 MPa [131]. To minimize geometric and compliance variations across all models, only those with uniform wall thickness (0.4 mm) and no bubble defects were used for this study [128]. Repeatability analysis of this fabrication process has shown geometric variations to be within 1%. The lumen diameters of the MV and SB were 3.96 mm and 2.77 mm, respectively, representing typical coronary diameters [118]. The models used for this study were planar with no curvature and constant lumen diameter, both differing from physiological conditions.   Commercially available Endeavor Resolute stents (Medtronic, Minneapolis, MN, USA) were implanted into three of the models by an interventional cardiologist using a 4.0 mm and 3.0 mm angioplasty balloon for the MV and SB, respectively, as they would be during a typical clinical procedure. The Endeavor stent is a well-established clinical device and was used in all bifurcation models so that the results of this study are not subject to the stent type.

Table 5-1 describes the implantation sequence used for each method.

Table 0-1: Step by step sequence of each stent implantation method used (FKB = Final Kissing Balloon, POT = Proximal Optimization Technique)

PSB	CUL	CRU
1. MV stent implantation 2. POT (MV post-dilation) 3. FKB 4. POT (MV post-dilation)	1. Stent implantation from SB to PMV 2. POT (MV post-dilation) 3. MV rewiring 4. MV Dilation 5. MV stent implantation (distal to proximal) 6. SB rewiring 7. FKB 8. POT (MV post-dilation)	1. SB stenting with small protrusion in MV 2. SB stenting crush by MV balloon inflation 3. MV stent implantation 4. SB rewiring 5. FKB 6. POT (MV post-dilation)

Post stenting lumen diameters were approximately 4.35 mm and 3.05 mm in the MV and SB, respectively. This represents a 110% inflation, as is clinically typical. A similar expansion was observed in the SB with PSB where the final kissing balloon was used, but only near the carina. Figure 5-2 shows the stent models used in this experiment with a schematic of each implementation method tested.
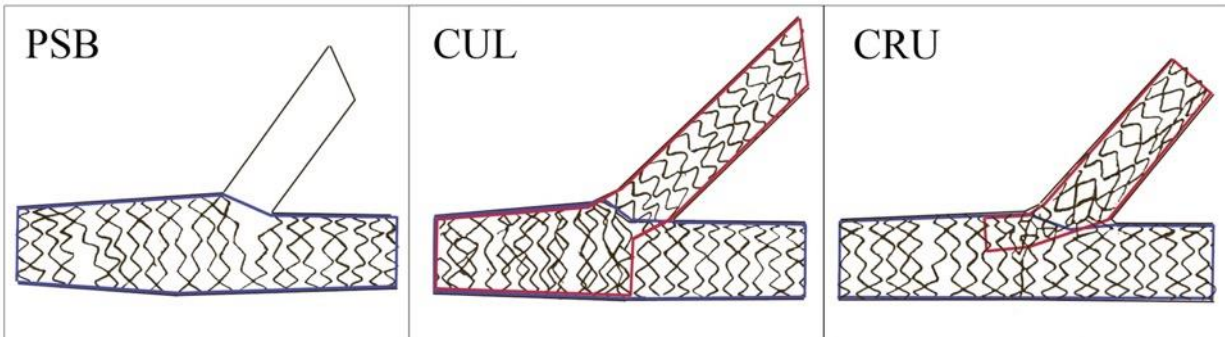
Figure 0-2: Provisional side branch (PSB), culotte (CUL), and crush (CRU) stented models. MV stents are outlined with blue, SB stents are outlined in red. (Adapted from Raben et al. [128])

5.3.3 PIV Setup

PIV images were captured using an Nd-YAG laser and a high-speed camera (IDT Xs-5i) [128]. To match the index of refraction, the area surrounding the test section was also filled with the working fluid. The working fluid was seeded with 7 μm fluorescent particles. A frame pair frequency of 250 Hz was used with 200 μs between the images in a pair. The images were captured

in the transversal plane of the vessel, of size 1728 x 2352 pixels, with a resolution of 7.04 μm/pixel for all stented cases and 7.73 μm/pixel for the un-stented case. Four cardiac cycles were acquired for each test case. PIV images were processed using an in-house PIV software Prana (https://github.com/aether-lab/prana). A multi-frame approach for dynamic range enhancement [132] and robust phase correlation algorithms for increased accuracy were used [73–75]. Four PIV passes were used, with the final pass using a 64 x 32 pixel window and 16 x 16 grid resolution. Proper orthogonal decomposition with a 90% energy cutoff was used on the time-resolved PIV velocity fields to reduce the effects of random errors [51]. To obtain a general quantification of the velocity uncertainty, the peak to peak ratio was analyzed, similar to the method described in Raben et al. [133], with further details in Charonko et al. [78]. From this analysis, uncertainty in the PIV velocity fields is approximated at 4% and 13% for the un-stented and stented cases, respectively. The un-stented case maintained the average uncertainty expected for a typical PIV study. The uncertainty in the stented cases was slightly higher than average due to the inherent issue of stent struts blocking particle motions in the images. A more rigorous uncertainty quantification for this experimental setup was done in Raben et al. [128], but such analysis is beyond the scope of this work.

5.3.4   Post-Processing

The PIV velocity fields were phase averaged. Masks of the stent locations were created using a connected components algorithm with 4-point neighborhoods and a 10-pixel threshold (refer to Sklansky [134] for more details on connected components algorithms). The location of the stent was computed in 25 image increments ($1/20_{th}$ of the pulsatile cycle) to account for the stretching and compressing of the stent through the pulsatile cycle. Velocity components that overlapped with stent struts were excluded from all post-processing calculations.

Particles near the vessel inlet in the proximal main vessel (PMV) for all stented case were observed to be out of focus, hindering the velocity correlation in this region. Consequently, velocities at the inlet of the geometry could not be resolved, as evident in the velocity fields shown in Figure 5-3. For this reason, we have removed this poorly resolved portion of the flow from all post-processing calculations.

Reduction of the centerline velocity was computed as the percent decrease in maximum centerline velocity magnitude for each stent case as compared to the un-stented case. The percent

of vectors in the MV of a given velocity field that are within 50% of the maximum velocity vector in the MV for that velocity field was computed as a representative measure of the breadth of the velocity profile distribution through time. This was also computed for the SB. Because a planar model was used, secondary flows are expected to be minimal throughout the vessel allowing these two metrics—the reduction of centerline velocity magnitude and the percent of vectors within 50% of the maximum velocity magnitude—to together provide a representative measure of momentum deficit induced by the stents.

Recirculating flow areas were identified by the angle of a velocity vector compared to a 0_o and 60_o reference angle in the MV and SB, respectively. Any vector that deviated by more than 20_o from its reference angle was considered an indicator of recirculating flow. The deviation angle of 20_o was chosen because it is small enough that recirculating flow could be easily identified, but large enough that vector angles caused by PIV processing uncertainty or error would not contaminate the calculation. Degree of recirculation was defined as the number of instantaneous velocity fields in which a vector was identified as maintaining recirculating flow, over the total number of velocity fields (250 fields per cycle) in the data set. Thus, one indicates the flow at that point is recirculating throughout the entire cycle while zero indicates flow in that region is never recirculating. Because this study used planar PIV, secondary flows, such as helical structures, are not captured in the velocity fields, allowing for only planar recirculating areas to be identified using this calculation. Recirculation areas identified at the ostium of the SB were removed, since the velocity angle at that location should not abide by the 0_o or 60_o reference angle.

Time averaged WSS (TAWSS), oscillatory shear index (OSI) and relative residence time (RRT), given in Equations (5.1), (5.2), and (5.3) respectively, were computed in the MV.

$$TAWSS = \frac{1}{T} \int_0^T |\tau_w| dt \qquad \text{(Equation 5.1)}$$

$$OSI = \frac{1}{2}\left(1 - \frac{\frac{1}{T}\left|\int_0^T \tau_w dt\right|}{\frac{1}{T}\int_0^T |\tau_w| dt}\right) \qquad \text{(Equation 5.2)}$$

$$RRT = \frac{1}{(1-2OSI)TAWSS} \qquad \text{(Equation 5.3)}$$

where τ_w is the WSS vector and T is the duration of the cardiac cycle. To compute TAWSS, walls of the MV and SB in the test section were linearly defined and velocity gradients were obtained using thin-plate spline radial-basis functions (TPS-RBF) to decrease errors in the calculation [51]. It should be noted that the velocity fields are two-dimensional and thus the TAWSS computed here

is one-dimensional. Additionally, a temporal moving average using four data points was used to smooth the trends and minimize noise caused by the numerical differentiation. The TAWSS code was validated using synthetic Poiseuille flow images. OSI values range from 0 to 0.5 with 0 indicating a flow with no oscillatory flow and 0.5 indicating a purely oscillatory flow. Time and space averaged WSS, OSI, and RRT values were obtained by numerically averaging the spatially varying results from Equations (5.1), (5.2), and (5.3).

PIV pressure fields for each stented case were evaluated using an in-house Navier-Stokes pressure solver described in Charonko et al. [50]. This method has been extensively tested and applied to a variety of flows including cardiovascular applications [55]. The velocity fields following proper orthogonal decomposition (70% energy), prior to phase averaging, were used to compute the pressure in order to minimize errors. A pressure transducer just upstream of the geometry was used as the reference pressure for the code. The method has shown to be accurate for flows with out of plane velocity components of less than 45o [50]. Because a co-planar geometry was used for this study, out of plane motion and thus errors in the computed pressure caused by 3-D effects is expected to be minimal.

Subsequently pressure wave speeds 'c', as a representative measure of the stent compliance, were computed in the distal main vessel (DMV) and the SB using the following equation:

$$c = \frac{1}{\rho} \sqrt{\frac{\sum_{t=0}^{T} dP^2}{\sum_{t=0}^{T} dU^2}} \qquad \text{(Equation 5.4)}$$

where ρ is the fluid density, T is the duration of one cardiac cycle, and P and U are the instantaneous pressure and velocity, respectively [135]. This pressure-velocity single point technique sums the temporal changes of the instantaneous velocity and pressure. The wave speeds in the DMV and SB reported here are the median values of all points in the DMV beginning immediately after the bifurcation and all points in the SB beginning at the carina, respectively. Although Equation (5.4) was derived to mathematically include wave reflections and reduce their effect on the calculation of wave speed [135], the pressure-velocity method has been shown to be susceptible to wave reflections causing an over prediction of the wave speed [136]. Because the magnitudes of the forward and total pressure wave speeds are within the 2% repeatability of the loop and the stents themselves induce negligible effects on the reflected pressure wave [137], bias errors in the computed pressure wave speeds are also expected to be within 2% variability across cases. Thus, changes in the pressure wave speeds between cases can be made here. However,

because the accuracy of the method in this *in vitro* setting has not been rigorously established, pressure wave speeds reported here do not represent global values for pressure wave speeds through a coronary artery and cannot be compared with *in vivo* measurements. Uncertainties in the wave speed calculations were estimated using a Taylor series expansion propagating the effects of density, velocity, and pressure uncertainties. An increase in pressure wave speed following stent implantation indicates a decrease in compliance and thus a larger compliance mismatch. Compliance mismatch is known to increase RRT, adversely alter the WSS distribution, and increase the risk of stenting failure [123].

5.4 Results

Table 5-2 provides a concise summary of all results presented here. This includes, reduction of centerline velocity, representative momentum deficit, TAWSS, OSI, RRT, and pressure wave speed. Stent induced hemodynamic percent changes are also given.
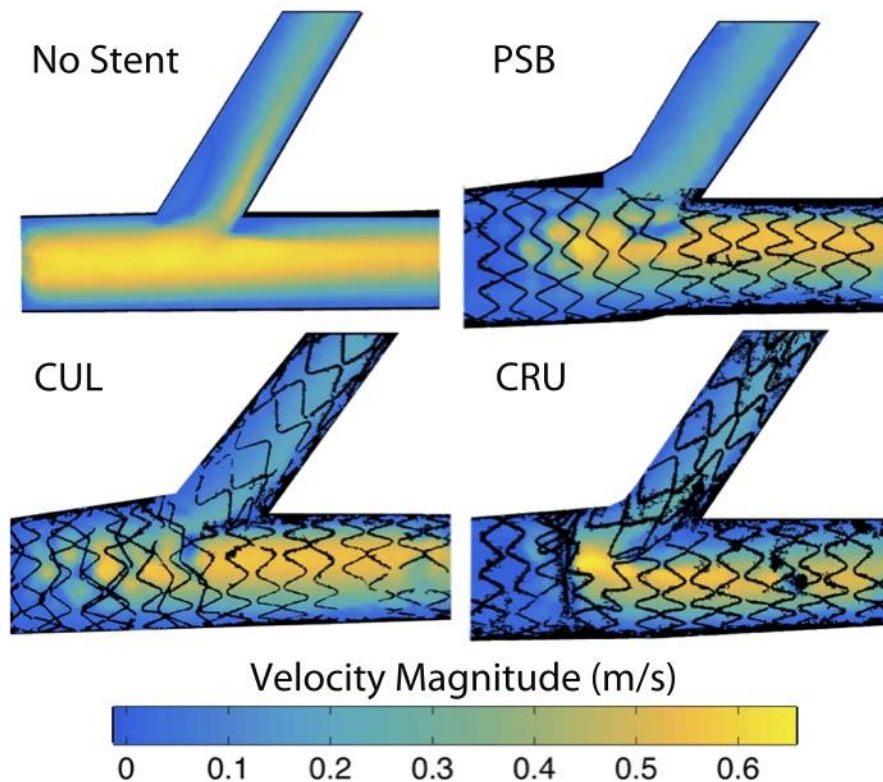
Figure 0-3: Velocity magnitude of each test case at peak velocity magnitude. The low velocity observed in the entrance of the main vessel for all stented cases illustrates the portion of out of focus particles. This portion was omitted for all post-processing calculations.

Table 0-2: Results summary containing velocity, flow parameters, and wave speeds for each test case. Stent induced hemodynamic alterations are defined as the percent change of a property in the stented case compared to the un-stented case.

	Flow Property	No Stent	PSB	CUL	CRU
Velocity Data	MV max velocity magnitude (m/s)	0.683	0.576	0.557	0.634
	SB max velocity magnitude (m/s)	0.509	0.285	0.212	0.253
	TA MV velocity vectors within 50% of max (%)	55.3%	25.4%	29.4%	25.3%
	TA SB vel. vectors within 50% of max (%)	13.5%	24.7%	18.3%	13.9%
Time and Space Averaged Flow Parameters	PMV - WSS (dyne/cm2)	5.46	2.13	2.02	2.66
	PMV - OSI	0.036	0.205	0.053	0.077
	PMV - RRT (dyne/cm2)-1	0.22	1.41	0.68	0.47
	DMV - WSS (dyne/cm2)	4.40	4.16	5.65	3.80
	DMV - OSI	0.025	0.033	0.017	0.019
	DMV - RRT (dyne/cm2)-1	0.288	0.329	0.226	0.304
	Total - WSS (dyne/cm2)	4.82	3.31	4.00	3.12
	Total - OSI	0.029	0.114	0.032	0.025
	Total - RRT (dyne/cm2)-1	0.26	1.05	0.48	0.63
Pressure Wave Speeds	DMV (m/s)	5.5 ± 0.3	14.2 ± 0.6	11.5 ± 0.6	8.5 ± 0.3
	SB (m/s)	7.1 ± 0.5	29.4 ± 1.2	30.8 ± 1.5	19.7 ± 1.0
Stent Induced Flow Changes	MV centerline vel. reduction (%)	-	15.8%	18.5%	7.2%
	SB centerline vel. reduction (%)	-	43.9%	58.4%	50.2%
	WSS deficit (%)	-	31.4%	17.1%	35.3%
	OSI increase (%)	-	293.8%	10.2%	-15.3%
	RRT increase (%)	-	305.0%	84.7%	143.8%
	Pressure wave speed (DMV) increase (%)	-	158.2%	109.1%	54.6%
	Pressure wave speed (SB) increase (%)	-	314.1%	333.8%	177.5%

The velocity magnitude fields at peak flow-rate (~200 mL/min) for each test case are shown in Figure 5-3. An immediately observable consequence of stent implantation is the reduction of centerline flow velocity in the DMV. The maximum centerline velocity magnitude through the cycle for the un-stented case was 0.68 m/s (Figure 5-4a). CRU provided the smallest centerline

98
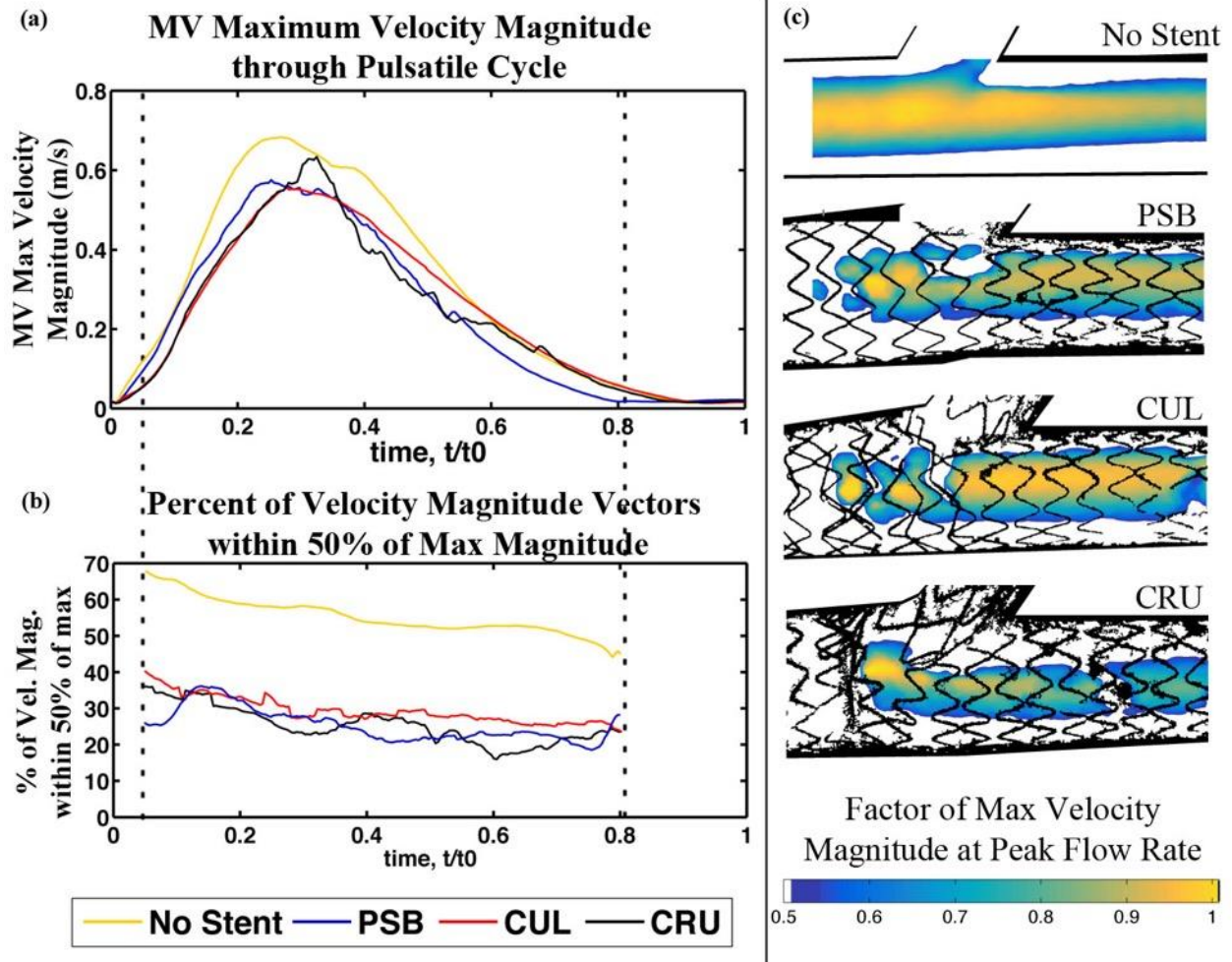
Figure 0-4: (a) Maximum velocity magnitude in MV for each test case through pulsatile cycle, (b) Velocity vectors at a given time in MV that are within 50% of maximum velocity at that time, (c) Normalized velocity vectors in MV at peak velocity magnitude that are within 50% of the maximum velocity vector.

velocity reduction of 7.2%. PSB and CUL yielded similar velocity deficits of 15.7% and 18.4%, respectively. Further, CUL, and to a lesser extent PSB, demonstrate velocity profiles similar to that observed in the un-stented case. CRU altered the velocity profile in the DMV, skewing the centerline velocity towards the non-bifurcating wall.

Figure 5-4 further details the velocity changes in the MV for each stented case as compared to the un-stented case. In Figure 5-4a, the maximum velocity magnitude in each time field through one cycle is plotted. Figure 5-4b plots the percent of the MV velocity vectors at each time step that are within 50% of the maximum velocity magnitude at the given time step. The un-stented case averages 55.3% of vectors within 50% of the maximum velocity, while PSB, CUL, and CRU

maintain averages of 25.4%, 29.4%, and 25.3% of vectors, respectively. Comparing PSB and CUL, they maintain similar maximum velocity magnitude profiles throughout the pulsatile cycle. But, because CUL maintains more vectors within 50% of the maximum velocity throughout the cycle, mathematical integration for a control volume analysis can reasonably be expected to show that CUL yields lower drag than PSB. PSB and CRU seem to have qualitatively similar drag values. The main conclusion is that all stented cases yield a significant momentum deficit in the MV. Figure 5-4c shows the velocity fields at the time where centerline velocity is maximized for each test case normalized by the respective maximum velocity magnitude for each stent and masked to only show vectors within 50% of the maximum. CRU demonstrates a localized jet-like flow in the DMV, suggesting low flow exists near the walls. PSB and CUL exhibit wide velocity fields when the centerline velocity is maximized and thus favorably low velocity profile narrowing in the DMV. PSB maintains an asymmetrical velocity profile, skewed towards the bifurcating wall, in the DMV.

Figure 5-5a shows the reduction of centerline velocity in the SB. The maximum velocity in the SB in the un-stented case is 0.50 m/s. PSB, CUL, and CRU induce a reduction of the maximum SB velocity by 43.9%, 58.4%, and 50.2%, respectively. While all stented cases yield large deficits of velocity magnitude, they produce a broader jet of flow into the SB. Figure 5-5b illustrates this with the percent of SB velocity vectors within 50% of the maximum SB velocity through time. The un-stented case maintains the lowest percentage of vectors with an average of 13.5%. CRU sustains a similar average of vectors of 13.9%. PSB and CUL, however, provide increases with 24.7% and 18.3% percent of vectors within 50% of the maximum velocity, respectively. Using similar analysis as in the MV, CRU provides the largest momentum deficit through the SB. Figure 5-5c shows the SB maximum centerline velocity fields, normalized by the respective maximum velocity for each stent and masked to only show vectors within 50% of the maximum. This further exhibits that all stent methods widen the jet of flow into the base of the SB as compared to the un-stented case. This also suggests that the stents partially mitigate the adverse hemodynamic effects of low velocity and recirculation at the proximal side of the SB caused by the high bifurcation angle.

To confirm the observations that the stented models attenuate the recirculating regions in the SB, Figure 5-6 shows the recirculation areas for each test case. Vectors with recirculating flow for less than 25% of the time were masked out in order to better visualize the regions of interest. Recirculating flow generally can cause low flow velocity, increased OSI and RRT, and higher risk
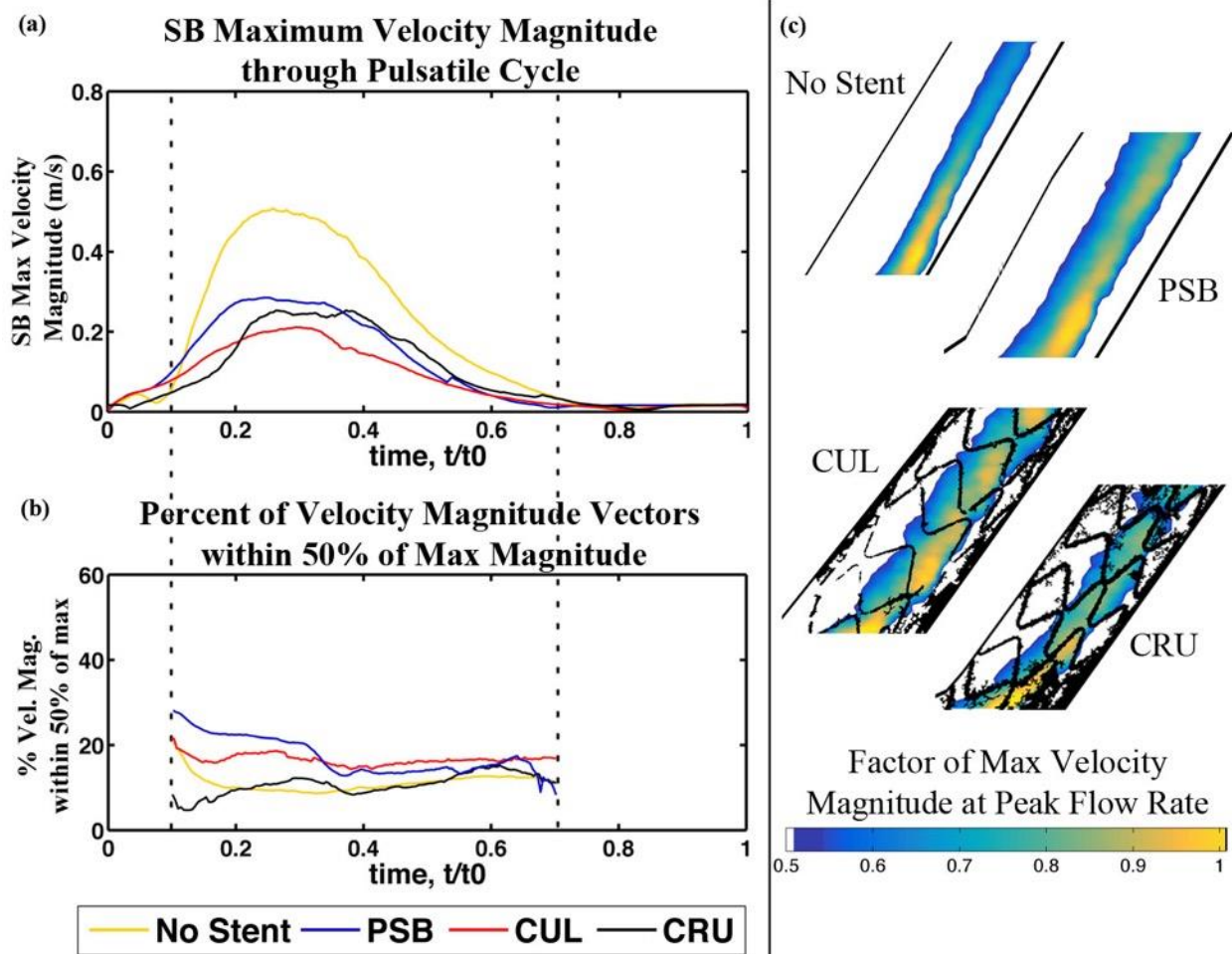
Figure 0-5: (a) Maximum velocity magnitude in SB for each test case through pulsatile cycle, (b) Velocity vectors at a given time in SB that are within 50% of maximum velocity at that time, (c) Normalized velocity vectors in SB at peak velocity magnitude that are within 50% of the maximum velocity vector.

of restenosis. All stent cases eliminate the large recirculation zone observed in the proximal side of the SB base of the un-stented case. The fact that this change, as well as the widening of the SB in-flow jet, is consistent across all implantation types suggests that this positive result may be due to the enlarged ostium of the bifurcation induced by the final kissing balloon procedure. The un-stented case and CRU show low velocity recirculating flow immediately following the SB on the bifurcating DMV wall. CUL shows a smaller and weaker recirculation region in this area. The small recirculating flow regions highlighted on the walls of all test cases are the result of low flow velocity near the walls combined with the unsteady nature of the pulsatility.
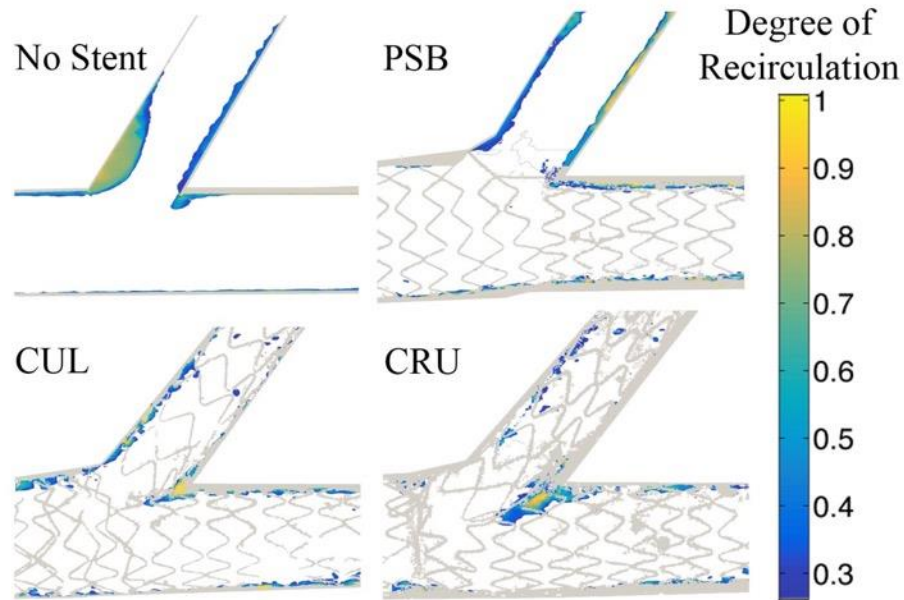
Figure 0-6: Recirculation regions for each test case, where degree of recirculation represents the percentage of time within the pulsatile cycle that the flow deviates by 20_o or more from a reference angle (0_o in the MV or 60_o in the SB). Stent mask is included to show relative locations.

While recirculation zones are generally unfavorable, TAWSS, OSI, and RRT must be examined to determine the adverse risk that each zone causes. Figure 5-7 shows the TAWSS for each case along the MV bifurcating and non-bifurcating wall. In the PMV, the TAWSS is notably low for all stented cases. Previous studies have indicated that low TAWSS in the proximal MV can be the result of over-expansion of the stent, requiring recovery of WSS in order to restore physiological flow conditions [48,128,138]. On the non-bifurcating wall, PSB and the un-stented case show a decreasing TAWSS trend in the DMV, a direct result of the asymmetric velocity profile in this location. Immediately following the SB on the bifurcating MV wall, the un-stented case and CRU both exhibit low TAWSS, a result of the recirculation zones observed in this location. Time and space averaged WSS values are given in Figure 5-8. CUL provided the smallest reduction of time and space averaged WSS of 17.1% as compared to the un-stented case. PSB and CRU yielded reductions of 31.4% and 35.3%. This reduction of overall time and space averaged WSS is due to the hemodynamics in the PMV where all stented methods yielded deficits of over 50%. In the DMV, CUL actually increased the time and space average WSS as compared to the un-stented case by 28.5%, while PSB and CRU maintained mild reductions of 5.5% and 13.6%, respectively.
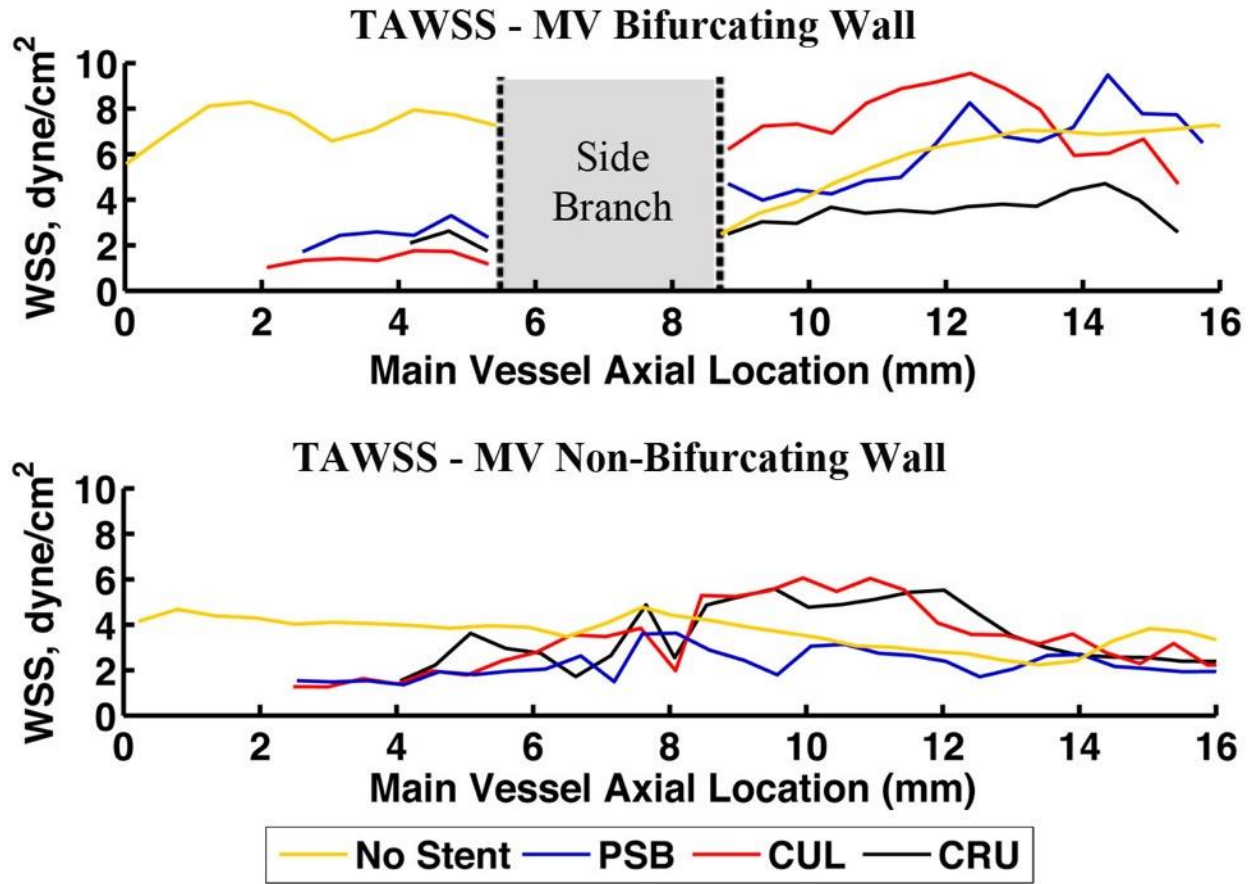
Figure 0-7: Time averaged wall shear stress in the MV for each test case using a four-point moving average to smooth noise from differentiation.

OSI and RRT distributions did not show significant space-dependent trends through the MV and thus are not shown here. Time and space averaged values of OSI and RRT are given in Figure 5-8. In the DMV, CUL and CRU reduce the OSI by approximately 31% and 21%, respectively, as compared to the un-stented case. Meanwhile, PSB increases average OSI in the DMV by 33%, suggesting a detrimental effect of the high bifurcation angle persists with PSB in the DMV. In the PMV, PSB and CRU increase OSI by 473.3% and 115.5%, respectively. CUL maintains a significantly lower OSI increase in the PMV of only 47.3%. All stent cases increase the RRT of the vessel. Particularly, in the PMV as compared to the un-stented case, CUL provides a twofold increase in RRT, while PSB yields a fivefold increase in RRT values. This is likely a consequence of the stent over-expansion and low TAWSS at this location. In the DMV, all stented cases maintain similar RRT results to the un-stented case.
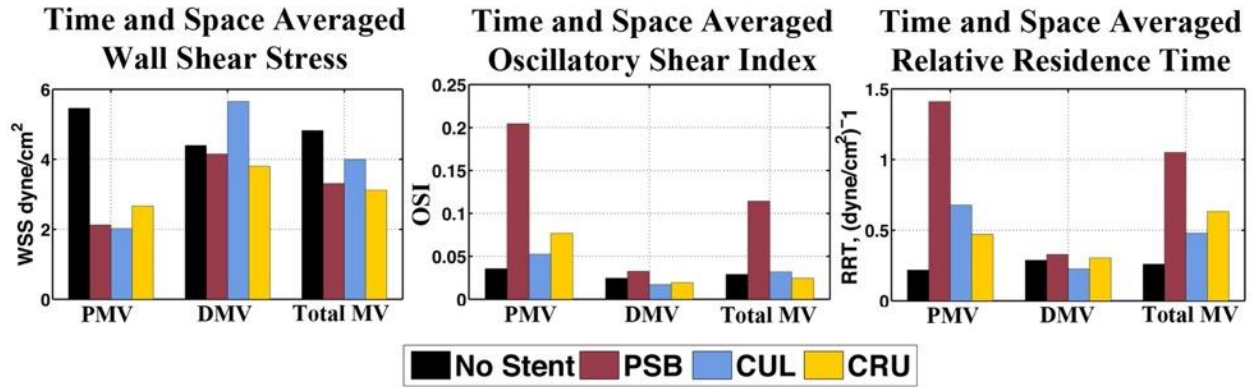
Figure 0-8: Time and space averaged wall shear stress, oscillatory shear index, and relative residence time in the Proximal MV, Distal MV, and MV.

Table 5-2 reports the pressure wave speeds in the DMV and SB for each case, as well as the uncertainty in each calculation. As expected, the implantation of the stent stiffens the vessel, thus increasing the pressure wave speed. CRU best approximates the un-stented vessel compliance for both the DMV and SB. CRU increases the pressure wave speed in the DMV by 54.6% while PSB and CUL yield increases of 158.2% and 109.1%, respectively. Thus, in the DMV, CUL provides increased performance as compared to PSB. In the SB, CUL and PSB are within the uncertainty bounds of the calculation and thus are considered equivalent. PSB increases pressure wave speed in the SB by 314.1% despite not having a stent implanted in the SB. In principle, an alteration in pressure wave speed indicates a change in vessel wall properties. In the case of the PSB, the only alteration to the SB vessel wall could have come from the final kissing balloon technique. Thus, this suggests that the kissing balloon technique can alter a vessel's material properties and adversely contribute to a compliance mismatch.

5.5 Discussion

Coronary branching with bifurcation angles over 50_o are recognized to have higher risk of stenosis as they induce detrimental hemodynamic patterns [130]. In the un-stented case, the high bifurcation angle causes a large recirculation zone in the proximal side at the base of the SB as well as a large centripetal acceleration of the flow pulling it upward which creates a slightly asymmetric velocity profile in the DMV. This causes low velocity flow on the non-bifurcating wall in the DMV and induces low and decreasing TAWSS at this location. Additionally, a low flow region is present on the bifurcating wall of the DMV immediately following the SB, as

observed in Figure 5-6. This causes low TAWSS at the start of the DMV in this location. These hemodynamic observations cultivate three high-risk zones that are susceptible to stenosis: (1) the large recirculating region in the SB, (2) the low flow region near the carina, and (3) the non-bifurcating wall in the DMV. A successful stenting procedure aims to restore normal hemodynamic conditions through a vessel by reopening an occluded vessel. However, cases exhibiting a high bifurcation angle present a unique challenge because "normal hemodynamic conditions", even without a stent, maintain adverse hemodynamic conditions. For this reason, in cases such as the one presented here, where a high bifurcation angle exists, the stent implantation procedure seeks to restore blood flow to normal hemodynamic conditions while also mitigating the natural and deleterious effects of the high bifurcation angle. From the results presented here, it is evident that each stent implantation method achieves these two goals with varying success, as each technique produces different hemodynamic environments.

All stenting methods are able to eliminate the large recirculation zone observed in the proximal side of the base of the SB in the un-stented case. As previously mentioned, the final kissing balloon procedure widens the ostium of the bifurcation, yielding a more gradual transition from the PMV to the SB. For both PSB and CUL, because the recirculation region in the SB is eliminated with all stenting methods, the effective area of flow into the SB is increased, in accordance with Figure 5-5b. Thus, to maintain continuity, the velocity magnitude at the ostium of the SB must decrease, as observed in Figure 5-5a. With CRU, despite the reduction of maximum velocity into the SB at peak velocity magnitude, a high momentum deficit persists in the SB because CRU has a high strut density in the PMV on the bifurcating wall just before the SB.

Because of the low flow velocity and unsteadiness in the pulsatile waveform, small eddies are produced near the wall when the bulk flow velocity is low as evident by the recirculation regions indicated along the walls of all test cases and the carina region in the un-stented case, as seen in Figure 5-6. However, in the case of CRU, the recirculation zone near the carina is an artifact of high strut density and interaction at that location, resulting in flow disturbances. Subsequently, with CRU, the TAWSS drops following the SB and must increase throughout the length of the DMV non-bifurcating wall in order to restore the flow conditions following the strut induced flow disturbances. CUL also shows a low flow region near the carina, though considerably smaller than with CRU. This is because CUL maintains overlapped struts at this location, but the two stents have a more limited interaction than with CRU. Additionally, CUL does not cause low TAWSS to

persist for any length on the bifurcating wall in the DMV as evident in Figure 5-7, indicating that the low flow area maintains minimal hemodynamic disturbances. PSB does not show a low velocity flow region at the carina level, in accordance with previous computational fluid dynamics (CFD) results [128,138,139]

Having a DMV velocity profile very similar to that of the un-stented case, CUL best maintains a normal velocity profile in the DMV. PSB was previously noted to maintain an asymmetric velocity profile in the DMV. PSB appears to have the largest momentum flux through the SB of all stenting cases. Thus, it maintains the strongest centripetal force on the flow, yielding a larger upward force on flow in the DMV and a velocity profile more skewed towards the bifurcating wall. This results in low flow velocity and TAWSS on the non-bifurcating wall.

To the authors' knowledge, this is the first study to examine compliance mismatch to compare coronary bifurcation stent implantation techniques. Further, examination of the pressure wave speeds demonstrates that the stenting methods stiffen the vessels to varying extents and thus can induce different levels of a compliance mismatch. CRU advantageously provided the smallest compliance mismatch throughout the vessel. Adversely, PSB provided the largest decrease in compliance of the MV. This likely contributes to the increase of OSI and RRT values seen with PSB in Figure 5-8, supporting the notion that compliance mismatch substantially affects the level of flow disturbances induced [123]. As previously mentioned, the change in pressure wave speed in the SB with PSB indicates that the kissing balloon method can also induce a compliance mismatch. The fact that PSB and CUL had similar pressure wave speeds in the SB may lead to two conclusions. First, because the final kissing balloon technique seemed to have a bigger affect in the SB than the MV in terms of compliance mismatch, it likely has a more deleterious effect on smaller lumen diameter vessels. Second, because the kissing balloon was also used with CRU, where a lower compliance mismatch was observed in the SB, the crushing of the SB stent could plausibly restrict the expansion of the kissing balloon in the SB, thus minimizing the stiffening of the vessel. The second conclusion could also be drawn for the MV kissing balloon, thus indicating that the crushed portion of the SB stent provides benefits in terms of kissing balloon induced vessel stiffening and compliance mismatch.

In vivo, the observed stent induced flow disturbances would each affect vascular remodeling and intimal growth. A known link between low TAWSS and neointimal hyperplasia exists [120,121]. This would be of concern with PSB maintaining the low TAWSS distribution on

the non-bifurcating wall of the MV. Additionally, because PSB maintains a large increase in OSI and RRT in the PMV, it would promote endothelial cell inflammation, vascular remodeling, and ultimately restenosis at that location [119]. CRU demonstrated several adverse effects of high strut density and close strut interactions, a factor known to elevate neointimal hyperplasia [121]. A large compliance mismatch is known to cause restenosis, but can also affect platelet behavior and increase the risk of thrombosis [123]. The results of this study supported the idea that compliance mismatch plays a crucial role in the level of flow disturbances induced, particularly in TAWSS, OSI, and RRT distributions. This, coupled with the fact that these flow disturbances affect biomechanical processes, may indicate that compliance mismatch is an influential distinguishing factor among stent implantation techniques and should be explored in future technique developments.

Overall, this study demonstrated both positive and negative hemodynamic effects observed with all implantation methods. CRU provided some advantages, most notably the lowest compliance mismatch. However, CRU demonstrated the lowest TAWSS, an adverse jet-like velocity profile in the DMV, and deleterious interaction of the two stents resulting in high flow disturbances in the MV near the carina. Despite its simplicity, PSB showed several favorable hemodynamic results including the elimination of major recirculation zones and widening of the SB inflow jet. However, PSB yielded the highest and most adverse OSI and RRT averages and MV compliance mismatch. Meanwhile, CUL provided a balanced hemodynamic environment that eliminated the adverse effects of the high bifurcation angle and showed many indications of maintaining normal flow conditions. CUL yielded time and space averaged WSS, OSI, and RRT values that most closely matched that of the un-stented case. Overall, CUL provided the most synergistic stenting solution, resulting in minimal stent induced flow disturbances. Additionally, disruptions of the flow that were observed with CUL did not propagate into TAWSS, OSI, or RRT. Thus, these results demonstrated that both PSB and CUL were able to retain many aspects of normal flow conditions with minimal flow disturbances. However, CUL mitigated the detrimental effects induced by a high bifurcation angle, while PSB fell short.

There were some notable limitations of this study. The calculation of WSS, OSI, and RRT on the walls of the SB was subject to experimental noise and stent interference. All TAWSS computations were also subject to small disturbances as a result of stent struts inducing minor directional deviations from the defined walls. Additionally, the results presented here are

constrained to one plane of the bifurcation, making overall distributions of TAWSS, OSI, and RRT unknown. The results also do not account for factors such as overlapping stent struts that increase risk of mechanical stent failure [140]. Because properties of diseased coronary arteries vary spatially and are highly patient specific, compliance of the models used for this study approximated properties of a healthy coronary artery. Thus, the pressure wave speed calculations here show representative compliance mismatch between a healthy vessel and an implanted stent. It is possible an *in vivo* diseased coronary artery plastically deforms differently than the *in vitro* silicone models used here which may alter the magnitude of the increase in pressure wave speed observed. Therefore, while the results presented indicate the major hemodynamic differences between the stent implantation methods, final conclusions and comparisons between the stent cases must be taken with caution, as the experimental limitations impose an inability to directly predict clinical outcomes.

5.6   Acknowledgements

CHAPTER 6. MULTI-MODALITY CEREBRAL ANEURYSM HEMODYNAMIC ANALYSIS: *IN VIVO* 4D FLOW MRI, *IN VITRO* VOLUMETRIC PARTICLE VELOCIMETRY, AND *IN SILICO* COMPUTATIONAL FLUID DYNAMICS

6.1 Abstract

Typical approaches to patient-specific hemodynamic studies of cerebral aneurysms use image-based computational fluid dynamics (CFD) and seek to statistically correlate parameters such as wall shear stress (WSS) and oscillatory shear index (OSI) to risk of growth and rupture. However, such studies have reported contradictory results, emphasizing the need for in-depth multi-modality hemodynamic metric evaluation. In this work, we used *in vivo* 4D Flow MRI data to inform *in vitro* particle velocimetry and CFD modalities in two patient-specific cerebral aneurysm models (basilar tip and internal carotid artery). Pulsatile volumetric particle velocimetry experiments were conducted, and the particle images processed using Shake-the-Box (STB), a particle tracking method. Across modalities, distributions of normalized WSS and relative residence time (RRT) were shown to be highly yet inconsistently affected by minor flow field and spatial resolution variations across modalities, and specific relationships among these should be explored in future work. Conversely, OSI, a non-dimensional parameter, was shown to be more robust to the varying assumptions, limitations, and spatial resolutions of each subject and modality. These results suggest a need for further multi-modality analysis as well as development of non-dimensional hemodynamic parameters and correlation of such metrics to aneurysm risk of growth and rupture.

6.2 Introduction

It is estimated that about 3% of the population harbors an unruptured intracranial aneurysm (IA) [141]. If detected, clinicians must assess and balance risk of rupture with risk of treatment of the cerebral aneurysm [1,142]. However, accurately assessing risk of rupture in IAs is difficult as the specific mechanisms that cause an aneurysm to form, grow, and rupture remain largely unknown.

Previous studies have demonstrated that hemodynamics play a critical role in the growth and rupture of an IA [3,6,15,19,143]. However, despite a large volume of studies that have investigated the influence of several hemodynamic variables on risk of rupture, contradictory and ultimately inconclusive results have been reported. Wall shear stress (WSS) has received much attention, but has been perhaps the most controversial hemodynamic parameter [3]. Both low [6,11,16,20,144] and high [13,25] WSS have been shown to indicate elevated risk of rupture. High WSS gradients, high oscillatory shear index (OSI), and high relative residence time (RRT) have also been reported to increase risk of rupture [3,6,12,20]. Studies have also explored the presence and effect of chaotic flow and high frequency fluctuations in cerebral aneurysms [9,19,142]. Other hemodynamic variables identified as potentially increasing risk of rupture include concentrated inflow jets, larger shear concentration, lower viscous dissipation, and complex and unstable flow patterns [13,19,25].

Computational fluid dynamics (CFD) has been the predominant methodology used to study hemodynamics in cerebral aneurysms [1,6,9,11,13,16]. However, limited CFD validation and disputed CFD assumptions such as laminar flow remain issues limiting its clinical acceptance [22]. It has also been shown that CFD results can vary significantly based on solver parameters, even when similar geometries and boundary conditions are used [15,21]. Velocity fields obtained from both *in vivo* and *in vitro* 4D Flow MRI have also been used, but the low spatiotemporal resolution is a major limitation of this modality [15–17]. Although high resolution 4D Flow MRI has been shown to capture complex flow patterns [17], studies have demonstrated that the low resolution causes an underestimation of velocity and WSS magnitudes, particularly when compared to CFD or PIV [1,15,16,145]. Few experimental particle image velocimetry (PIV) studies have been conducted in this domain. Among such studies, planar and stereo PIV (2D-2 velocity component) have been most common [12,17,20,142,146]. Other studies have taken 2D data at several parallel planes in a "sliced planar" (3D-2 velocity component) configuration and subsequently reconstructed the third velocity component [19,147]. Despite the high three-dimensionality known

to exist in cerebral aneurysm geometries, to date, only one steady flow 4D tomographic PIV (3D-3 velocity component) study has been reported [15]. Further, PIV studies are most often used only to compare flow patterns and validate CFD models and simulations [15,17,20], only a few have reported WSS and even less (if any) OSI and RRT [12,19]. Multi-modality-type studies have compared *in vivo* 4D Flow MRI and CFD [11,16,22,37], many treating CFD as the "ground-truth" modality due to its increased resolution and accuracy, however the higher physiological fidelity method is debatable. Due to this "ground-truth" concern, studies which directly compared 4D Flow MRI, CFD, and PIV are often restricted to *in vitro* and *in silico* validation-based analysis [15,17,142,147], limiting their clinical translational ability due to the lack of *in vivo* data.

In this work, we utilize a multi-modality approach, including *in vivo* measurements, *in vitro* experiments, and *in silico* modeling in a unique way, where the *in vivo* 4D Flow MRI was used as boundary conditions for the CFD and particle velocimetry. We conducted one of the first reported pulsatile volumetric particle velocimetry studies using two patient-specific aneurysm models. As opposed to traditional tomographic PIV (TOMO-PIV) studies which use interrogation window correlation, we used Shake-the-Box (STB) [87], a particle tracking methodology, which has, to the authors' knowledge, never been used in this domain and demonstrated significant improvements in the current experimental methodologies for this application. All three modalities maintained different assumptions and limitations, and—due to the low spatiotemporal resolution and high noise inherent to 4D Flow MRI—some uncertainty in the prescribed boundary conditions existed which manifested into flow variations across modalities. Here, we investigate the effect of these factors on the resulting hemodynamic metrics including time averaged WSS (TAWSS), OSI, and RRT. The multi-modality approach of this work was intended to take some initial steps towards bridging the gaps between modalities and understanding how to synthesize information by leveraging the strengths of each method and compensating for the weaknesses, thereby enhancing the clinical translational ability of such hemodynamic analysis.

6.3   Materials and Methods

6.3.1   In vivo 4D Flow MRI and MRA Imaging

The two aneurysm models used were a basilar tip aneurysm, MRI imaged at San Francisco VA Medical Center, and an internal carotid artery (ICA) aneurysm, MRI imaged at Northwestern

Memorial Hospital (NMH). Both aneurysms were imaged on a 3T MRI scanner (Skyra, Siemens Healthcare, Erlangen, Germany). At San Francisco VA Medical Center, the Siemens WIP sequence, an ECG-gated RF spoiled 4D Flow MRI sequence was used with gadolinium contrast, while at NMH no contrast was used. The 4D flow scan parameters for both imaging studies are given in Table 6-1. The *in vivo* 4D Flow MRI data will be referred to simply as '4D Flow' herein.

Table 6-1: 4D Flow MRI parameters and resolutions.

Geometry	TE/TR (ms)	Flip Angle (°)	Velocity Encoding (venc) (cm/s)	Temporal Resolution (ms)	Spatial Resolution (mm)
Basilar Tip	3.46/6.33	12	100	40.5	1.25 x 1.25 x 1.33
ICA	2.997/6.4	15	80	44.8	1.09 x 1.09 x 1.30

All 4D Flow data was corrected for noise, velocity aliasing, and phase offset errors caused by eddy currents and concomitant gradient terms. In addition to 4D Flow, contrast-enhanced magnetic resonance angiography (CE-MRA) data with a spatial resolution of 0.7 x 0.7 x 0.7 mm3 for the basilar tip aneurysm and non-contrast time of flight (TOF) angiography with a spatial resolution of 0.4 x 0.4 x 0.6 mm3 for the ICA aneurysm were acquired in the same scanning sessions and used to create the *in vitro* models.

6.3.2 Image Segmentation and Model Fabrication

For the basilar tip aneurysm, CE-MRA images were segmented using an in-house VTK-based software. A 3D iso-surface was computed by selecting a threshold intensity value that defined the intra-luminal volume of the vessel. The threshold was adjusted to match the iso-surface to the MR luminal boundaries. For the ICA aneurysm, TOF images were segmented with open-source ITK-SNAP software, using thresholding and volume growth techniques. A modeling software, Geomagic Design (3D Systems, Rock Hill, SC), was used to separate the inflow and outflow vessels of the aneurysm from the remaining cerebral vasculature (Figures 1a and 1c). The resulting surface (STL), shown in Figures 1b and 1d, was used for CFD simulations and PIV flow phantom fabrication. Note the STL surfaces in Figure 1 are zoomed in and clipped such that they do not reflect the full branch lengths. For the flow phantoms, inlet and outlet vessels were extended in order to connect the model to the flow loop. A positive-space model of the vascular geometry was 3D printed (ProJet printer - 3D Systems), embedded into a tear-resistant silicone block, then
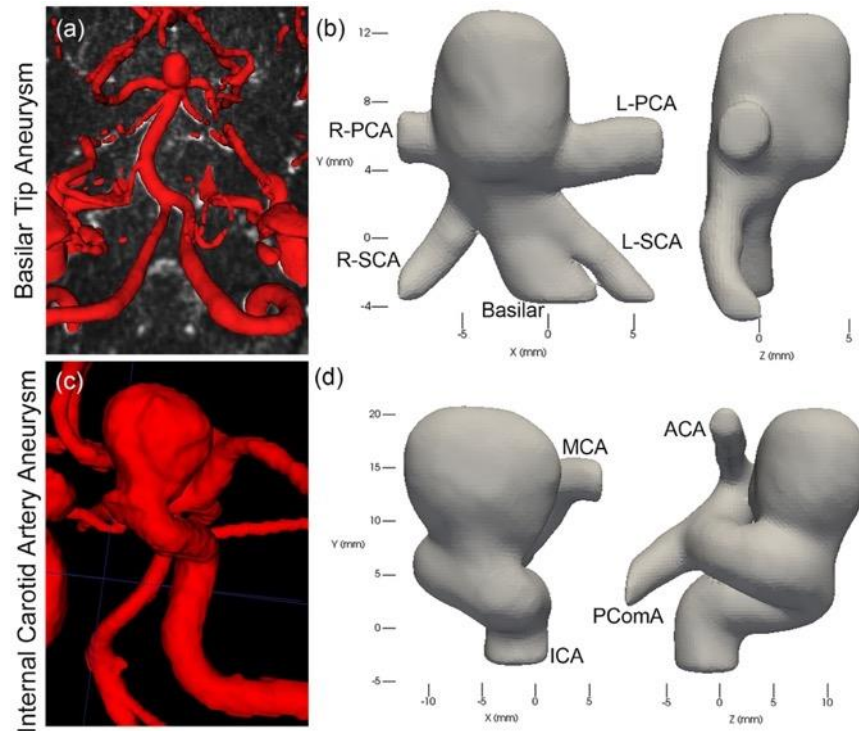
Figure 6-1: Segmentation from (a) in vivo vasculature showing patient-specific basilar tip aneurysm, to the (b) associated in vitro model. Note: The in vitro basilar tip model was mirrored as compared to the in vivo. (c) In vivo vasculature for patient-specific internal carotid artery (ICA) aneurysm and the (d) in vitro segmented model. (PCA=posterior cerebral artery, SCA=superior cerebellar artery, MCA=middle cerebral artery, ACA=anterior cerebral artery, PComA = posterior communicating artery).

cut from the block. A low melting point metal (Cerrobend 158 Bismuth alloy) was cast into the block and the block was then cut away. The metal model was embedded in optically clear polydimethylsiloxane silicone (PDMS—Slygard 184) which was allowed to cure until hardened, then the metal was melted out from the clear PDMS.

6.3.3   *In Vitro* **Flow Loop**

An *in vitro* flow loop (Figure 6-2a) was designed to simulate *in vivo* flow conditions. The working fluids, detailed in Table 6-2, were blood analogs consisting of water, glycerol, and urea. Water, glycerol, and urea blood analogs have been demonstrated to provide good user-control and flexibility over the balance of fluid density, viscosity, and index of refraction, as well as yield densities more consistent with blood than water, glycerol, and sodium iodide (NaI) solutions [148]. The pulsatile inflow waveforms (Figure 6-2b) were extracted from the *in vivo* 4D Flow MRI data

and generated by a computer-controlled gear pump. Average flow rates for the outlet vessels were controlled using resistive elements to match the 4D Flow outlet flow rate ratios. Flow details for both geometries are provided in Table 6-3.

Table 6-2: Blood analog working fluids used for both geometries. Nano-pure water, technical grade glycerol (99% - McMaster-Carr), and 99+% urea (Fischer Scientific) were used.

Geometry	Blood Analog Composition (%wt)			Density (kg/m_3)	Kinematic Viscosity (m_2/s)
	Water	Glycerol	Urea		
Basilar Tip	44.8	32.8	22.4	1103	$3.04x10_{-6}$
ICA	45.3	29.7	25.0	1132	$3.50x10_{-6}$

Table 6-3: Flow cycle information for both aneurysm geometries.

Geometry	Reynolds Number		Womersley Number	Cycle Period, T (sec)
	Max	Min		
Basilar Tip	500	150	2.73	0.77
ICA	300	130	5.33	0.54
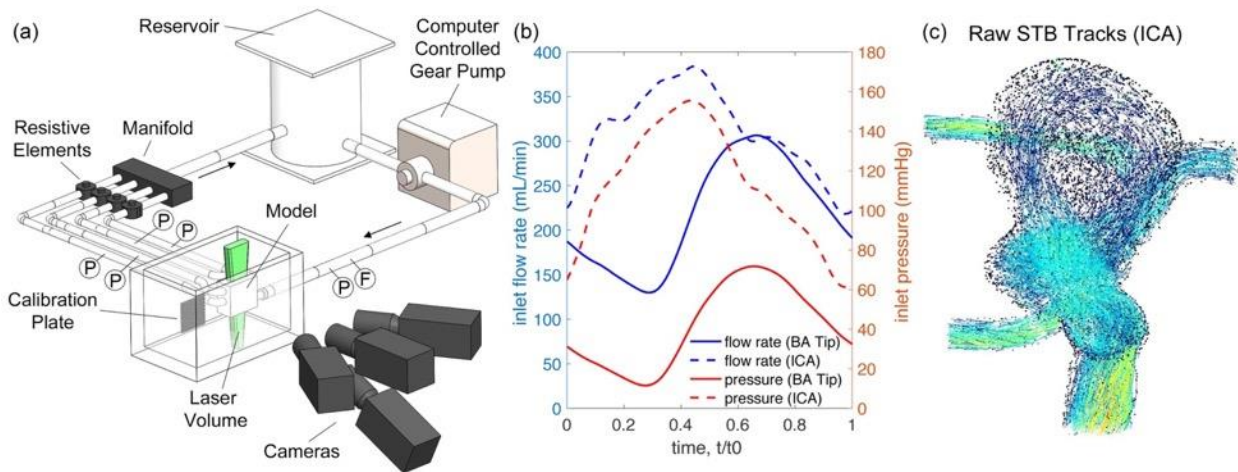
Figure 6-2: (a) Schematic of the flow loop setup, including the camera and calibration plate. F indicates locations of ultrasonic flowmeters and P indicates locations of pressure transducers. (b) Inflow flow rate and pressure taken from the upstream flowmeter and pressure transducer for both geometries. The phase of the pulsatile cycle is displayed as it was extracted from 4D Flow MRI. (c) Sample Shake-the-Box tracks for the ICA geometry.

6.3.4 Volumetric Particle Velocimetry Measurement Technique

Particle images were captured using an Nd-YLF laser (Continuum Terra-PIV, $\lambda = 527$ nm) and four high-speed cameras (Phantom Miro). In the camera configuration (Figure 6-2a), the center camera was not angled, while the other three were angled about 30º from the geometry plane. The magnification of all cameras was approximately 30 µm/pixel. Flow was seeded with 24 µm fluorescent particles and long-pass filters filtered the laser light from the images. The index of refraction of the working fluid was matched to that of the PDMS model (n = 1.4118), and the model was submerged in the working fluid to reduce optical distortion. Time-resolved images (1216x1224 pixels for basilar tip, 1088x1320 pixels for ICA) were captured at 2000 Hz, corresponding to a maximum particle displacement between frames of approximately 10 pixels. Three full pulsatile cycles for the basilar tip aneurysm and four cycles for the ICA aneurysm were captured.

Particle images were processed using DaVis 10.0 (LaVision Inc.). Calibration images were captured using a dual-plane calibration target. The perspective calibration error was approximately 0.25 pix for each camera in both experiments and volume self-calibration corrected these errors to less than 0.03 pix [149]. Shake-the-Box (STB), a particle tracking based algorithm, was used to process the velocity fields. Sample STB tracks are shown in Figure 6-2c. STB requires time-resolved data, using the previous time step to iteratively add predicted particle locations in the next time step. The predicted particle locations are refined by iteratively "shaking" them within a tolerance, minimizing the residual between the subsequent particle image and predicted particle image. STB was done using 12 iterations for both the outer (adding particles) and inner (particle position refinement) loops with an allowed particle triangulation error of 1.5 voxels and particle position shaking of 0.1 voxels. As opposed to planar and stereo PIV [77,78,150], currently no methods to evaluate uncertainty in volumetric PIV/STB processing have been reported. However, the calibration errors were consistent with those observed in well-controlled tomographic PIV experiments. To further ensure accuracy of the STB data, a portion of data was processed using the traditional TOMO-PIV multiplicative algebraic reconstruction technique (MART) processing [151]. Due to the complex, highly curved aneurysm geometries which amplify small and unavoidable refractive index mismatches within the test section, ghost particles (falsely triangulated 3D particles) were expected to be higher using MART. Ghost particles can create significant bias error in resulting velocity fields [87,152]. As compared to MART, STB's use of

temporal information reduced the percentage of estimated ghost particles from about 10% to less than 1%. STB also reduced computation time by at least a factor of 10 per dataset. The volumetric STB data will be referred to as 'STB' herein.

6.3.5 CFD Simulation

CFD simulations were performed using Fluent 18.1 (ANSYS) to solve the governing Navier-Stokes equations. An unstructured tetrahedral mesh was generated on the domain using HyperMesh 14.0 (Altair Engineering, Troy, MI). Incompressible, Newtonian flow with density of $1060\,kg/m_3$ and dynamic viscosity of 0.0035 Pa·s was modeled. Laminar flow and rigid walls were assumed. Patient-specific waveforms obtained from 4D Flow were prescribed at the inlet and outlets of the CFD models. A pressure-based coupled algorithm was used to solve the momentum and pressure-based continuity equations. A second-order Crank–Nicolson scheme was used in time discretization and a third-order MUSCL scheme was used for discretization of the momentum equations. A mesh with the nominal cell size of 150 µm and time step of 1.5 ms was used. These values provided sufficient resolution of the flow based on mesh independence and temporal resolution testing. Three cardiac cycles were simulated, and the results obtained for the last cycle were used for comparisons with the other modalities.

6.3.6 Post-Processing

All modalities were registered to and masked by the STL geometry obtained from MRA segmentation. The unstructured STB and CFD data were gridded to isotropic resolutions of 0.3 and 0.4 mm for the basilar tip and ICA aneurysms, respectively, using inverse-squared radial distance weighted averaging. An initial radius of half the grid size was used to search for the nearest unstructured vectors, however this radius was extended to ensure a minimum of three unstructured vectors for each averaging calculation. For the STB gridding, unstructured velocity fields were temporally grouped at a 5:1 and 3:1 ratio for the basilar tip and ICA aneurysms, respectively, such that each unstructured field was used in only a single group. This increased the number of unstructured particles per gridded time step but reduced the effective temporal resolution to 2.5 ms and 1.5 ms for the basilar tip and ICA aneurysms, respectively. The gridded STB data was filtered using proper orthogonal decomposition (POD) with the entropy line fit (ELF) autonomous thresholding method [41,112]. A single pass of universal outlier detection (UOD) [76]

and phase averaging of the STB pulsatile cycles were subsequently done. "Virtual voxel averaging" was spatially performed to bring the STB and CFD data to the 4D Flow spatial resolution.

Wall shear stress was computed using thin-plate spline radial basis functions (TPS-RBF), which performs smoothing surface fits and reduces errors in the inherently noisy gradient calculation [51]. A normal vector at each surface point was computed by mapping the velocity coordinate to the equivalent STL-surface point and computing the inward facing normal from a surface fit of 25 adjacent STL-surface points. Two passes of UOD were used to eliminate erroneous normal vectors. For the voxel averaged datasets, wall normals were extracted from their full resolution equivalent. For the 4D Flow, the full resolution CFD was used. WSS was computed according to the following equations [153]:

$$\tau_x = \mu * \left(2n_x \left(\frac{du}{dx} \right) + n_y \left(\frac{du}{dy} + \frac{dv}{dx} \right) + n_z \left(\frac{du}{dz} + \frac{dw}{dx} \right) \right) \quad \text{(Equation 6.1)}$$

$$\tau_y = \mu * \left(n_x \left(\frac{du}{dy} + \frac{dv}{dx} \right) + 2n_y \left(\frac{du}{dy} \right) + n_z \left(\frac{dv}{dz} + \frac{dw}{dy} \right) \right) \quad \text{(Equation 6.2)}$$

$$\tau_z = \mu * \left(n_x \left(\frac{du}{dz} + \frac{dw}{dx} \right) + n_y \left(\frac{dv}{dz} + \frac{dw}{dy} \right) + 2n_z \left(\frac{dw}{dz} \right) \right) \quad \text{(Equation 6.3)}$$

$$\tau_{mag} = \sqrt{\tau_x^2 + \tau_y^2 + \tau_z^2} \quad \text{(Equation 6.4)}$$

where τ_x, τ_y, and τ_z, are the WSS components in the x, y, and z directions, τ_{mag} is the WSS magnitude, μ is the dynamic viscosity, and (n_x, n_y, n_z) is the unit normal.

The in-house WSS code, including the wall normal and velocity gradient calculations, was validated using analytical 3D Poiseuille flow data. Biases in the near-wall discrete velocity gradients, whose magnitude vary based on each specific point's distance from the wall, is a known issue [19,51]. Thus, similar to that done in Yagi et al. (2013) [19], the WSS calculation was extended to use gradients beyond the biased near-wall region, mitigating the spatial variation of this bias to about 5% but allowing WSS magnitude bias errors of up to 25% (based on the validation testing). Thus, all WSS magnitudes reported here are expected to have a consistent bias and should be considered only relative to other values reported here.

Time averaged WSS (TAWSS) was computed according to Equation (6.5)

$$TAWSS = \frac{1}{T} \int_0^T |\tau_w| dt \quad \text{(Equation 6.5)}$$

where τ_w is the WSS vector and T is the duration of the pulsatile cycle. Oscillatory shear index (OSI) was subsequently computed according to Equation (6.6)

$$OSI = \frac{1}{2}\left(1 - \frac{\frac{1}{T}\left|\int_0^T \tau_w dt\right|}{\frac{1}{T}\int_0^T |\tau_w| dt}\right).$$
(Equation 6.6)

OSI is a non-dimensional parameter ranging from 0 to 0.5, where 0 indicates no oscillatory WSS throughout the pulsatile cycle and 0.5 indicates purely oscillatory WSS. Relative residence time (RRT) was computed using Equation (6.7).

$$RRT = \frac{1}{(1-2OSI)TAWSS}$$
(Equation 6.7)

RRT is a measure of the flow stagnation or residence of fluid particles near the wall. High RRT is typically considered as an indicator of flow disturbances [154], thrombus-prone regions [155], and flow separation regions which are believed to facilitate aneurysm growth [3].

6.4   Results

6.4.1   Comparing Flow Structures and Velocity Distributions across Modalities
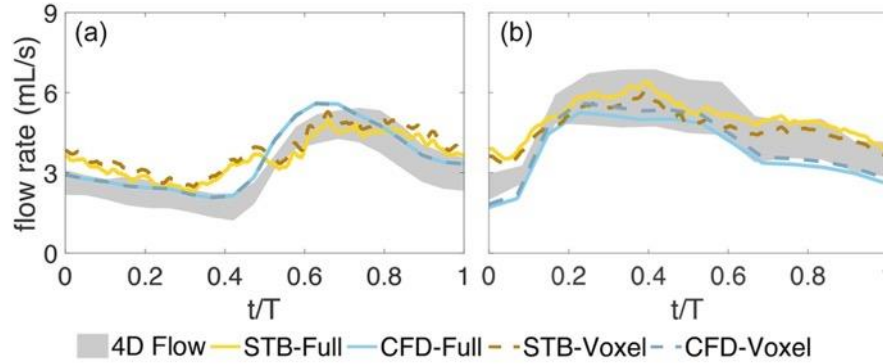
Figure 6-3: Inlet flow rates for all modalities in the (a) basilar tip aneurysm and (b) ICA aneurysm. The 4D Flow flowrate is shaded to show the discrepancy of the total inflow and outflow flow rates.

The inlet flow rate was computed from the velocity fields for all modalities in the basilar tip and ICA aneurysms to ensure agreement across modalities and are shown in Figures 6-3a and 6-3b, respectively. The shaded 4D Flow inflow rates highlight the difference between the computed inflow and outflow rates and demonstrate the uncertainty of prescribed *in vitro* boundary conditions. All reported 4D Flow inflow rates are based on the average of the total inflow and outflow rates. The maximum inlet flow rate in the basilar tip aneurysm was 4.81, 4.97, and 5.61 mL/s for the 4D Flow and full resolution STB and CFD, respectively. The average inlet flow rate was 3.09 mL/s for the 4D Flow, 3.58 mL/s for STB, and 3.51 mL/s for CFD. The trend of the

118

inflow waveforms was similar for all modalities, with STB maintaining the largest temporal variability as expected. For the ICA aneurysm, the maximum inflow rate was 5.81, 6.40, and 5.26 mL/s for the 4D Flow, and full resolution STB and CFD, respectively. The average inlet flow rate was 4.54 mL/s for 4D Flow, 5.07 mL/s for STB, and 3.79 mL/s for CFD. Again, the general inflow waveform trend showed reasonable agreement across all modalities.

Figure 6-4 shows the instantaneous 3D velocity stream-tracers for each modality and geometry at peak systole. In the basilar tip aneurysm (Figure 6-4a), initial observation shows qualitative agreement of the flow patterns across all modalities. Flow enters from the basilar artery and about 20% (by flow rate) exits through the superior cerebellar arteries (SCAs). The remainder of the flow extends into the right distal posterior region of the aneurysmal sac, swirls to the left proximal anterior portion of the sac and exits the posterior cerebral arteries (PCAs). In the ICA aneurysm (Figure 6-4b) flow enters from the curving ICA and some flow rotates through the aneurysmal sac before re-entering the distal ICA. About half of the flow exits through the middle cerebral artery (MCA) and the remainder splits between the anterior cerebral artery (ACA) and
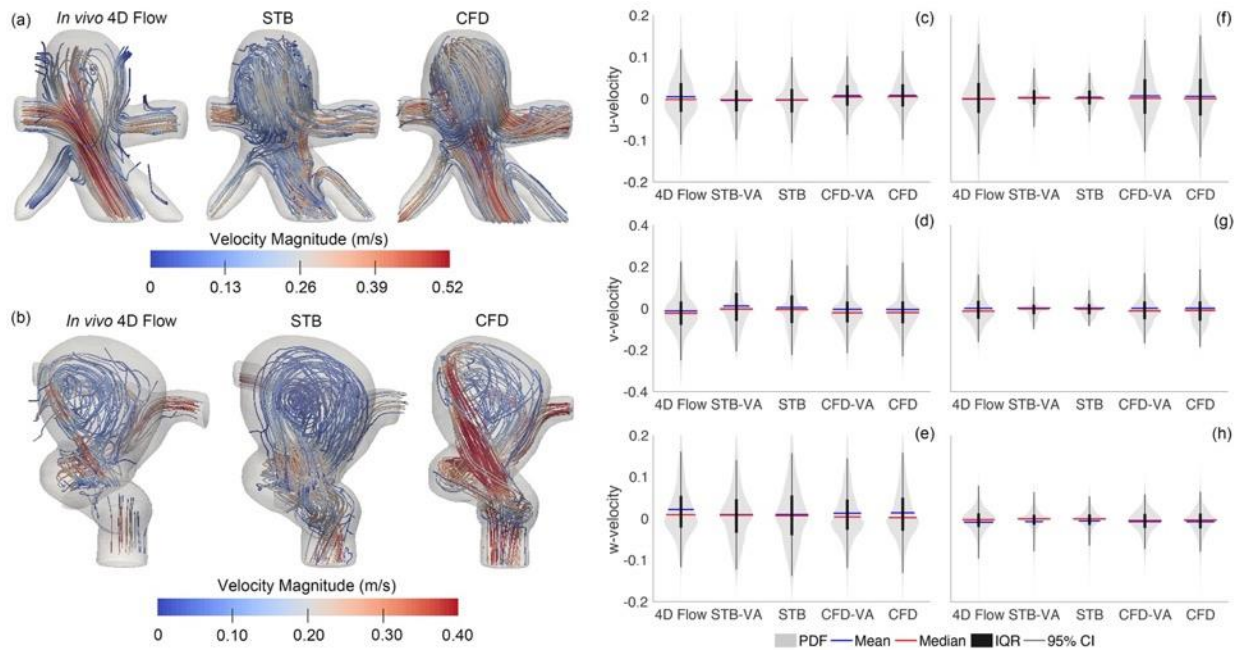
Figure 6-4: Velocity field instantaneous streamlines for the MRI and full resolution STB and CFD at peak systole for the (a) basilar tip aneurysm and (b) ICA aneurysm. (Note: The two aneurysm geometries (a) and (b) are not shown at the same spatial scale.) Distributions of all velocity components throughout the entire pulsatile cycle, spatially limited to the aneurysmal sac only for the (c-e) basilar tip and (f-h) ICA aneurysm. Mean and median values, interquartile ranges (IQR), and 95% confidence intervals (CI) are indicated.

posterior communicating artery (PComA). The swirling flow in the aneurysmal sac was qualitatively similar for the 4D Flow and CFD, while for the STB the swirling was more centered in the sac and the impinging jet was weaker. The velocity distributions in the aneurysmal sac for all modalities throughout the pulsatile cycle are shown in Figure 6-4c-e for the basilar tip aneurysm and Figure 6-4f-h for the ICA aneurysm. The distributions highlight some velocity field differences across the modalities. Similar velocity distributions and velocity ranges were observed across all modalities for the basilar tip aneurysm. The u-velocity component 95% confidence interval ranged from ±11.4 cm/s for 4D Flow, ±10.5 cm/s for STB, and ±10.6 cm/s for CFD. For the v-velocity component the 95% confidence interval ranges were ±23.7, ±22.9, and ±22.6 cm/s for 4D Flow, STB, and CFD, respectively. The ranges for the w-velocity were ±13.9 cm/s for 4D Flow, ±14.7 cm/s for STB, and ±14.5 cm/s for CFD. In the ICA aneurysm, all modalities maintained similar distribution shapes, however STB maintained lower magnitude ranges of the velocity distributions than 4D Flow and CFD. For example, for the u-velocity component, STB maintained a 95% confidence interval range of ±6 cm/s while 4D Flow MRI and CFD maintained 95% confidence interval ranges of ±14 cm/s. The v-velocity 95% confidence interval ranges were ±9 cm/s for STB and ±17 cm/s for 4D Flow and CFD while for the w-velocity they were ±6 cm/s for STB and CFD and ±8 cm/s for 4D Flow.

6.4.2   Evaluating TAWSS, OSI, and RRT across Modalities and Spatial Resolutions

The previous results demonstrate each modality represented the same underlying process, maintaining similar large-scale flow features but with notable flow field variations resulting from uncertainties in the segmentation and boundary conditions, as well as differing spatiotemporal resolution, flow properties and regime assumptions, and limitations across modalities. Next, the effects of the such variations on subsequent hemodynamic metrics was evaluated.

Figure 6-5 shows the distributions of TAWSS, OSI, and RRT in the aneurysmal sac for all modalities for the basilar tip aneurysm (Fig 6-5a-c) and ICA aneurysm (Fig 6-5d-f). The distributions of the TAWSS varied significantly across all five data sets. For the basilar tip aneurysm, the average TAWSS was 6.19 dynes/cm2 for the 4D Flow, 13.88 dynes/cm2 for the full resolution STB, and 11.61 dynes/cm2 for the full resolution CFD. When voxel averaged, the average TAWSS decreased to 5.88 dynes/cm2 for the STB, a 58% drop, and to 6.81 dynes/cm2 for the CFD, a 41% decrease. For the ICA aneurysm, the TAWSS distributions of the 4D Flow, full
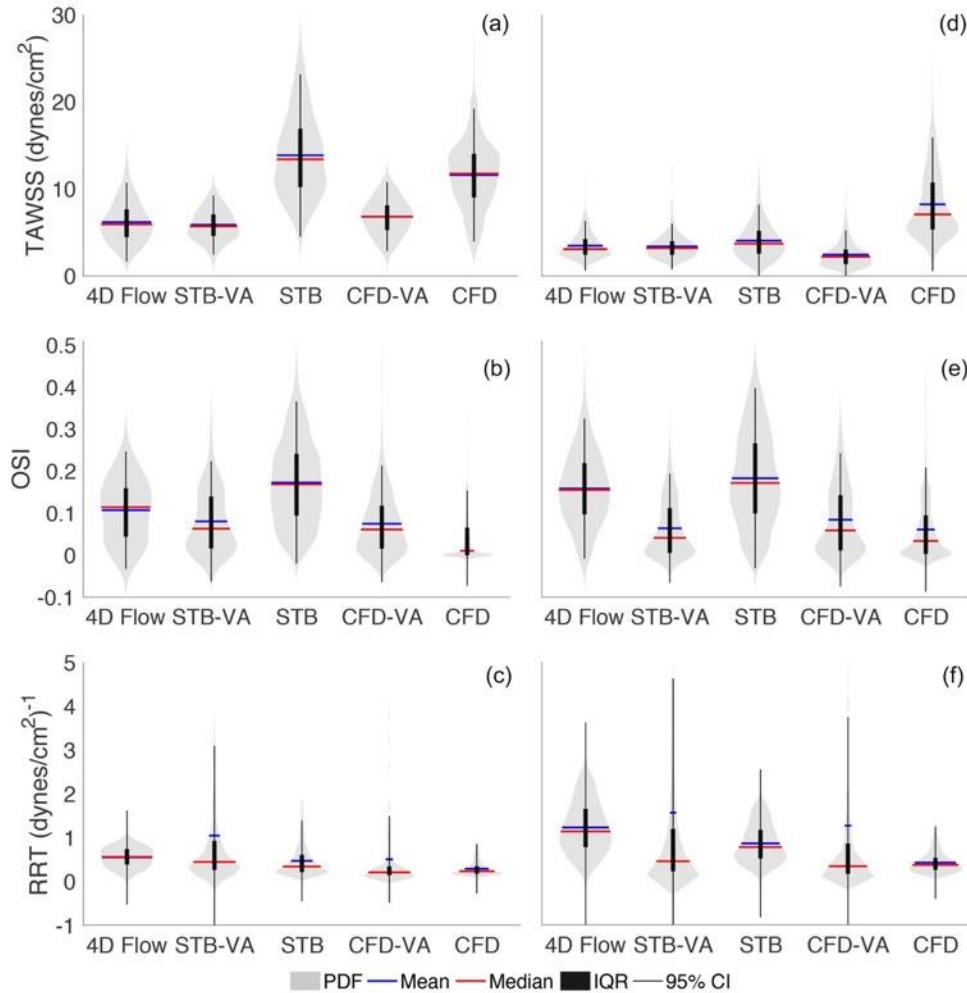
Figure 6-5: Distribution of (a) time averaged wall shear stress (TAWSS), (b) oscillatory shear index (OSI), and (c) relative residence time (RRT) in the basilar tip aneurysm, where width of PDF shows relative distribution density. Distribution of (d) TAWSS, (e) OSI, and (f) RRT in the ICA aneurysm. Mean and median values, interquartile ranges (IQR), and 95% confidence intervals (CI) are indicated.

resolution STB, and voxel averaged STB and CFD showed agreement. The average TAWSS for STB had only a small change from 4.06 to 3.40 dynes/cm2 when voxel averaged. The average CFD TAWSS decreased 70% from 8.25 to 2.46 dynes/cm2 when voxel averaged. The full resolution CFD WSS distribution maintained a larger spread of WSS values than all other modalities and maintained the largest WSS magnitudes. Similar OSI distributions for the basilar tip aneurysm were observed for all modalities except the full resolution CFD. The average OSI of the STB changed from 0.17 to 0.08, while CFD went from 0.04 to 0.07 when voxel averaged. For the ICA aneurysm, good agreement of the OSI distribution and averages was observed between 4D Flow

and STB. The voxel averaged STB and CFD and full resolution CFD OSI distributions and averages matched well. Voxel averaging changed the average OSI from 0.18 to 0.06 for STB and from 0.06 to 0.08 for CFD. Average RRT in the basilar tip aneurysm was 0.55, 0.47, and 0.29 (dynes/cm2)-1 for the 4D Flow, and full resolution STB and CFD, respectively. When voxel averaged, these values changed to 1.05 (dynes/cm2)-1 for STB and 0.50 (dynes/cm2)-1 for CFD. RRT distributions in the ICA aneurysm showed more variation across modalities. Average RRT in the ICA aneurysm was 1.22, 0.86, and 0.42 (dynes/cm2)-1 for the 4D Flow, and full resolution STB and CFD, respectively. Voxel averaging increased the average RRT to 1.56 (dynes/cm2)-1 for STB and to 1.27 (dynes/cm2)-1 for CFD. Overall, OSI showed the best agreement of confidence intervals and interquartile ranges across modalities for both geometries, while TAWSS showed the largest variation of distributions across modalities and RRT maintained the largest variance of 95% confidence intervals, demonstrating the effect of the unbounded RRT calculation.
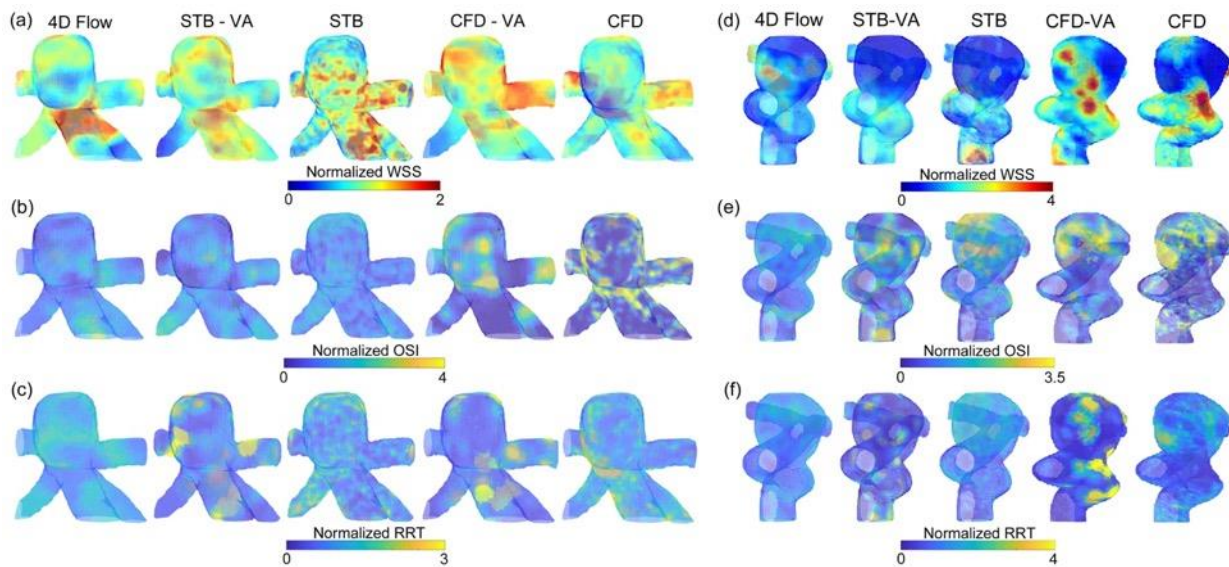
Figure 6-6: Normalized WSS distribution at peak systole for all modalities in the (a) basilar tip aneurysm and (d) ICA aneurysm. Normalized OSI distribution for all modalities in the (b) basilar tip aneurysm and (e) ICA aneurysm. Normalized RRT distribution in the (c) basilar tip and (f) ICA aneurysm. Normalization of the WSS, OSI, and RRT was done for each modality using its own mean value. (Note: The two aneurysm geometries are not shown at the same spatial scale.)

Given the flow field variations across modalities, it is important to investigate and compare the normalized spatial distributions of the hemodynamic metrics. Figure 6-6 illustrates the WSS distribution at peak systole (Fig. 6-6a and 6-6d), and the OSI (Fig. 6-6b and 6-6e) and RRT (Fig. 6-6c and 6-6f) distributions. Each modality's WSS, OSI, and RRT distributions were normalized

by its respective mean value. Even when normalized, the WSS spatial distributions showed large variation across modality and resolution. For the basilar tip aneurysm (Figure 6-6a), the full resolution CFD exhibited a large region of low WSS at the proximal anterior portion of the aneurysmal sac. Conversely, the full resolution STB showed no region of low WSS and 4D Flow maintained a much smaller region of low WSS at that location. Similarly, for the ICA aneurysm normalized WSS (Figure 6-6d), all modalities maintained uniquely different distributions. For both geometries, the normalized RRT distributions also varied significantly across modalities. Although still maintaining some differences, the normalized OSI spatial distributions showed the best agreement across modalities for both geometries. Further, comparing STB-VA vs. STB and CFD-VA vs. CFD, the low spatial resolution and voxel averaging significantly altered the normalized WSS and RRT distributions, but the OSI distributions maintained better agreement.
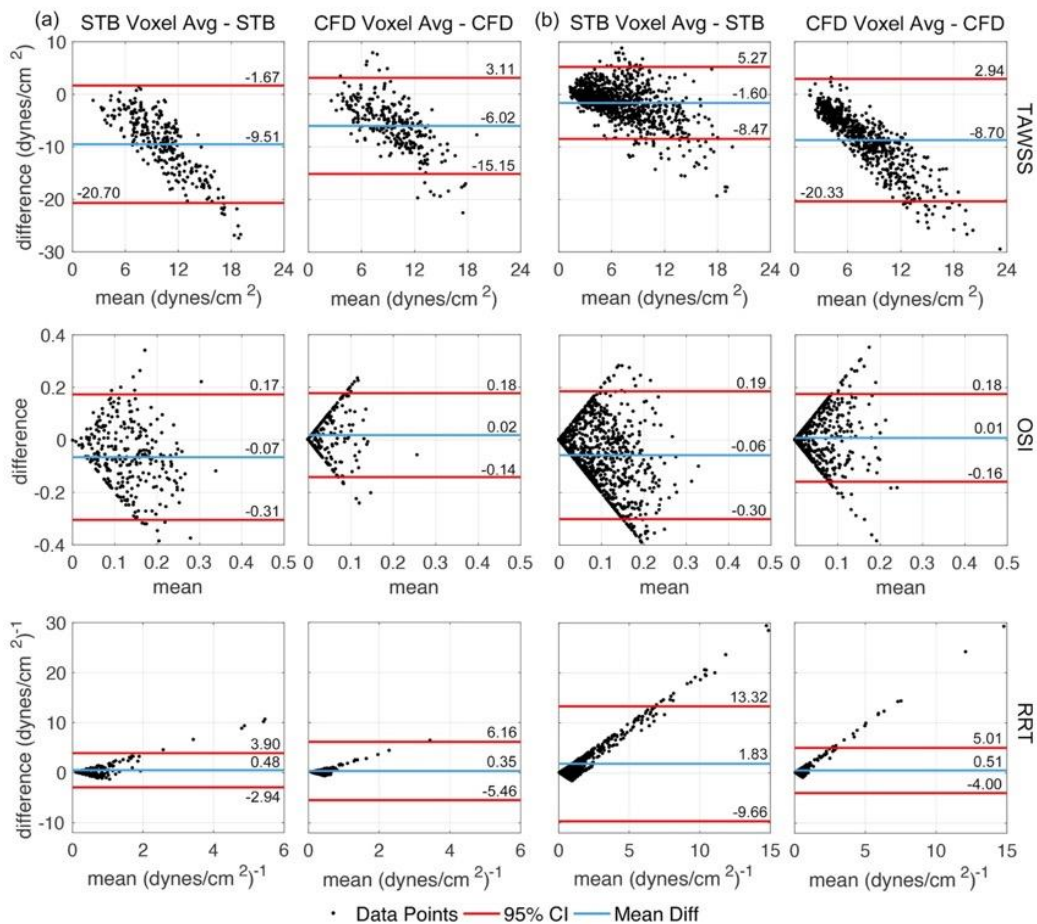
Figure 6-7: Bland-Altman analysis of time averaged wall shear stress, oscillatory shear index, and relative residence time, comparing voxel averaged STB to full resolution STB and voxel averaged CFD to full resolution CFD in the (a) basilar tip aneurysm and (b) ICA aneurysm. Mean difference and 95% confidence intervals are indicated.

To investigate the effect of spatial resolution on TAWSS, OSI, and RRT in more detail, Figure 6-7 illustrates Bland-Altman analysis comparing the voxel averaged and full resolution STB and CFD across the entire flow domain. Using an intra-modality comparison here isolates the effect of spatial resolution. In both aneurysms, a proportional difference of the TAWSS was observed where the voxel averaged TAWSS magnitude was less than that of the full resolution, in agreement with the results in Figure 6-5. The average differences were -9.51 and -6.02 dynes/cm2 for the STB and CFD, respectively, in the basilar tip aneurysm (Fig 6-7a). For the ICA aneurysm (Fig 6-7b), the average TAWSS difference was -1.60 dynes/cm2 for STB and -8.70 dynes/cm2 for CFD. The average OSI difference magnitude across all cases was 0.04, with a maximum difference magnitude of 0.07. The spread of OSI points was relatively symmetric, demonstrating no significant proportional differences. The average RRT difference was 0.48 (dynes/cm2)-1 for the STB and 0.35 (dynes/cm2)-1 for the CFD in the basilar tip aneurysm, and 1.83 and 0.51 (dynes/cm2)-1 for the STB and CFD, respectively, in the ICA aneurysm. A proportional difference was observed with the RRT, but in this case the voxel averaged RRT was larger in magnitude than that of the full resolution. Thus, Figure 6-7 confirms the varying behavior and sensitivity of each metric to spatial resolution.
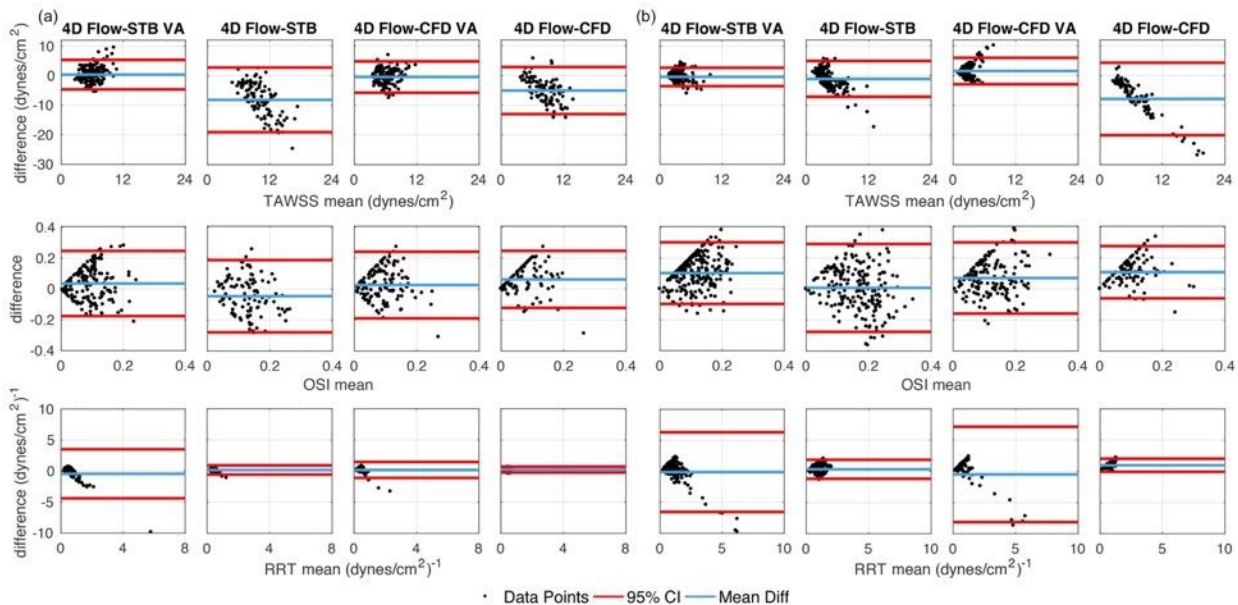
Figure 6-8: Bland-Altman analysis of time averaged wall shear stress, oscillatory shear index, and relative residence time, comparing in vivo 4D Flow MRI to voxel averaged STB (STB-VA), full resolution STB, voxel averaged CFD (CFD-VA), and full resolution CFD in the (a) basilar tip aneurysm and (b) ICA aneurysm. Mean difference and 95% confidence intervals are indicated.

Bland-Altman analysis was performed to specifically compare the *in vitro* and *in silico* TAWSS, OSI, and RRT in the aneurysmal sac to that of the *in vivo* 4D Flow data as well as how the spatial resolution of the *in vitro* and *in silico* datasets affect the comparison (Figure 6-8). In the basilar tip aneurysm (Fig 6-8a), the mean TAWSS difference was -8.19 and -5.05 dynes/cm$_2$ for STB and CFD, respectively. This changed to 0.36 dynes/cm$_2$ for STB-VA and -0.49 dynes/cm$_2$ for CFD-VA. The 95% confidence intervals for the voxel averaged data reduced in range by 54% for STB and 34% for CFD as compared to the full resolution intervals. Similarly, for the ICA aneurysm (Fig 6-8b), the mean TAWSS difference was -1.12 dynes/cm$_2$ for STB and -7.86 dynes/cm$_2$ for CFD. The 95% confidence interval limits reduced by 49 and 64% for STB-VA and CFD-VA, respectively, as compared to the full resolution data. Thus, the voxel averaged datasets generally maintained a better match to the 4D Flow TAWSS than the full resolution datasets. For OSI, the mean difference was -0.05 and 0.06 for STB and CFD, respectively, in the basilar tip aneurysm. Voxel averaging had a small effect, where the mean difference changed to 0.04 for STB and to 0.03 for CFD, while the 95% confidence intervals reduced by only 9% for STB and 17% for CFD. Mean OSI differences of 0.01 for STB, 0.10 for STB-VA, 0.11 for CFD, and 0.07 for CFD-VA were observed in the ICA aneurysm. The interval ranges decreased by 29% when voxel averaged for the STB and increased by 36% when voxel averaged for the CFD. In the basilar tip aneurysm, the mean RRT difference was 0.16 and -0.45 (dynes/cm$_2$)$_{-1}$ for the full resolution and voxel averaged STB, respectively, and 0.24 and 0.17 (dynes/cm$_2$)$_{-1}$ for the full resolution and voxel averaged CFD, respectively. The confidence interval ranges increased fivefold for the STB when voxel averaged and threefold for the CFD when voxel averaged. For the ICA aneurysm, the mean RRT difference was 0.33 (dynes/cm$_2$)$_{-1}$ for the full resolution STB and -0.13 (dynes/cm$_2$)$_{-1}$ for the voxel averaged STB. The mean RRT difference was 0.97 and -0.50 (dynes/cm$_2$)$_{-1}$ for the full resolution and voxel averaged CFD, respectively. The confidence intervals maintained about a fourfold increase in range for the voxel averaged STB dataset as compared to the full resolution while the CFD maintained about a sevenfold increase.

6.5   Discussion

In this work, the effects of spatiotemporal resolution and varying flow assumptions and limitations across modalities on resultant hemodynamic metrics was assessed. The unique implementation of three modalities—where the *in vivo* 4D Flow MRI data informed the *in vitro*

STB and *in silico* CFD—in two time-varying aneurysm flow domains is a significant contribution of this work and provided an enhanced evaluation of the hemodynamic metrics. A major challenge for any multi-modality study that utilizes *in vivo* measurements is that no "ground truth" flow field can be established. The 4D Flow MRI maintains the highest possible level of physiological fidelity because it does not require segmentation or assumptions on flow regime and properties. However, the low spatiotemporal resolution, voxel averaging, and typically high noise compromises the accuracy and overall reliability of calculated hemodynamic metrics. *In vitro* or *in silico* modalities maintain higher resolution and accuracy, but uncertainty in the segmentation and boundary conditions compromises the fidelity, as do modality-specific assumptions (i.e. Newtonian fluid, laminar flow for CFD), solver parameters [15,21], and experimental limitations regarding inflow conditions and noise. In general, each modality yields a unique set of strengths and weaknesses as well as varying accuracy, physiological fidelity, and resolution. The results here demonstrated WSS, OSI, and RRT maintained differing behavior when subjected to these flow domain variations across modalities. Thus, this analysis can provide a framework for improving the robustness and universality of hemodynamic-based risk of rupture assessments through additional multi-modality studies that develop methods to optimally synthesize information across modalities in order to enhance the accuracy, fidelity, and clinical utility of *in vivo* hemodynamic representations.

Low WSS regions and their impact on risk of growth and rupture have received much attention [3,6,11,12,16,20]. As seen in Figure 6-6, all modalities had uniquely different regions of normalized low WSS and RRT in the aneurysmal sacs of both geometries, even across cases which had strong agreement in the flow patterns and velocity distributions (i.e. 4D Flow and CFD for the ICA aneurysm). In this study, one WSS calculation methodology was used and variations in the proximity of the velocity vectors to the wall were mitigated to ensure consistent calculation bias across cases. Further, Cebral et al. (2011) [13] showed inflow waveform changes can cause variability on the magnitude but not spatial variation of hemodynamic metrics and van Ooij et al. (2013) [16] demonstrated similar findings regarding spatial resolution. However, WSS and RRT calculations are highly sensitive to the near-wall velocity field, and across modalities different accuracy and resolution in the near-wall region is expected. CFD is highly resolved in the near-wall region and enforces the no-slip boundary condition, ensuring zero-flow at the wall. Conversely, resolving the no-slip condition for MRI or STB is unlikely and in MRI the low velocity flow is known to maintain substantially higher noise. Compounding ancillary factors such

as variations in inlet flow conditions, the Newtonian fluid assumption, and physical aneurysm orientation can plausibly influence resulting hemodynamic forces, though future work is needed to expand the specific relationships. Moreover, these factors, some of which could be time or spatially varying, hinder the robustness of both WSS and RRT and their ability to inform aneurysm stability. For example, the assessed stability of the basilar tip aneurysm here would likely be different based on the WSS distribution obtained from the full resolution CFD versus that obtained from the full resolution STB. Further, studies which investigate hemodynamic variables in order to determine which variables have a statistically significant difference between stable and unstable aneurysms, regardless of modality, would be influenced by these factors, possibly confounding statistically significant results.

The effect of voxel averaging and spatial resolution on hemodynamic metric magnitudes has also been a growing concern. Roloff et al. (2018) [15] demonstrated reductions of velocity magnitude by as much as 10-20% because of voxel averaging. van Ooij et al. (2013) [16] reported WSS values for 4D Flow MRI were lower than that of CFD, but increased if the MRI spatial resolution was increased. Figure 8 is in agreement with this notion, demonstrating that datasets with similar spatial resolutions have similar TAWSS magnitudes and lowering the spatial resolution generally lowers the WSS magnitude. In Figure 6-7, reduction (bias error) of TAWSS caused by virtual voxel averaging within the same modality was about 6.46 dynes/cm$_2$, corresponding to a roughly 72% error when normalizing by the mean TAWSS across all datasets. The effect of spatial resolution on OSI and RRT by contrast has received very limited attention. The average RRT error caused by voxel averaging was 0.79 (dynes/cm$_2$)$_{-1}$, a 125% error when normalizing by the mean RRT across all datasets. However, the average OSI bias error caused by voxel averaging was 0.04, a 50% error when normalized by the mean OSI across all datasets. Further, in Figure 6-8, comparing the *in vitro* and *in silico* datasets to the *in vivo* 4D Flow, OSI had the most consistent 95% interval bounds across all modalities as well as across full resolution and voxel averaged datasets within the same modality.

Overall, OSI was more robust to varying limitations, assumptions, and spatial resolution, and maintained more consistent magnitude and spatial distributions than both TAWSS and RRT. OSI yielded no proportional or significant bias errors for all datasets and comparisons. Because OSI is a non-dimensional parameter, its magnitude is less affected by bias errors than equivalent dimensional parameters, as bias scale errors in the WSS magnitude would cancel out in the OSI

calculation Equation (6.6). As previously discussed, bias errors are unavoidable across all modalities and subjects and are attributed, at least in part, to the assumptions and spatial resolution of the data as well as calculation methodologies. Thus, OSI and other non-dimensional parameters offer the potential for more consistent hemodynamic risk analysis across a cohort of varying geometries and 4D Flow resolutions than equivalent dimensional parameters. This is a notion that should be explored and expanded in future studies.

There were several limitations of this study. The inlet vessel of the *in vitro* models had to be curved slightly for experimental and manufacturing reasons. This could have had some effect on inflow conditions of the STB experiment, possibly preventing a fully developed inflow. However, given the natural tortuosity of the cerebral vasculature, the exact *in vivo* inflow conditions would be complex and not necessarily fully-developed. For example, in Figure 1c, the *in vivo* inflow of the ICA geometry contains a significant curve, similar to what was manufactured for this study. Further, passive resistance valves were used to control the outlet flow rates such that only the average flow rate throughout the pulsatile cycle in each vessel could be controlled. Thus, the amplitude of pulsatility in each vessel could not be controlled and differences in the outlet flow rate pulsatility amplitude of the smaller vessels was observed. Small batches of the working fluid were made for each geometry test such that the working fluids were slightly different. However, because no cross-geometry comparisons were done, this did not impact the results. Uncertainty quantification methods are widely available for PIV but have yet to be reported for STB and are needed so this data can be used as robust validation test cases for CFD simulations. While virtual spatial voxel averaging was done here, this process does not exactly replicate that of MRI voxel or ensemble averaging. Thus, additional studies are needed to further explore the possible effects of voxel averaging on velocity and post-processing metrics identified in this study using higher fidelity voxel averaging techniques. Bias errors in discrete WSS calculations are well documented in the literature [19,51]. From the WSS algorithm validation done for this study, a consistent bias error was a known issue. Further, although the working fluid was highly controlled and optimized, the STB and CFD dynamic viscosities differed by 4 and 13% for the basilar tip and ICA aneurysms, respectively, and for the *in vivo* 4D Flow the viscosity was not explicitly known and had to be assumed. These viscosity variations could plausibly have caused minor differences in the near-wall flow and thus WSS for each modality, but this effect was not expected to be significant nor alter the conclusions of this work. Therefore, all WSS, OSI, and RRT values reported in this study

can validly be interpreted in a relative sense, but global values of these metrics cannot be extrapolated from this study.

6.6   Conclusions

In this study, we conducted a multi-modality comparison using *in vivo* 4D Flow MRI, *in vitro* volumetric flow velocimetry data, and *in silico* CFD in order to investigate the robustness of TAWSS, OSI, and RRT to inherent boundary condition uncertainties and modality-specific assumptions. Here, Shake-the-Box processing of particle images significantly reduced reconstruction errors, advancing the state-of-the-art experimental capability and fidelity among cerebral aneurysm studies. The notable, differences of WSS and RRT distributions across modalities demonstrated that more in-depth and comprehensive sensitivity analysis of specific assumptions and limitations on such metrics is needed. Further, non-dimensional parameters, such as OSI, were shown to be more robust and consistent to varying modalities and spatial resolutions, a finding which can improve flow metrics associated with aneurysm risk of rupture in future work. However, given the limitations of this study, additional work is needed to further investigate these findings.

6.7   Acknowledgements

CHAPTER 7. CONCLUSIONS AND FUTURE WORK

7.1   Conclusions

The goal of this work was to develop methodologies to mitigate the complexity of IA hemodynamic experimental PIV studies, expand the understanding of mechanisms that lead to the onset and development of transitional flow in biologically relevant pulsatile flows, and experimentally test the influence of hemodynamics in two independent cardiovascular regions.

7.1.1   Advancing Experimental Methods in Cerebral Aneurysm Studies

The cultivation of Chapters 2, 3, and 6 provide a road map for future experimental cerebral aneurysm studies which can be used to substantially improve both the number and accuracy of PIV studies in the cerebral aneurysm domain.

The developed autonomous POD truncation method, ELF, can be used to reduce experimental noise in resulting velocity fields. For IA studies, experimental noise is of particular importance because the complex, highly curved, 3-D geometries will yield optical distortions that can be mitigated, but not eliminated, and will propagate into the computed flow fields. Further, the effect of transitional flow on IA hemodynamics requires a noise mitigation technique which does not remove or corrupt the fidelity of small-scale transitional flow structures. Considering these requirements, the ELF method is autonomous, removing any possible user subjectivity, and excels at distinguishing small-scale flow structures from small-scale noise. Therefore, the ELF method is well-suited for use in cerebral aneurysm PIV studies.

The developed water-glycerol-urea blood analog working fluid reduces the complexity and cost of conducting PIV cerebral aneurysm studies. Most often cerebral aneurysm PIV studies use PDMS to manufacture the test section because it is versatile and allows the compliance of the geometry to be controlled [15,20]. Further, MRI-based IA studies typically use a 60/40 (by volume) mixture of water-glycerol as a density and viscosity-matched blood analog. However, the RI of PDMS is 1.41, while the RI of a 60/40 water-glcyerol mixture is 1.39, a substantial and inadmissible difference for PIV experiments. The accepted solution to this RI-mismatch among IA PIV studies is most often to add NaI to the water-glycerol to increase the index of refraction [15,17,95]. However, it is not possible for a water-glycerol-NaI solution to simultaneously match the RI of PDMS as well as the density and viscosity of blood and NaI is considerably costly and

difficult to work with. Using urea as an additive to water-glycerol substantially mitigates all of these issues, thereby enhancing the accuracy of PIV techniques for cerebral aneurysm studies. Further, for MRI studies, a suitable water-urea mixture could be produced. Because water-urea has a considerably less oily consistency than water-glycerol, it would be easier to work with and reduce the detrimental effects of possible fluid leaks in the MRI machine.

7.1.2 Understanding Transitional Flow in Cerebral Aneurysms

Preliminary studies have demonstrated that transitional flow exists within cerebral aneurysms and can have an influential effect on an IA's risk of growth and rupture [9]. However, the mechanisms that cause the onset and development of transition to turbulence in pulsatile flows are not well understood, requiring fundamental flow physics studies. In Chapter 4, it was demonstrated that different pulsatile waveforms can produce varying behavior of the onset and magnitude of transitional flow. For an IA, different areas of the cerebral vasculature have different inflow waveforms and thus would have different influences of transitional flow behavior. Therefore, it follows that the varying levels of intermittency from transitional flow across aneurysms would yield different effects on resultant hemodynamic metrics and IA risk of rupture. This again suggests a connection between hemodynamic and morphological variables, in this case between aneurysmal location and transitional flow behavior. Additional studies are needed to develop specific relationships of inflow pulsatile waveform characteristics and transitional flow.

7.1.3 Expanding the Hemodynamic Evaluation in IA Studies

While a variety of hemodynamic metrics have been evaluated in IA studies and such studies have sought to link these metrics to risk of rupture, few studies have investigated the robustness and consistency of such metrics across different modalities, spatiotemporal resolutions, and flow assumptions. Yet, inconsistencies among evaluation metrics could play a significant role in the contradictory results reported among risk of rupture studies. In Chapter 6, such an evaluation was done for TAWSS, OSI, and RRT. This analysis showed that, OSI, a non-dimensional parameter was more robust to changing modalities, resolutions, and assumptions than TAWSS and RRT, both dimensional parameters. Thus, future studies aiming to improve IA risk of growth and rupture hemodynamic assessment should specifically focus on testing and developing non-dimensional parameters.

Some hemodynamic metrics have received little to no attention in the cerebral aneurysm domain, even in cases where such parameters have been proven to be significant in other cardiovascular regions. In Chapter 5, PWV was demonstrated to provide insight into restenosis among different coronary bifurcation stenting techniques. This analysis is translatable to both IA risk of rupture and IA risk of treatment evaluations, yet IA studies have rarely considered this metric or pressure fields at all. Thus, this work demonstrates a need for evaluating additional hemodynamic metrics in order to develop improved risk of rupture assessments.

7.2   Future Work

7.2.1   Using PIV to Bridge the Gap of Hemodynamic and Morphological Variables

The work presented here demonstrates the independent and unique value of experimental studies in the cerebral aneurysm domain. Moreover, stand-alone PIV studies in the cerebral aneurysm domain remain exceptionally limited and among one of the largest gaps in the current literature. Yet, PIV requires substantially less flow field assumptions than CFD, making it a useful modality for exploring specific effects of morphological variables on the resulting hemodynamic environment, thereby providing a means to develop relationships between such parameters.

For example, CFD studies in this domain almost universally neglect gravity, but no study has tested the validity of this assumption. Further, the analysis completed for the multi-modality cerebral aneurysm study suggested a possible influence of gravitational forces on IA hemodynamics. Thus, the resultant hypothesis was that the physical orientation of the cerebral aneurysm has a non-negligible effect on the flow field and hemodynamic forces within the aneurysmal sac. This hypothesis crosses between morphological variables (aneurysm orientation) and hemodynamic variables. PIV was used to test this hypothesis by using two patient-specific IA geometries both imaged at two orthogonal and physiologically-relevant aneurysm orientations. The two orientations tested consisted of a "horizontal" orientation (Figure 7-1a) representing a person in the supine position and a "vertical" orientation (Figure 7-1b) representing a person standing up.

Preliminary results demonstrate subtle, yet significant differences between the flow fields of the two orientations. Specifically, Figure 7-2 shows the velocity fields (Figure 7-2a) and vorticity fields (Figure 7-2b) of a basilar tip aneurysm in the horizontal and vertical orientations.
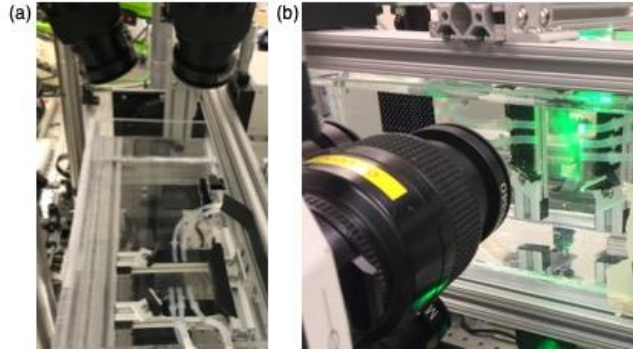
Figure 7-1: Pictures of an in vitro basilar tip aneurysm model
in the (a) horizontal position and (b) vertical position.
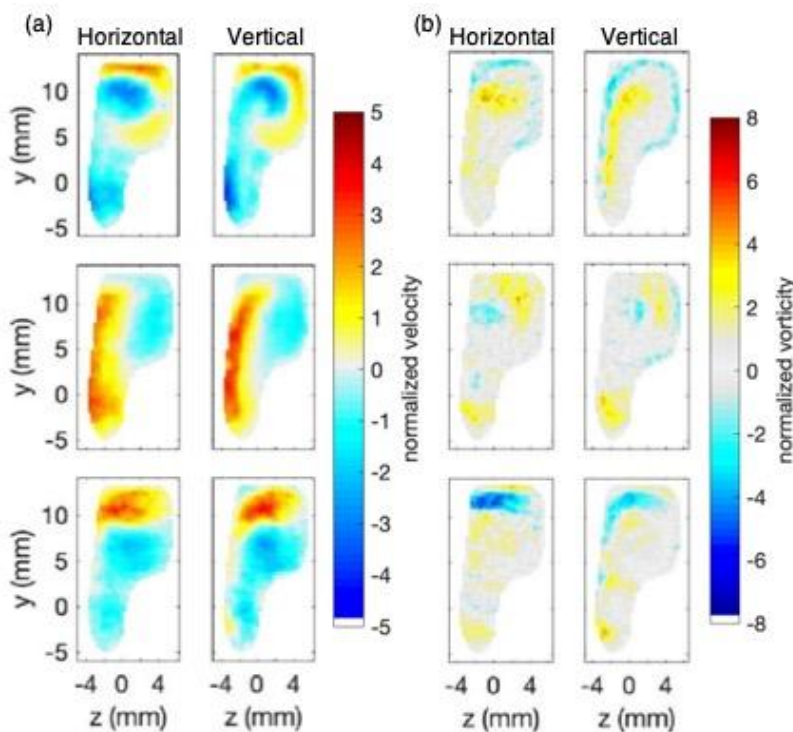
Figure 7-2: (a) Velocity fields and (b) vorticity fields for both the horizontal and
vertical orientations at a Y-Z cut-plane in the center of the basilar tip aneurysm.

From Figure 7-2, it is evident that the two orientations yield different structures of the swirling flow in the aneurysmal sac. Further, Figure 7-3 shows the probability density function (PDF) of the PWV within the aneurysmal sac for the two orientations. Between the two orientations, a shift of PWV magnitude is observed suggesting the vertical case induces a higher impedance on the flow. This suggests that gravitational forces, and thus aneurysm orientation, can have a realizable effect on the resulting hemodynamic environment within an IA. Because this study is restricted to

in vitro PIV, these results cannot be extrapolated to make conclusions regarding the effect of aneurysm orientation on *in vivo* hemodynamic metrics. But these results do necessitate evaluation of the *in vivo* relationship of gravity and IA flow fields.
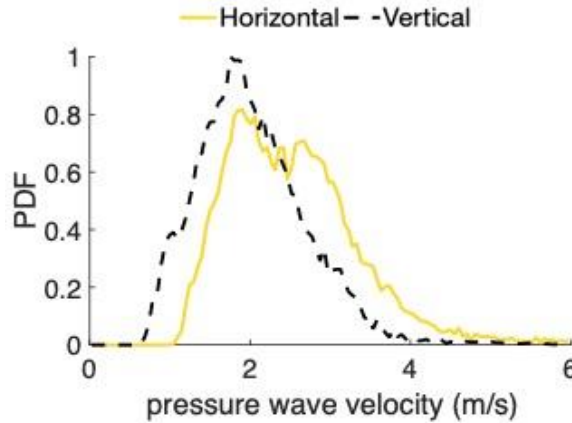
Figure 7-3: PDF of the PWV within the aneurysmal sac for the basilar tip aneurysm at both the horizontal and vertical orientations.

7.2.2 Developing Time-Frequency Methods for IA Studies

Assessing and quantifying the intermittent characteristics of transitional flow behavior is challenging and remains a gap among current literature. Yet, such a methodology is needed in order to evaluate intermittent and high-frequency fluctuating transitional flow within an aneurysmal sac. Preliminary work has focused on the development of a wavelet and Hilbert transform-based time-frequency evaluation method (WHTF) which is schematically shown in Figure 7-4 and is comparable to the dual-tree discrete wavelet transform (DT-DWT). The WHTF aims to provide the instantaneous frequency in both time and space. Using the WHTF method, coherent frequency structures (CFS) can be identified. These CFS can provide insight across a spectrum of applications from coherent flow structures to functional MRI (fMRI) activation maps. For example, Figure 7-5 shows the comparison of an fMRI activation map based on traditional statistical analysis to one based on the WHTF analysis. Evident similarities between the two activation maps demonstrate the value of CFS. While additional development and testing are needed for the WHTF method, this method would be well-suited for evaluating fluctuating characteristics of IA hemodynamic metrics.
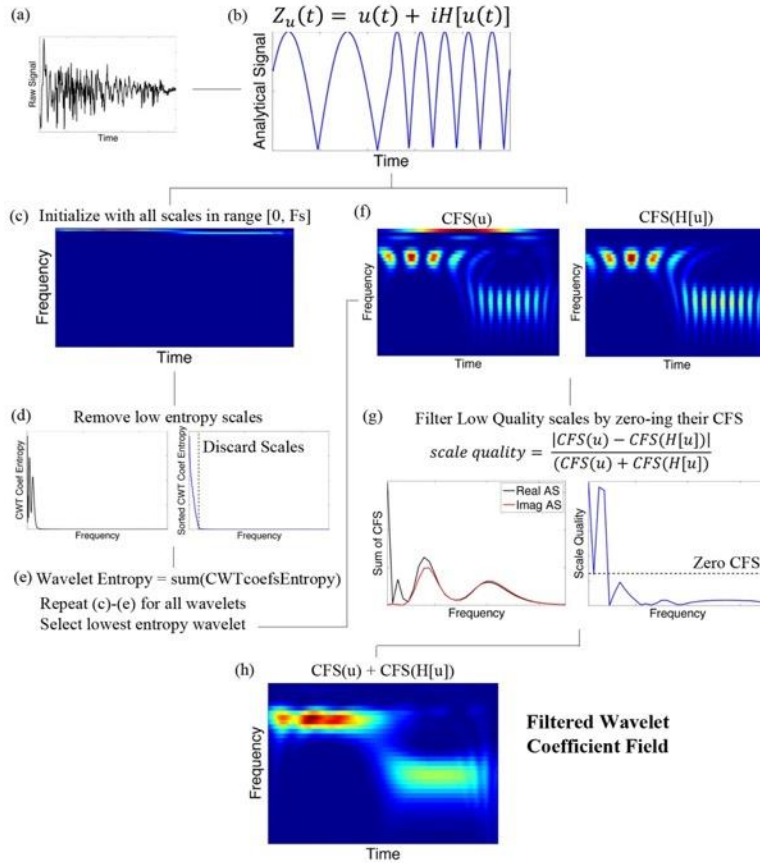
Figure 7-4: Schematic of the WHTF methodology.
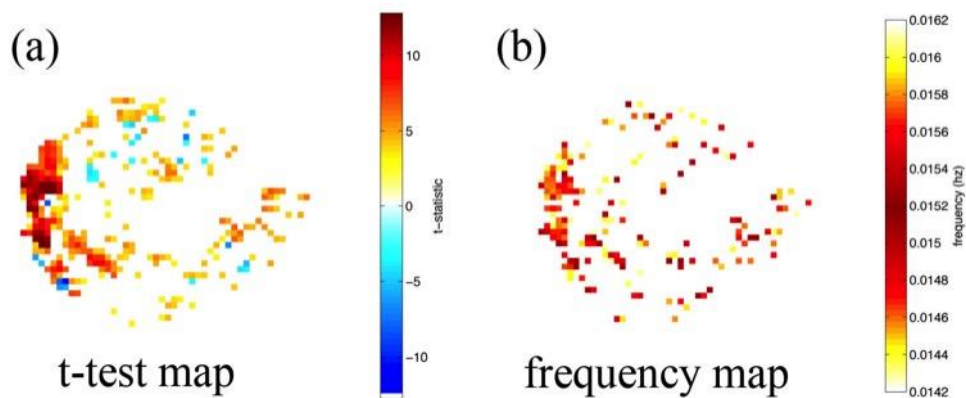
Figure 7-5: fMRI activation maps computed using (a) general linear model statistical methods and (b) the WHTF method.

REFERENCES

1. Rayz VL, Abla A, Boussel L, Leach JR, Acevedo-Bolton G, Saloner D, et al. Computational Modeling of Flow-Altering Surgeries in Basilar Aneurysms. Ann Biomed Eng. 2015;43(5):1210–22.

2. Lauric A, Miller E, Frisken S, Malek AM. Automated detection of intracranial aneurysms based on parent vessel 3D analysis. Med Image Anal [Internet]. 2010;14(2):149–59. Available from: http://dx.doi.org/10.1016/j.media.2009.10.005

3. Meng H, Tutino VM, Xiang J, Siddiqui A. High WSS or Low WSS? Complex interactions of hemodynamics with intracranial aneurysm initiation, growth, and rupture: Toward a unifying hypothesis. Am J Neuroradiol. 2014;35(7):1254–62.

4. Greving JP, Wermer MJH, Brown RD, Morita A, Juvela S, Yonekura M, et al. Development of the PHASES score for prediction of risk of rupture of intracranial aneurysms: A pooled analysis of six prospective cohort studies. Lancet Neurol. 2014;13(1):59–66.

5. Detmer FJ, Chung BJ, Mut F, Slawski M, Hamzei-Sichani F, Putman C, et al. Development and internal validation of an aneurysm rupture probability model based on patient characteristics and aneurysm location, morphology, and hemodynamics. Int J Comput Assist Radiol Surg. 2018;13(11):1767–79.

6. Xiang J, Natarajan SK, Tremmel M, Ma D, Mocco J, Hopkins LN, et al. Hemodynamic-morphologic discriminants for intracranial aneurysm rupture. Stroke. 2011;42(1):144–52.

7. Backes D, Vergouwen MDI, Velthuis BK, Van Der Schaaf IC, Bor ASE, Algra A, et al. Difference in aneurysm characteristics between ruptured and unruptured aneurysms in patients with multiple intracranial aneurysms. Stroke. 2014;45(5):1299–303.

8. Lindgren AE, Koivisto T, Bjorkman J, Von Und Zu Fraunberg M, Helin K, Jaaskelainen JE, et al. Irregular Shape of Intracranial Aneurysm Indicates Rupture Risk Irrespective of Size in a Population-Based Cohort. Stroke. 2016;47(5):1219–26.

9. Valen-Sendstad K, Mardal KA, Steinman DA. High-resolution CFD detects high-frequency velocity fluctuations in bifurcation, but not sidewall, aneurysms. J Biomech. 2013;46(2):402–7.

10. Tominari S, Morita A, Ishibashi T, Yamazaki T, Takao H, Murayama Y, et al. Prediction model for 3-year rupture risk of unruptured cerebral aneurysms in Japanese patients. Ann Neurol. 2015;77(6):1050–9.

11. Boussel L, Rayz V, McCulloch C, Martin A, Acevedo-Bolton G, Lawton M, et al. Aneurysm growth occurs at region of low wall shear stress: Patient-specific correlation of hemodynamics and growth in a longitudinal study. Stroke. 2008;39(11):2997–3002.

12. Tanoue T, Tateshima S, Villablanca JP, Vinuela F, Tanishita K. Wall Shear Stress Distribution Inside Growing Cerebral Aneurysm. Am J Neuroradiol. 2011;32(9):1732–7.

13. Cebral JR, Mut F, Weir J, Putman C. Quantitative characterization of the hemodynamic environment in ruptured and unruptured brain aneurysms. Am J Neuroradiol. 2011;32(1):145–51.

14. Castro MA, Putman CM, Cebral JR. Computational fluid dynamics modeling of intracranial aneurysms: Effects of parent artery segmentation on intra-aneurysmal hemodynamics. Am J Neuroradiol. 2006;27(8):1703–9.

15. Roloff C, Stucht D, Beuing O, Berg P. Comparison of intracranial aneurysm flow quantification techniques: standard PIV vs stereoscopic PIV vs tomographic PIV vs phase-contrast MRI vs CFD. J Neurointerv Surg. 2018;neurintsurg-2018-013921.

16. van Ooij P, Potters W V., Guédon A, Schneiders JJ, Marquering HA, Majoie CB, et al. Wall shear stress estimated with phase contrast MRI in an in vitro and in vivo intracranial aneurysm. J Magn Reson Imaging. 2013;38(4):876–84.

17. van Ooij P, Guedon A, Poelma C, Schneiders J, Rutten MCM, Marquering HA, et al. Complex flow patterns in a real-size intracranial aneurysm phantom: Phase contrast MRI compared with particle image velocimetry and computational fluid dynamics. NMR Biomed. 2012;25(1):14–26.

18. Ford MD, Nikolov HN, Milner JS, Lownie SP, Demont EM, Kalata W, et al. PIV-Measured Versus CFD-Predicted Flow Dynamics in Anatomically Realistic Cerebral Aneurysm Models. J Biomech Eng. 2008;130(2):021015.

19. Yagi T, Sato A, Shinke M, Takahashi S, Tobe Y, Takao H, et al. Experimental insights into flow impingement in cerebral aneurysm by stereoscopic particle image velocimetry: transition from a laminar regime. J R Soc Interface. 2013;10(82):20121031.

20. Kojima M, Irie K, Ikeda S, Fukada T, Arai F, Hirose Y, et al. The hemodynamic study for growth factor evaluation of rupture cerebral aneurysm followed up for five years. J Biomed Sci Eng. 2012;05(12):884–91.

21. Berg P, Roloff C, Beuing O, Voss S, Sugiyama SI, Aristokleous N, et al. The Computational Fluid Dynamics Rupture Challenge 2013 - Phase II: Variability of Hemodynamic Simulations in Two Intracranial Aneurysms. J Biomech Eng. 2015;137:121008.

22. Berg P, Stucht D, Janiga G, Beuing O, Speck O, Thévenin D. Cerebral Blood Flow in a Healthy Circle of Willis and Two Intracranial Aneurysms: Computational Fluid Dynamics Versus Four-Dimensional Phase-Contrast Magnetic Resonance Imaging. J Biomech Eng. 2014;136(4):041003.

23. Yasuda R, Strother CM, Taki W, Shinki K, Royalty E, Pulfer K, et al. Aneurysm Volume-to-Ostium Area Ratio: A Parameter Useful for Discriminating the Rupture Status of

Intracranial Aneurysms. Neurosurgery. 2011;68(2):310–5.

24. Bor ASE, Tiel Groenestege AT, terBrugge KG, Agid R, Velthuis BK, Rinkel GJE, et al. Clinical, radiological, and flow-related risk factors for growth of untreated, unruptured intracranial aneurysms. Stroke. 2015;46(1):42–8.

25. Castro MA, Putman CM, Sheridan MJ, Cebral JR. Hemodynamic patterns of anterior communicating artery aneurysms: A possible association with rupture. Am J Neuroradiol. 2009;30(2):297–302.

26. Qian Y, Takao H, Umezu M, Murayama Y. Risk analysis of unruptured aneurysms using computational fluid dynamics technology: preliminary results. Am J Neuroradiol. 2011;32(10):1948–55.

27. Cebral JR, Mut F, Weir J, Putman CM. Association of hemodynamic characteristics and cerebral aneurysm rupture. Am J Neuroradiol. 2011;32(2):264–70.

28. Parker KH, Davies JE, Francis D, Hughes AD, Mayet J. Arterial pulse wave velocity in coronary arteries. 2006;2(1):867–70.

29. Liao J, Farmer J. Arterial stiffness as a risk factor for coronary artery disease. Curr Atheroscler Rep. 2014;16(2):387.

30. Brindise MC, Chiastra C, Burzotta F, Migliavacca F, Vlachos PP. Hemodynamics of Stent Implantation Procedures in Coronary Bifurcations: An In Vitro Study. Ann Biomed Eng. 2016;45(3):543–53.

31. Brindise MC, Vlachos PP. Pulsatile pipe flow transition: Flow waveform effects. Phys Fluids. 2018;30(1):015111.

32. Trip R, Kuik DJ, Westerweel J, Poelma C. An experimental study of transitional pulsatile pipe flow. Phys Fluids. 2012;24(1):014103.

33. Varghese SS, Frankel SH, Fischer PF. Direct numerical simulation of stenotic flows. Part 2. Pulsatile flow. Vol. 582, Journal of Fluid Mechanics. 2007. 281–318 p.

34. Sherwin SJ, Blackburn HM. Three-dimensional instabilities of steady and pulsatile axisymmetric stenotic flows. J Fluid Mech. 2005;533:297–327.

35. Kefayati S, Poepping TL. Transitional flow analysis in the carotid artery bifurcation by proper orthogonal decomposition and particle image velocimetry. Med Eng Phys. 2013;35(7):898–909.

36. Poelma C, Watton PN, Ventikos Y. Transitional flow in aneurysms and the computation of haemodynamic parameters. J R Soc Interface. 2015;12(105):20141394.

37. Jain K, Jiang J, Strother C, Mardal KA. Transitional hemodynamics in intracranial aneurysms - Comparative velocity investigations with high resolution lattice Boltzmann

simulations, normal resolution ANSYS simulations, and MR imaging. Med Phys. 2016;43(11):6186–98.

38.   Bergamino M, Saitta L, Castellan L, Zona G, Bartolini B, Spaziante R, et al. Cerebral Aneurysms Database, a New Free Database for Intracranial Aneurysms. Neuroinformatics. 2011;42:1–4.

39.   Saqr KM, Mansour O, Tupin S, Hassan T, Ohta M. Evidence for non-Newtonian behavior of intracranial blood flow from Doppler ultrasonography measurements. Med Biol Eng Comput. 2019;57(5):1029–36.

40.   Patil VA, Liburdy JA. Optical measurement uncertainties due to refractive index mismatch for flow in porous media. Exp Fluids. 2012;53(5):1453–68.

41.   Sirovich L. Turbulence and the Dynamics of Coherent Structures, I-III. Q Appl Math. 1987;45(3):561–71.

42.   Berkooz G, Holmes P, Lumley JL. The proper orthogonal decomposition in the analysis of turbulent flows. Annu Rev Fluid Mech. 1993;25(1971):539–75.

43.   Smith TR, Moehlis J, Holmes P. Low-dimensional modelling of turbulence using the proper orthogonal decomposition: A tutorial. Nonlinear Dyn. 2005;41(1–3):275–307.

44.   Kostas J, Soria J, Chong MS. A comparison between snapshot POD analysis of PIV velocity and vorticity data. Exp Fluids. 2005;38(2):146–60.

45.   Jørgensen BH. Application of POD to PIV Images of Flow Over a Wall Mounted Fence. Sørensen JN, Hopfinger EJ, Aubry N, editors. IUTAM Symp Simul Identif Organ Struct Flows. 1999;52:397–407.

46.   Müller SHR, Böhm B, Gleißner M, Grzeszik R, Arndt S, Dreizler A. Flow field measurements in an optically accessible, direct-injection spray-guided internal combustion engine using high-speed PIV. Exp Fluids. 2010;48(2):281–90.

47.   Stewart KC, Vlachos PP. Vortex rings in radially confined domains. Exp Fluids. 2012 Jul 7;53(4):1033–44.

48.   Charonko J, Karri S, Schmieg J, Prabhu S, Vlachos P. In vitro comparison of the effect of stent configuration on wall shear stress using time-resolved particle image velocimetry. Ann Biomed Eng. 2010 Mar;38(3):889–902.

49.   Adrian RJ, Christensen KT, Liu Z-C. Analysis and interpretation of instantaneous turbulent velocity fields. Exp Fluids. 2000;29(3):275–90.

50.   Charonko JJ, King C V, Smith BL, Vlachos PP. Assessment of pressure field calculations from particle image velocimetry measurements. Meas Sci Technol. 2010;21(10):105401.

51.   Karri S, Charonko J, Vlachos PP. Robust wall gradient estimation using radial basis

functions and proper orthogonal decomposition (POD) for particle image velocimetry (PIV) measured fields. Meas Sci Technol. 2009;20(4):045401.

52. Holmes P, Lumley JL, Berkooz G, Rowley CW. Turbulence, Coherent Structures, Dynamical Systems and Symmetry. 1996.

53. Tropea C, Yarin AL, Foss JF. Handbook of experimental fluid mechanics. Vol. 53, Journal of Chemical Information and Modeling. 2007. 1043–1080 p.

54. Algazi VR, Sakrison DJ. A note on the optimality of the Karhunen-Loeve expansion. IEEE Trans Inf Theory. 1969;15(2):319–21.

55. Charonko JJ, Kumar R, Stewart K, Little WC, Vlachos PP. Vortices formed on the mitral valve tips aid normal left ventricular filling. Ann Biomed Eng. 2013 May;41(5):1049–61.

56. Epps BP, Techet AH. An error threshold criterion for singular value decomposition modes extracted from PIV data. Exp Fluids. 2010;48(2):355–67.

57. Raiola M, Discetti S, Ianiro A. On PIV random error minimization with optimal POD-based low-order reconstruction. Exp Fluids. 2015;56(4).

58. Raiola M, Discetti S. Personal Communication. 2016.

59. Ahmed N, Natarajan T, Rao KR. Discrete Cosine Transform. IEEE Trans Comput. 1974;(January):90–3.

60. Aubry N, Guyonnet R, Lima R. Spatiotemporal analysis of complex signals: theory and applications. J Stat Phys. 1991;vol.64(no.3-4):683–739.

61. Bulusu K, Plesniak M. Shannon Entropy-Based Wavelet Transform Method for Autonomous Coherent Structure Identification in Fluid Flow Field Data. Entropy. 2015;17(10):6617–42.

62. Abutaleb AS. Automatic thresholding of gray-level pictures using two-dimensional entropy. Comput Vision, Graph Image Process. 1989;47(1):22–32.

63. Soon IY, Koh SN, Yeo CK. Noisy speech enhancement using discrete cosine transform. Speech Commun. 1998;24(3):249–57.

64. Chen WH, Pratt WK. Scene Adaptive Coder. IEEE Trans Commun. 1984;32(3):225–32.

65. Aubry N. On the hidden beauty of the proper orthogonal decomposition. Theor Comput Fluid Dyn. 1991;2(5–6):339–52.

66. Siegel SG, Seidel J, Fagley C, Luchtenburg DM, Cohen K, Mclaughlin T. Low-dimensional modelling of a transient cylinder wake using double proper orthogonal decomposition. Vol. 610, Journal of Fluid Mechanics. 2008. 1–42 p.

67. Hama FR. Streaklines in a Perturbed Shear Flow. Phys Fluids. 1962;5(6):644.

68.   Graham J, Lee M, Malaya N, Moser RD, Eyink G, Meneveau C, et al. Turbulent channel flow data set. 2013;1–8.

69.   Perlman E, Burns R, Li Y, Meneveau C. Data exploration of turbulence simulations using a database cluster. Proc 2007 ACM/IEEE Conf Supercomput (SC '07). 2007;

70.   Li Y, Perlman E, Wan M, Yang Y, Meneveau C, Burns R, et al. A public turbulence database cluster and applications to study Lagrangian evolution of velocity increments in turbulence. J Turbul. 2008;9(December 2016):N31.

71.   Yu H, Kanov K, Perlman E, Graham J, Frederix E, Burns R, et al. Studying Lagrangian dynamics of turbulence using on-demand fluid particle tracking in a public turbulence database. J Turbul. 2012;13(August 2015):N12.

72.   Scarano F. Iterative image deformation methods in PIV. Meas Sci Technol. 2002;13(1):R1–19.

73.   Eckstein AC, Charonko J, Vlachos P. Phase correlation processing for DPIV measurements. Exp Fluids. 2008;45(3):485–500.

74.   Eckstein A, Vlachos PP. Digital particle image velocimetry (DPIV) robust phase correlation. Meas Sci Technol. 2009;20(5):055401.

75.   Eckstein A, Vlachos PP. Assessment of advanced windowing techniques for digital particle image velocimetry (DPIV). Meas Sci Technol. 2009;20(7):075402.

76.   Westerweel J, Scarano F. Universal outlier detection for PIV data. Exp Fluids. 2005;39(6):1096–100.

77.   Xue Z, Charonko JJ, Vlachos PP. Particle image velocimetry correlation signal-to-noise ratio metrics and measurement uncertainty quantification. Meas Sci Technol. 2014;25(11):115301.

78.   Charonko JJ, Vlachos PP. Estimation of uncertainty bounds for individual particle image velocimetry measurements from cross-correlation peak ratio. Meas Sci Technol. 2013;24(6):065301.

79.   Zhou J, Adrian RJ, Balachandal S, Kendall TM. Mechanisms for generating coherent packets of hairpin vortices in channel flow. J Fluid Mech. 1999;387:353–96.

80.   Etebari A, Vlachos PP. Improvements on the accuracy of derivative estimation from DPIV velocity measurements. Exp Fluids. 2005;39(6):1040–50.

81.   Shariff K, Leonard A. Vortex Rings. Annu Rev Fluid Mech. 1992;24:235–79.

82.   Gharib M, Rambod E, Shariff K. A universal time scale for vortex ring formation. J Fluid Mech. 1998;360:121–40.

83. Savitzky A, Golay MJE. Smoothing and Differentiation of Data by Simplified Least Squares Procedures. Anal Chem. 1964;36(8):1627–39.

84. Krumm J. Savitzky-Golay filters for 2D images. 2001;98052.

85. Walpot RJE, van der Geld CWM, Kuerten JGM. Determination of the coefficients of Langevin models for inhomogeneous turbulent flows by three-dimensional particle tracking velocimetry and direct numerical simulation. Phys Fluids. 2007;19(4).

86. Oxlade AR, Valente PC, Ganapathisubramani B, Morrison JF. Denoising of time-resolved PIV for accurate measurement of turbulence spectra and reduced error in derivatives. Exp Fluids. 2012;53(5):1561–75.

87. Schanz D, Gesemann S, Schröder A. Shake-The-Box: Lagrangian particle tracking at high particle image densities. Exp Fluids. 2016;57(5):1–27.

88. Didden N. On the formation of vortex rings: rolling up and production of circulation. J Appl Math Phys. 1979;30:101–16.

89. Wright SF, Zadrazil I, Markides CN. A review of solid–fluid selection options for optical-based measurements in single-phase liquid, two-phase liquid–liquid and multiphase solid–liquid flows. Vol. 58, Experiments in Fluids. Springer Berlin Heidelberg; 2017. 1–39 p.

90. Yazdi SG, Geoghegan PH, Docherty PD, Jermy M, Khanafer A. A Review of Arterial Phantom Fabrication Methods for Flow Measurement Using PIV Techniques. Ann Biomed Eng. 2018;

91. Mayer GA. Blood Viscosity in Healthy Subjects and Patients With Coronary Heart Disease. Can Med Assoc J. 1964;91:951–4.

92. Yousif MY, Holdsworth DW, Poepping TL. A blood-mimicking fluid for particle image velocimetry with silicone vascular models. Exp Fluids. 2011;50:769–74.

93. Long JA, Ündar A, Manning KB, Deutsch S. Viscoelasticity of pediatric blood and its implications for the testing of a pulsatile pediatric blood pump. ASAIO J. 2005;51(5):563–6.

94. Najjari MR, Hinke JA, Bulusu K V., Plesniak MW. On the rheology of refractive-index-matched, non-Newtonian blood-analog fluids for PIV experiments. Exp Fluids. 2016;57(6):1–6.

95. Bai K, Katz J. On the refractive index of sodium iodide solutions for index matching in PIV. Exp Fluids. 2014;55(4).

96. Shuib AS, Hoskins PR, Easson WJ, Model ASA. Flow Regime Characterization in a Diseased Artery Model. 2010;4(2):87–91.

97. Nguyen TT. A Method for Matching the Refractive Index and Kinematic Viscosity of a

Blood Analog for Flow Visualization in Hydraulic Cardiovascular Models. J Biomech Eng. 2004;126(4):529.

98. Bale-Glickman J, Selby K, Saloner D, Savaş O. Experimental Flow Studies in Exact-Replica Phantoms of Atherosclerotic Carotid Bifurcations Under Steady Input Conditions. J Biomech Eng. 2003;125(1):38.

99. Deplano V, Knapp Y, Bailly L, Bertrand E. Flow of a blood analogue fluid in a compliant abdominal aortic aneurysm model: Experimental modelling. J Biomech. 2014;47(6):1262–9.

100. Warren JR, Gordon JA. On the refractive indices of aqueous solutions of urea. J Phys Chem. 1966;70(1):297–300.

101. Ramnarine K V., Nassiri DK, Hoskins PR, Lubbers J. Validation of a new blood-mimicking fluid for use in Doppler flow test objects. Ultrasound Med Biol. 1998;24(3):451–9.

102. Thurston GB. Rheological parameters for the viscosity viscoelasticity and thixotropy of blood. Biorheology. 1979;16(3):149–62.

103. Varghese SS, Frankel SH, Fischer PF. Direct numerical simulation of stenotic flows, Part 2: Pulsatile flow. J Fluid Mech. 2007;582:281.

104. He S, Jackson JD. An experimental study of pulsating turbulent flow in a pipe. Eur J Mech B/Fluids. 2009;28(2):309–20.

105. Scotti A, Piomelli U. Numerical simulation of pulsating turbulent channel flow. Phys Fluids. 2001;13(5):1367–84.

106. Iguchi M, Park G moon, Koh Y ha. The structure of turbulence in pulsatile pipe flows. KSME J. 1993;7(3):185–93.

107. Eckmann DM, Grotberg JB. Experiments on transition to turbulence in oscillatory pipe flow. J Fluid Mech. 1991;222:329–50.

108. Yellin EL. Laminar-Turbulent Transition Process in Pulsatile Flow. Circ Res. 1966;19(4):791–804.

109. Stettler JC, Hussain AKMF. On transition of the pulsatile pipe flow. J Fluid Mech. 1986;170:169–97.

110. Peacock J, Jones T, Tock C, Lutz R. The onset of turbulence in physiological pulsatile flow in a straight tube. Exp Fluids. 1998;24(1):1–9.

111. Falsetti HL, Carroll RJ, Swope RD, Chen CJ. Turbulent blood flow in the ascending aorta of dogs. Cardiovasc Res. 1983;17(7):427–36.

112. Brindise MC, Vlachos PP. Proper orthogonal decomposition truncation method for data denoising and order reduction. Exp Fluids. 2017;58(4):28.

113. Daubechies I. Ten lectures on wavelets. SIAM; 1992.

114. Vetterli M, Herley C. Wavelets and filter banks: Theory and design. IEEE Trans Signal Process. 1992;40(9):2207–32.

115. Mallat SG. A Theory for Multiresolution Signal Decomposition: The Wavelet Representation. IEEE Trans Pattern Anal Mach Intell. 1989;11(7):674–93.

116. Xu D, Chen J. Accurate estimate of turbulent dissipation rate using PIV data. Exp Therm Fluid Sci. 2013;44:662–72.

117. Stanislas M, Okamoto K, Kähler CJ, Westerweel J, Scarano F. Main results of the third international PIV Challenge. Exp Fluids. 2008;45(1):27–71.

118. Lassen JF, Holm NR, Stankovic G, Lefevre T, Chieffo A, Hildick-Smith D, et al. Percutaneous coronary intervention for coronary bifurcation disease: Consensus from the first 10 years of the European Bifurcation Club meetings. EuroIntervention. 2014;10(5):545–60.

119. Van Der Heiden K, Gijsen FJH, Narracott A, Hsiao S, Halliday I, Gunn J, et al. The effects of stenting on shear stress: Relevance to endothelial injury and repair. Cardiovasc Res. 2013;99(2):269–75.

120. Antoniadis AP, Giannopoulos AA, Wentzel JJ, Joner M, Giannoglou GD, Virmani R, et al. Impact of local flow haemodynamics on atherosclerosis in coronary artery bifurcations. EuroIntervention. 2015 May 19;11(V):V18–22.

121. LaDisa JF, Olson LE, Molthen RC, Hettrick D a, Pratt PF, Hardel MD, et al. Alterations in wall shear stress predict sites of neointimal hyperplasia after stent implantation in rabbit iliac arteries. Am J Physiol Heart Circ Physiol. 2005;288(5):H2465–75.

122. Hoi Y, Zhou YQ, Zhang X, Henkelman RM, Steinman DA. Correlation between local hemodynamics and lesion distribution in a novel aortic regurgitation murine model of atherosclerosis. Ann Biomed Eng. 2011;39(5):1414–22.

123. Yazdani SK, Moore JE, Berry JL, Vlachos PP. DPIV measurements of flow disturbances in stented artery models: adverse affects of compliance mismatch. J Biomech Eng. 2004;126(5):559–66.

124. Darremont O, Leymarie JL, Lefevre T, Albiero R, Mortier P, Louvard Y. Technical aspects of the provisional side branch stenting strategy. EuroIntervention. 2015;11:V86–90.

125. Hildick-Smith D, de Belder AJ, Cooter N, Curzen NP, Clayton TC, Oldroyd KG, et al. Randomized trial of simple versus complex drug-eluting stenting for bifurcation lesions:

the British Bifurcation Coronary Study: old, new, and evolving strategies. Circulation. 2010;121(10):1235–43.

126. Yamashita T, Nishida T, Adamian MG, Briguori C, Vaghetti M, Corvaja N, et al. Bifurcation Lesions : Two Stents Versus One Stent — Immediate and Follow-up Results. 2000;35(5):1145–51.

127. Kervinen K, Niemelä M, Romppanen H, Erglis A, Kumsars I, Maeng M, et al. Clinical outcome after crush versus culotte stenting of coronary artery bifurcation lesions: The nordic stent technique study 36-month follow-up results. JACC Cardiovasc Interv. 2013;6(11):1160–5.

128. Raben JS, Morlacchi S, Burzotta F, Migliavacca F, Vlachos PP. Local blood flow patterns in stented coronary bifurcations: an experimental and numerical study. J Appl Biomater Funct Mater. 2014 Dec 19;13(2):116–26.

129. Charonko J, Karri S, Schmieg J, Prabhu S, Vlachos P. In vitro, Time-resolved PIV comparison of the effect of stent design on wall shear stress. Ann Biomed Eng. 2009;37(7):1310–21.

130. Dzavik V, Kharbanda R, Ivanov J, Ing DJ, Bui S, Mackie K, et al. Predictors of long-term outcome after crush stenting of coronary bifurcation lesions: Importance of the bifurcation angle. Am Heart J. 2006;152(4):762–9.

131. Ozolanta I, Tetere G, Purinya B, Kasyanov V. Changes in the mechanical properties, biochemical contents and wall structure of the human coronary arteries with age and sex. Med Eng Phys. 1998;20(7):523–33.

132. Hain R, Kähler CJ. Fundamentals of multiframe particle image velocimetry (PIV). Exp Fluids. 2007;42(4):575–87.

133. Raben JS, Hariharan P, Robinson R, Malinauskas R, Vlachos PP. Time-Resolved Particle Image Velocimetry Measurements with Wall Shear Stress and Uncertainty Quantification for the FDA Nozzle Model. Cardiovasc Eng Technol. 2015;7(1):7–22.

134. Sklansky J. Image Segmentation and Feature Extraction. IEEE Trans Syst Man Cybern. 1978;8(4):237–47.

135. Davies JE, Whinnett ZI, Francis DP, Willson K, Foale R a, Malik IS, et al. Use of simultaneous pressure and velocity measurements to estimate arterial wave speed at a single site in humans. Am J Physiol Heart Circ Physiol. 2006;290(2):H878–85.

136. Segers P, Swillens A, Taelman L, Vierendeels J. Wave reflection leads to over- and underestimation of local wave speed by the PU- and QA-loop methods: theoretical basis and solution to the problem. Physiol Meas. 2014;35(5):847–61.

137. Charonko JJ, Ragab S a., Vlachos PP. A Scaling Parameter for Predicting Pressure Wave Reflection in Stented Arteries. J Med Device. 2009;3(1):011006.

138. Morlacchi S, Chiastra C, Gastaldi D, Pennati G, Dubini G, Migliavacca F. Sequential Structural and Fluid Dynamic Numerical Simulations of a Stented Bifurcated Coronary Artery. J Biomech Eng. 2011;133(12):121010.

139. Chiastra C, Morlacchi S, Pereira S, Dubini G, Migliavacca F. Computational fluid dynamics of stented coronary bifurcations studied with a hybrid discretization method. Eur J Mech - B/Fluids. 2012 Sep;35:76–84.

140. Morlacchi S, Colleoni SG, Cárdenes R, Chiastra C, Diez JL, Larrabide I, et al. Patient-specific simulations of stenting procedures in coronary bifurcations: Two clinical cases. Med Eng Phys. 2013;35(9):1272–81.

141. Vlak MHM, Algra A, Brandenburg R, Rinkel GJE. Prevalence of unruptured intracranial aneurysms, with emphasis on sex, age, comorbidity, country, and time period: A systematic review and meta-analysis. Lancet Neurol. 2011;10(7):626–36.

142. Ford MD, Nikolov HN, Milner JS, Lownie SP, Demont EM, Kalata W, et al. PIV-measured versus CFD-predicted flow dynamics in anatomically realistic cerebral aneurysm models. J Biomech Eng. 2008 Apr;130(2):021015.

143. Cebral JR, Raschi M. Suggested connections between risk factors of intracranial aneurysms: A review. Ann Biomed Eng. 2013;41(7):1366–83.

144. Xu J, Yu Y, Wu X, Wu Y, Jiang C, Wang S, et al. Morphological and Hemodynamic Analysis of Mirror Posterior Communicating Artery Aneurysms. PLoS One. 2013;8(1):1–7.

145. Cibis M, Potters W V., Gijsen FJ, Marquering H, Van Ooij P, Van Bavel E, et al. The effect of spatial and temporal resolution of cine phase contrast MRI on wall shear stress and oscillatory shear index assessment. PLoS One. 2016;11(9):1–15.

146. Roloff C, Bordás R, Nickl R, Mátrai Z, Szaszák N, Szilárd S, et al. Investigation of the velocity field in a full-scale model of a cerebral aneurysm. Int J Heat Fluid Flow. 2013;43:212–9.

147. Raschi M, Mut F, Byrne G, Putman CM, Tateshima S, Vinuela F, et al. CFD and PIV analysis of hemodynamics in a growing intracranial aneurysm. Int j numer method biomed eng. 2012;28(1):72–86.

148. Brindise MC, Busse MM, Vlachos PP. Density- and Viscosity-matched Newtonian and non-Newtonian Solutions with PDMS Refractive Index. Exp Fluids. 2018;59:173.

149. Wieneke B. Volume self-calibration for 3D particle image velocimetry. Exp Fluids. 2008;45(4):549–56.

150. Bhattacharya S, Charonko JJ, Vlachos PP. Stereo-particle image velocimetry uncertainty quantification. Meas Sci Technol. 2017;28:015301.

151. Herman GT, Lent A. Iterative reconstruction algorithms. Comput Biol Med. 1976;6(4):273–94.

152. Elsinga GE, Westerweel J, Scarano F, Novara M. On the velocity of ghost particles and the bias errors in Tomographic-PIV. Exp Fluids. 2011;50(4):825–38.

153. Stalder AF, Russe MF, Frydrychowicz A, Bock J, Hennig J, Markl M. Quantitative 2D and 3D phase contrast MRI: Optimized analysis of blood flow and vessel wall parameters. Magn Reson Med. 2008;60(5):1218–31.

154. Xu L, Liang F, Gu L, Liu H. Flow instability detected in ruptured versus unruptured cerebral aneurysms at the internal carotid artery. J Biomech. 2018;72:187–99.

155. Rayz VL, Boussel L, Ge L, Leach JR, Martin AJ, Lawton MT, et al. Flow residence time and regions of intraluminal thrombus deposition in intracranial aneurysms. Ann Biomed Eng. 2010;38(10):3058–69.

RESEARCH INTERESTS

Cerebral aneurysm and cardiovascular hemodynamics, transition to turbulence in pulsatile pipe flows, experimental and signal processing methods development for flow and biomedical applications, and automated left ventricle segmentation.

EDUCATION

- *Doctor of Philosophy in Mechanical Engineering,* Purdue University, West Lafayette, IN, USA, December 2019.
- *Bachelor of Science in Aeronautical Engineering*, Purdue University, West Lafayette, IN, USA, December 2013.

PUBLICATIONS

- **Brindise, M.C.**, Rothenberger, S., Dickerhoff, B., Schnell, S., Markl, M., Saloner, D., Rayz, V.L., Vlachos, P.P. (2019). Multi-modality cerebral aneurysm haemodynamic analysis: *in vivo* 4D Flow MRI, *in vitro* particle velocimetry, and *in silico* computational fluid dynamics. *Journal of the Royal Society Interface.* 16(158), 20190465.
- **Brindise, M.C.**, Busse, M.M., Vlachos, P.P. (2018). Density- and viscosity-matched Newtonian and non-Newtonian blood-analog solutions with PDMS refractive index. *Experiments in Fluids*, 59(11), 173.
- **Brindise, M.C.**, Vlachos, P.P. (2018). Pulsatile pipe flow transition: Flow waveform effects. *Physics in Fluids.* 30(1), 015111.
- **Brindise, M.C.**, Chiastra, C., Burzotta, F., Migliavacca, F., Vlachos, P.P. (2017). Hemodynamics of Stent Implantation Procedures in Coronary Bifurcations: An In Vitro Study. *Ann. Biomed. Eng.* 45(3), 542-553.
- **Brindise, M.C.**, Vlachos, P.P. (2017). Proper Orthogonal Decomposition Truncation Method for Data Denoising and Order Reduction. *Exp. in Fluids.*
- Acuna A., Berman A.G., Damen F.W., Meyers B.A., Adelsperger A.R., Bayer K.C., **Brindise M.C.**, Bungart B., Kiel A.M., Morrison R.A., Muskat J.C., Wasilczuk, K.M., Wen, Y., Zhang, J., Zito, P., Goergen, C.J. (2018). Computational Fluid Dynamics of

Vascular Disease in Animal Models. *Journal of Biomechanical Engineering*. 140(8):080801.

CONFERENCE PROCEEDINGS

Podium Presentations

- **Brindise, M.C.**, Rothenberger, S., Schnell, S., Markl, M., Saloner, D., Rayz, V.L., Vlachos, P.P. (2019, June 25). Effect of gravity on hemodynamics in cerebral aneurysms – an *in vitro* study. Summer Biomechanics, Bioengineering, and Biotransport Conference. Seven Springs, PA, USA.

- **Brindise, M.C.**, Rothenberger, Dickerhoff, B., S., Schnell, S., Markl, M., Saloner, D., Rayz V.L., Vlachos, P.P. (2018, Nov 20). Comprehensive flow structures and hemodynamic analysis of patient-specific cerebral aneurysms using volumetric PIV. American Physical Society – Division of Fluid Dynamics. Atlanta, GA, USA.

- Zhang, J., **Brindise, M.C.**, Scalo, C., Vlachos, P. (2018, Nov 20). Pressure reconstruction using velocity measurement-error based generalized least-squares. American Physical Society – Division of Fluid Dynamics. Atlanta, GA, USA.

- Rothenberger, S., **Brindise, M.C.**, Muskat, J., Dickerhoff, B., S., Schnell, S., Markl, M., Saloner, D., Vlachos, P.P., Rayz V.L. (2018, Nov 20). Patient-specific modeling of cerebral aneurysms hemodynamics: Comparisons of CFD, *in vitro*, and *in vivo* 4D Flow MRI. American Physical Society – Division of Fluid Dynamics. Atlanta, GA, USA.

- **Brindise, M.C.**, Rothenberger, Dickerhoff, B., S., Schnell, S., Markl, M., Saloner, D., Rayz V.L., Vlachos, P.P. (2018, July 12). Comparing volumetric PIV, CFD, *in vitro* and *in vivo* PC-MRI results in cerebral aneurysms. World Congress of Biomechanics. Dublin, Ireland.

- **Brindise, M.C.**, Dickerhoff, B., Saloner, D., Rayz, V.L., Vlachos, P.P. (2017, Nov 20). Investigation of patient-specific cerebral aneurysm using volumetric PIV, CFD and *in vitro* PC-MRI. American Physical Society – Division of Fluid Dynamics. Denver, CO, USA.

- **Brindise, M.C**., Vlachos, P.P. (2016, Nov 22). Transition to Turbulence in Pulsatile Pipe Flow. American Physical Society – Division of Fluid Dynamics. Portland, OR, USA.

- **Brindise, M.C**., Dickerhoff, B., Saloner, D., Rayz, V.L.,Vlachos, P.P. (2016, Nov 20). Volumetric PIV in Patient-Specific Cerebral Aneurysm. American Physical Society – Division of Fluid Dynamics. Portland, OR, USA.
- **Brindise, M.C**., Vlachos, P.P. (2015, Nov 24). Experimental Comparison of Bifurcating Coronary Stent Techniques. American Physical Society – Division of Fluid Dynamics. Boston, MA, USA.

Poster Presentations
- **Brindise, M.C.**, Zhang, J., Dickerhoff, B., Scalo, C., Schnell, S., Markl, M., Saloner, D., Rayz, V.L., Vlachos, P.P. (2016, Oct 22). 4D Flow-MRI, PIV, and CFD Integrated Framework for Investigating Velocity and Pressure Fields in Patient Specific Cerebral Aneurysm. International Society for Magnetic Resonance in Medicine Workshop on Quantitaive MR: Innovation & Implementation for Clinical & Physiological Insights. San Francisco, CA.

AWARDS AND HONORS
- American Heart Association Pre-Doctoral Fellowship (July 2017)
- Lambert Teaching Fellowship (Fall 2017)
- Perry Fellowship (Spring 2014)
- Gerald I Gilbert Memorial Scholarship (Fall 2014)
- Pratt & Whitney Scholarship (Fall 2013)
- Purdue Presidential Scholarship (Fall 2010-Fall 2013)

TEACHING EXPERIENCES
- Lambert Teaching Fellow, *Lecturer*, ME 309 – Fluid Mechanics, August 2017 – May 2019
- Lead Teaching Assistant, *Lab Manager*, ME 309 – Fluid Mechanics, August 2015 – May 2017
- Teaching Assistant, *Lecturer and Lab Assistant*, ME 309 – Fluid Mechanics, August 2014 – May 2015